‘Astrocytic cradle’ controls extracellular potassium and glutamate during synaptic transmission

Olga Tiurikova

Dissertation submitted for the
Degree of Doctor of Philosophy

University College London

Department of Clinical & Experimental Epilepsy
Queen Square Institute of Neurology

Declaration

I, Olga Tiurikova, confirm that the work presented in this thesis is my own. Where information has been derived from other sources, I confirm that this has been indicated in the thesis.

September 2019

Abstract

It is widely recognised that astrocytes are able to shape synaptic transmission by restricting glutamate transients to the synaptic cleft. In this thesis, I demonstrate that during synaptic transmission K^+ efflux through postsynaptic NMDA receptors depolarises the astrocytic membrane and thus slows down glial glutamate uptake. This effect involves the rectifying K^+ channels (Kir4.1), predominantly located at perisynaptic astrocytic processes (PAPs). Genetic upregulation of this channel subtype in astrocytes does not affect glutamate transporters efficiency but curtails increase in presynaptic glutamate release probability during extracellular K^+ rises. Thus, activity-dependent accumulation of extracellular K^+ can boost glutamate release from the presynaptic site while decreasing astroglial glutamate uptake. Both factors occasion increased extrasynaptic glutamate escape and therefore inter-synaptic crosstalk in the hippocampus.

Impact Statement

Through the thesis, I used advanced, up-to-date imaging methodology to investigate one of the principal mechanisms underlying neuron-glial interaction in the tripartite synapse, and how electrogenic regulation of astrocytic glutamate transporters affects synaptic transmission.

From the methodology perspective, accurate evaluation of [Ca^{2+}] signalling in the brain tissue is severely restricted by light scattering and a low signal-to-noise ratio. To overcome these limitations I applied a time-resolved imaging approach combined with a newly developed spiral line scanning regime. Fluorescence lifetime imaging (FLIM) of the Ca^{2+}-sensitive dye Oregon Green BAPTA-1 provides necessary sensitivity for measuring low basal [Ca^{2+}] fluctuation (below 100 nM). Furthermore, FLIM readout does not depend on indicator concentration, light scattering or absorption. Spiral scanning mode allowed me to follow fluorescence signal dynamics in small structures (such as presynaptic boutons) at an unprecedented speed. Combining these approaches has provided a cutting-edge technique for rapid multiphoton imaging in organised brain tissue.

From the scientific standpoint, I obtained novel insights into the mechanisms underpinning astroglial regulation of excitatory synaptic transmission. I showed that intense synaptic activity, within the physiological range, can induce significant depolarisation of local astrocytic membranes due to local accumulation of extracellular K^+. The shift of astrocyte resting potential causes a slowdown of glutamate uptake by astroglial transporters. This mechanism boosts glutamate spillover and inter-synaptic crosstalk, suggesting a possible effect on computational properties of hippocampal neuronal networks. The depolarisation of astrocytic membrane involves functioning of inward rectifying K^+ channels (Kir4.1). Genetic upregulation of which curtails increased extracellular [K^+] rises that are often associated with pathophysiological synaptic transmission. Perturbed function or downregulation of astrocytic Kir4.1 channels has been demonstrated in various neurodegenerative disorders, including hippocampal sclerosis,

Huntington’s disease, and epilepsy. Given the slow progress of pharmacological treatment of these diseases, rescuing expression of functional Kir4.1 channels by gene therapy might open new directions for potential therapeutic strategies.

I believe therefore that, from both methodological and scientific perspectives, my work could have a significant value for a better understanding of regulatory mechanisms underpinning synaptic function and plasticity in the hippocampus, in health and disease.

Acknowledgements

I am grateful to everyone with whom I have had the pleasure to work during my studies. Firstly, I would like to thank my primary supervisor Professor Dmitri Rusakov for supporting me through my studies; without his constant trust, it would not be possible to conduct this research.

Many thanks to my supervisor Professor Alexey Semyanov for introducing me to neuroscience in the first place, always challenging me further to master new skills, and for his continued support.

Thank you, Annika, Alistair, Rob, Pey-Yu, Tom and Yulia! I appreciate our collaborative work; I learn so many things while working with you.

I am very thankful to all DCEE members that make me feel so welcome, for lots of troubleshooting advice, stimulating discussions and all the fun we have had in the last four years.

Special thanks to members of Synaptic Imaging laboratory: Kayu for helping with data analysis and equipment alinement; Tom and Sylvain for their patience in guiding me through all stages of research. Thank you, Lesha and Olga, for fascinating conversations, and both scientific and emotional support.

My research would have been less pleasant without the support of my friends and family. Thank you, Yulia, Katia, Seryozha and Masha for cheering me up, as usual; Doran for your generous help with English during my thesis journey; my long-time friends Yulia and Ilusha for their support and advice.

Finally, I would like to thank my family for their love and endless encouragement, especially throughout my PhD study.

Publication contributions during PhD

Tyurikova O., Zheng K., Rings A., Drews A., Klenerman D.,Rusakov D.,
Monitoring Ca^{2+} elevations in individual astrocytes upon local release of amyloid beta in acute brain slices,
Brain Res Bull. 2018 Jan; 136:85-90

Lebedeva A., Plata A., Nosova O., Tyurikova O., Semyanov A.,
Activity-dependent changes in transporter and potassium currents in hippocampal astrocytes,
Brain Res Bull. 2018 Jan; 136:37-43

Jensen T., Zheng K., Tyurikova O., Reynolds J., Rusakov D.,
Monitoring single-synapse glutamate release and presynaptic calcium concentration in organised brain tissue,
Cell Calcium. 2017 Jun; 64:102-108

Jennings A., Tyurikova O., Bard L., Zheng K., Semyanov A., Henneberger C., Rusakov D.,
Dopamine elevates and lowers astroglial Ca^{2+} through distinct pathways depending on local synaptic circuitry,
Glia. 2017 Mar; 65(3):447-459

Manuscripts in preparation:

Tyurikova O., Nicholson E., Zheng K., Timofeeva Y., Semyanov A., Volynski K., Rusakov D.,
FLIM reveals regulation of presynaptic Ca^{2+} by glutamate uptake, mGluRs, but not somatic voltage in cortical neurons,
(submitted to Journal of Neurochemistry)

Tyurikova O., Shih P-Y., Dembitskaya Y., McHugh T., Rusakov D., Semyanov A.,

K^+ efflux through postsynaptic NMDA receptors suppresses astrocytic glutamate uptake

Tyurikova O., Nicholson E., Kullmann D., Rusakov D., Volynski KE.

Tornado-FLIM acquisition for monitoring single-synapse presynaptic calcium dynamics in a mouse model of a migraine

Contents

List of figures

Abbreviations

AAV	adeno associated virus
AC	adenylyl cyclase
ACSF	artificial cerebrospinal fluid
AD	Alzheimer's disease
AM	acetoxymethyl
AMPA	α-amino-3-hydroxy-5-methyl-4-isoxazolepropionicn acid
AP	action potential
ATP	adenosine triphosphate
Aβ	beta amyloid
Best-1	bestrophin-1 channel
$[Ca^{2+}]$	calcium concentration
cAMP	cyclic adenosine monophosphate
CA	Cornu Ammonis
CSF	cerebrospinal fluid
CNS	central nervous system
DA	dopamine
DAG	diacylglycerol
DARPP-32	dopamine- and cyclic-AMP-regulated phosphoprotein, Mr32 kDa
EAAT	excitatory amino acid transporter
EGFP	enhanced green fluorescent protein
EPSP	excitatory postsynaptic potential
FIMAS	fluorescent imaging analysis software
fEPSP	field excitatory postsynaptic potential
EK	equilibrium potential
ER	endoplasmic reticulum
FLIM	fluorescence lifetime imaging microscopy
$GABA_A$	γ-aminobutyric acid type A (receptor)
$GABA_B$	γ-aminobutyric acid type B (receptor)
GDNF	glial cell line-derived neurotrophic factor

GECIs	genetically encoded calcium indicators
GFAP	glial fibrillary acidic protein
GJC	gap-junction connection
GLAST-1	L-glutamate/L-aspartate transporter
GLT-1	L-glutamate transporter
GltPh	homologue of the glutamate transporter from Pyrococcus horikoshi
GPCR	G-protein-coupled receptor
GS	glutamine synthetase
HFS	high-frequency stimulation
IP3	inositol 1,4,5-trisphosphate
IP3R2	inositol triphosphate receptor type 2
$[K^+]$	potassium concentration
Kd	dissociation constant
Kir	inward rectifying potassium channels
Kir4.1	inward rectifying potassium channels subtype 4.1
KMS	potassium methanesulfonate
KO	knockout mouse
LTD	long-term depression
LTP	long-term potentiation
mEPSC	miniature excitatory postsynaptic current
mGluR	metabotropic glutamate receptor
mIPSC	miniature inhibitory postsynaptic current
$[Na^+]$	sodium concentration
NADH	nicotinamide adenine dinucleotide
NGF	nerve growth factor
NMDA	N-methyl-D-aspartate
NMDG	N-methyl-D-glucamin
NKA	Na/K-ATPase
OGB-1	Oregon Green BAPTA-1, hexapotassium salt, cell impermeant
OGB-2	Oregon Green BAPTA-2, octapotassium salt, cell impermeant
OGB-AM	Oregon Green BAPTA, cell permeant version

PAPs	perisynaptic astrocyte processes
PBS	phosphate-buffered saline
PKA	protein kinase A
PKC	protein kinase C
PCR	polymerase chain reaction
Pr	release probability
PrPc	prion protein
RL	re-entrant loop
SC	Schaffer collaterals
SNARE	soluble N-ethylmaleimide sensitive factor attachment protein receptor
SR-101	sulforhodamine 101
TCSPC	time correlated single photon counting
TRP	transient receptor potential channel
VGCC	voltage-gated calcium channel
VGLUT1	vesicular glutamate transporter type 1
VRACs	volume-regulated anion channels
WT	wild type

Chapter 1: Introduction

Synopsis

For decades, synaptic circuits have been associated solely with neuronal cell-to-cell connections represented by the presynaptic terminal, which releases a neurotransmitter, and the postsynaptic neuronal specialisation, a site where the neurotransmitter can activate synaptic receptors. Accumulated evidence has revealed another active contributor to synaptic signalling - astroglial cells (Araque et al., 1999; Perea et al., 2009; Santello et al., 2012). Historically, Rudolf Virchow (1858) proposed the neuroglia concept. At the time, common electrophysiological techniques have been used to understand the functions of electrically-passive astrocytes. Half a century later, and only with the advance in electrophysiology and live cell imaging techniques, it became possible to detect internal Ca^{2+} signalling in astrocytes. This novel insight to astrocytic signalling prompted a re-think of their contribution to synaptic transmission. Nowadays, astrocytes are known to modulate neuronal synapse formation during development (Reichenbach et al., 2010), to provide energy substrates (MacVicar and Choi, 2017), and to control cerebral blood flow (Takano et al., 2006). Also, as an active component of the synapse, astrocytes shape signal transduction implementing rapid glutamate uptake (Bergles and Jahr, 1998; Diamond, 2001), buffering K^+ (Ransom and Sontheimer, 1992; Amédée et al., 1997), releasing signalling molecules (Bezzi et al., 1998; Coco et al., 2003) and possibly altering the architecture of synaptic environment (Henneberger et al., 2018).

In this thesis, I am asking how the cooperation of astrocytic K^+ buffering and glutamate uptake through glutamate transporters modulates the dynamics of extracellular glutamate, inside and outside the synaptic cleft, during physiological activity.

1.1. Morphological properties of protoplasmic astrocytes

Glial cells possess extremely diverse morphological characters, which might be explained by fine-tuning to the architecture of the particular brain region. The dramatic increase in processes elaboration, as well as glial density and parallels, increases brain complexity during evolution. The ratio of glia to neurons in cortex developed from 0.3 in rodents to 1.65 in humans (Figure 1.1a–b; Hof et al., 2006). Further comparison of rodent and human astrocytes revealed that the latter is not only larger and more complex but also contacting more than a million synapses, compared to thousands in rodents (Oberheim et al., 2009). Despite the vast morphological and territorial diversity across the brain region and species, astrocytes common features include smaller soma size compared to neurons (~10-12 μM), and a system of numerous fine protrusions, with one or more contacting blood vessel forming the endfoot (Figure 1.1b).

Additionally, having close contact with the site of synaptic transmission allow astrocytes to interact with, and reportedly modulate the neuronal activity. Fine astrocytic processes either approach or enwrap a large proportion of synapses (Figure 1.1d–e). For instance, in the rodent hippocampus, intracellular fluorescent dyes reveal that individual astrocytes can 'cover' up to 140,000 synapses (Bushong et al., 2002; Ogata and Kosaka, 2002), and ~57% of all hippocampal synapses are approached by nanoscopic perisynaptic astrocyte processes (PAPs). Non-overlapping territories of individual astroglia were identified by viral injections combined with 3D reconstruction in cortex *in vivo*, demonstrating that a single astrocyte enwraps on average of four neuronal somas with an upper limit of eight neuronal somas (Halassa et al. 2007). In the mouse hippocampus, intracellular injection of two different fluorescent dyes into neighbouring astrocytes revealed that they occupied spatially separate areas, with limited overlap (Figure 1.1c). Most peripheral processes interdigitate with one another, with the overlap representing only

<5% of the astrocytic tissue domain (Figure 1.1c; Bushong et al., 2002; Ogata and Kosaka, 2002).

Freeze-fracture electron microscopy revealed that astrocytes are connected through gap-junctions, which is constituted by the facing of two hemichannels (Massa and Mugnaini, 1985). Combination of electrophysiological recordings and immunoblotting disclosed that gap-junctions formed primarily from connexin 43 (Giaume et al., 1991), although connexin 30 is also present (Nagy et al., 1999). The diameter of such pores typically reaches 1.0 – 1.5 nm, allowing conducting ions and molecules up to several kDa. Introduction of the Lucifer Yellow dye or other low molecular weight dye to an individual astrocyte reveal dye-coupled cells (Fischer and Kettenmann, 1985; Konietzko and Müller, 1994) and allow the identification of coherent glial syncytium (Nagy and Rash, 2000). This dye coupling of astrocytes is significantly upregulated by membrane depolarisation and by an increase in the extracellular K^+ concentration in a dose-dependent manner (Kristian Enkvist and McCarthy, 1994; De Pina-Benabou et al., 2018). Such glial syncytium offers substrates for neurons including modulating speed and direction of Ca^{2+} waves (Dani et al., 1992) and dissipating local peaks of Na^+ and K^+ (Kofuji and Newman, 2004; Steinhäuser et al., 2012).

Astrocytes are split into distinct subtypes, according to their morphological features, localization in a particular CNS region or species-specificity (e.g. interlaminar astrocytes of cerebral cortex of higher primates) (Colombo and Reisin, 2004; Tabata, 2015). The largest group of astrocytes possessing stellate-like morphology include protoplasmic and fibrous astrocytes. The latter are mostly present in the white matter: they have long processes, with a lesser degree of branching (Miller and Raff, 1984). The protoplasmic astrocytes are located in the grey matter and represent complex cells with numerous elaborate processes. This thesis focuses on hippocampal protoplasmic astrocytes, throughout the chapters.

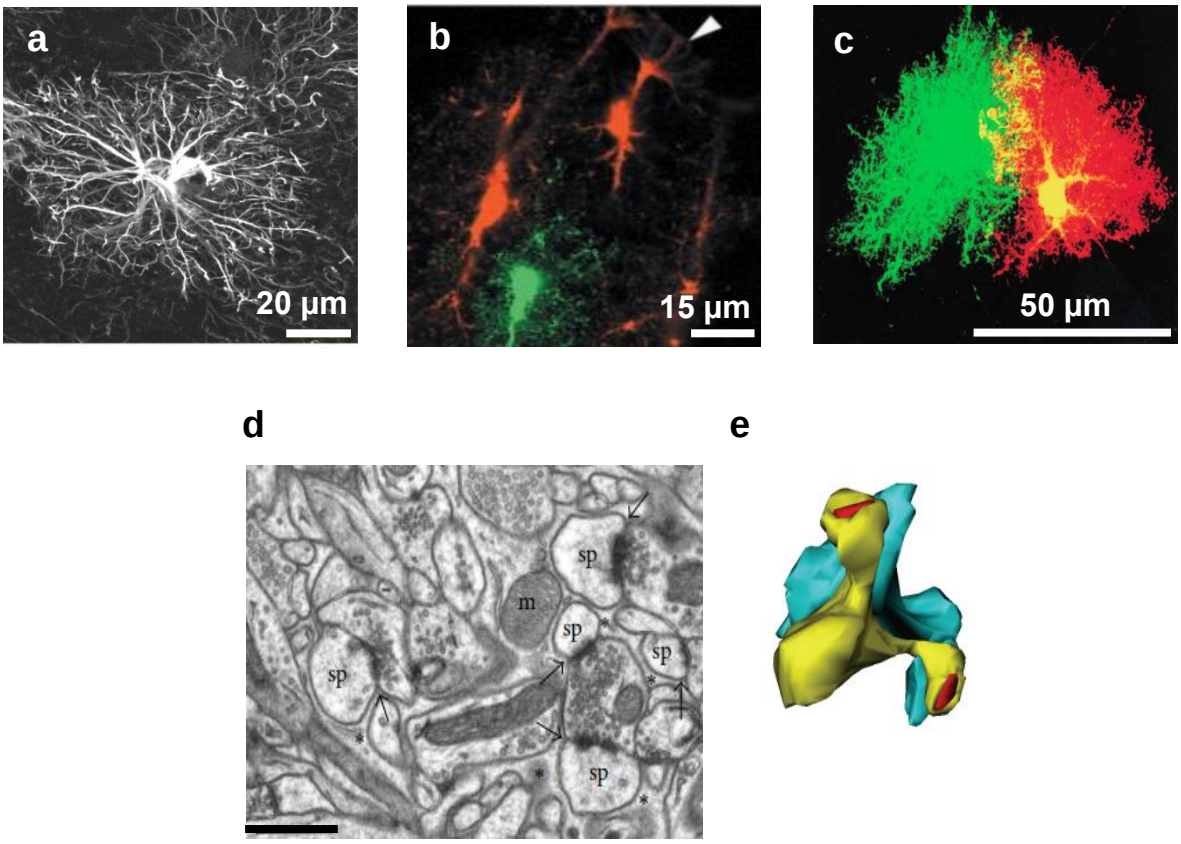

Figure 1.1 Morphological features of protoplasmic astrocytes

a- Human astrocyte from cortical layers 2-6 labelled with GFAP
b- Rat astrocyte from s*tratum radiatum* region filled with distinct fluorescent dyes Lucifer yellow (green) and Alexa-568 (red). Astrocytic endfeet enwraps blood vessel (arrow)
c- Confocal image of two mouse astrocytes in the *stratum radiatum* region, labelled with Lucifer yellow (green) and biocytin-conjugated Cascade blue (red). Protrusions of labelled astrocytes overlap in the border between them
d- Electron microscopy image of mouse cortex depicting dendritic spines (sp) enwrapped by astrocytic protrusions (*); scale bar: 1 µm
e- 3D reconstruction of the dendritic spine (yellow) and astrocytic processes (blue) shown in d. Postsynaptic density represented with red colour

a - adapted from Oberheim et al., 2009; b - adapted from Bushong et al., 2002 c - adapted from Ogata and Kosaka, 2002; d and e - adapted from Bernardinelli et al., 2014

1.2. Electrophysiological properties of the astrocytic membrane

Astrocytes from different brain regions express a multitude of ion channels and receptors (Bordey and Sontheimer, 2000; Verkhratsky and Steinhäuser, 2000). Expression of astroglial receptors, transporters and channels undergo substantial and multi-directional developmental changes. For instance, in the hippocampus, the expression level of metabotropic glutamate receptors mGluR 5 decreases with age (Cai et al., 2000), while that of mGluR 3 increases (Devaraju et al., 2013). Despite the difference in ion/receptors machinery of hippocampal astrocytes, they have generally considered a relatively homogenous electrophysiological group with respect to their resting membrane potential, which is around -85 mV. A hyperpolarising shift of resting membrane potential is explained predominantly by the K^+ conductance, which is enriched in the astrocytic plasma membrane (Walz et al., 1984). According to the initial Kuffler's finding on K^+ channels, it is the main inward rectifying (Kir) channels that are responsible for a larger portion of K^+-mediated conductance at rest membrane potential in glial cells (Kuffler and Nicholls, 1966; Newman, 1987, 1993).

Molecular cloning identified 16 Kir channel subunits, which are grouped into 7 Kir subfamilies (Kir1.x – Kir7.x). All the subtypes consist of two transmembrane domains and share common functional features, such as sensitivity to micromolar concentration of Ba^{2+} (Coetzee et al., 1999) and a preferentially inward current direction (Hagiwara and Takahashi, 1974; Alagem et al., 2001). Furthermore, channel current rectification is determined by a voltage-dependent block of the channel pore by intracellular Mg^{2+} or polyamines, such as spermine (Fakler et al., 1995; Oliver et al., 2000). Olsen et al. (2006) demonstrated in their two studies that among Kir channels subfamilies, Kir1.x, Kir4.x, Kir5.x and Kir7.x show weak rectification properties, allowing outward K^+ currents. However, Kir2.x and Kir3.x subfamilies are strongly rectifying channels, barely conducting ions in the outward direction

(Olsen and Sontheimer, 2004). Although these studies were performed in two different groups of glial cells (spinal cord astrocytes and malignant glia), more recent studies confirm that the majority of rectifying currents in rodent astrocytes represent weak rectification properties (underling their ability to conduct ions in the outward direction under certain circumstances) (Casper et al., 2007; Tong et al., 2014; Dvorzhak et al., 2016). Takumi et al. and Pessia et al. have shown that astrocytes predominantly express the inward rectifying channel Kir4.1 and Kir5.1 (Takumi et al., 1995; Pessia et al., 1996). Further studies employing single-cell PCR analysis have revealed that astrocytes in *stratum radiatum* region of the hippocampus also expresses Kir2.1, Kir2.2 and Kir3.3 channel subtypes, but at a lower level (Schröder et al., 2002). In addition, studies conducted in knockout animals revealed the critical importance of Kir4.1 channels for brain function. Mice lacking Kir4.1 channels died prematurely and showed the most substantial pathology in the white matter, spinal cord and the hippocampus (Neusch et al., 2005). Nevertheless, even a partial Kir4.1 deletion restricted to only GFAP-positive cells produced a severe phenotype with ataxia, paralysis and stress-induced seizures and caused profound astrocytic depolarisation (Casper et al., 2007). These and other related findings indicate that the Kir4.1 channel subfamily underlines the bulk of K^+ conductance in hippocampal astrocytes. Ultrastructural studies show that Kir4.1 channels are generally localised in fine astrocytic protrusions such as PAPs with the close proximity to neuronal synaptic terminals (Higashi et al., 2001; Ulbricht et al., 2008). The high-density Kir4.1 channels (which are leaky at resting membrane potential), together with a high surface-to-volume ratio, set the astrocytic input resistance at around 10 MOh. The domination of K^+ over Na^+ conductance underlines electrically passive properties of astrocytes, especially the inability to generate and conduct self-sustained electrical signals such as action potentials (APs).

1.3. An overview of astrocytic functions

Astrocytes maintain ion homeostasis of the extracellular space by engaging a range of cellular mechanisms. The extracellular space of the brain is enriched with Na^+ ions and low with K^+, which is roughly reversed inside the brain cells. This counter-balance is critical for maintaining neuronal excitability in a continued and reproducible fashion, including generation and propagation of action potentials. Even a slight alteration in the concentration of extracellular ions could produce significant changes in the cell resting membrane potential, with a consequent change in the activation of voltage-gated channels (Armstrong and Hille, 1998), neuronal firing (McBain, 1994) and neurotransmitter release (Meeks and Mennerick, 2004). Under physiological conditions astrocytes are capable of clearing the excess of extracellular K^+ by ensuring 'K^+ shuttle': K^+ after rapid uptake and accumulation in astrocytic cytoplasm released back to extracellular space (Figure 1.2; Verkhratsky et al., 2019). Also at resting condition, astrocytes maintain intracellular Na^+ concentration around 15-20 mM. This range is ensured by balanced Na^+ extrusion, almost exclusively implemented through Na^+/K^+-ATPase, and Na^+ influx through multitude of Na^+ channels, Na^+-dependent solute carrier (SLC) transporters and Na^+-dependent neurotransmitter transporters. The latter include excitatory amino acid glutamate transporters (EAATs) providing efficient glutamate uptake, empowered by the inward directing Na^+ transmembrane gradient (Unichenko et al., 2012). Inside astrocytes, glutamate is converted to glutamine and extracted back to the extracellular space in a non-toxic form so it could be taken up by the presynaptic terminal and converted back to glutamate (Bak et al., 2006). Function of EAATs allow astrocytes to rapidly take up glutamate against its steep concentration gradient, thus limiting the escape of extrasynaptic glutamate and preventing neurotoxicity (described in section 1.7; Bergles and Jahr, 1997; Diamond and Jahr, 1997).

Another key astrocytic property is ability of supplying neurons with required metabolic substrates through the astrocyte-neuronal lactate shuttle

(Pellerin and Magistretti, 1994). Neurons demand large amounts of energy to maintain and restore ion gradients disrupted during AP propagation, postsynaptic current, and uptake and recycling of neurotransmitters (Attwell and Laughlin, 2001). Astrocytic endfeet enriched with glucose transporter 1 allowing to take up glucose from blood vessels and use it as a substrate for the synthesis of lactate. The contiguous astrocytic syncytium (equipped with functional gap-junction channels) allows trafficking of lactate through syncytium and it futher shuttle from astrocytes to neurons via monocarboxylic acid transporters (Figure 1.2).

Apart from releasing lactate (Pellerin and Magistretti, 2012), astrocytes are able to release a range of signalling molecules including classical neurotransmitters (so-called gliotransmitters when released from glia cells; Araque et al.,1999; Bezzi and Volterra, 2001), their precursors (Hertz, 2013), neuromodulators (Henneberger et al., 2010b; Martineau et al., 2014), hormones (Morte and Bernal, 2014), peptides (Krzan et al., 2003), ROS scavengers (Minich et al., 2006), growth factors (Toyomoto et al., 2004). It is also shown that astrocytes undergoing mechanical or metabolic injury are capable of releasing inflammatory cytokines (Lau and Yu, 2001). In the next chapter, I describe ability of astrocytes to release classical neurotransmitters, as the objectives of this thesis include evaluation of astrocytic impact on efficient glutamatergic synaptic transmission.

1.4. Release of gliotransmitters from astrocytes

Early studies in mixed cultures reported that elevated Ca^{2+} level in astrocytes could lead to Ca^{2+} elevations in nearby neurons (Parpura et al., 1994; Araque et al., 1998). It was found that the neuro-ligand bradykinin applied exogenously triggered Ca^{2+} elevation and glutamate exocytosis from astrocytes. Further studies in cultured cells showed that pharmacological activation of purinergic receptors promotes ATP release (Abdipranoto et al.,

2003). These findings have been subsequently confirmed in acute hippocampal slices. In particular glutamate released from astrocytes is prompted to synchronised neuronal activity (Porter and McCarthy, 1996; Angulo et al., 2004; Fellin et al., 2004; Liu et al., 2004), while astrocytic ATP release appeared to increase postsynaptic efficacy (Gordon et al., 2005). It has long been established that excitatory transmitters were not the only signalling molecules to be released from astrocytes. Experiments in astroglial cultures and acute brain slices (taken from various brain regions) have demonstrated robust release of GABA from glial cells (Liu et al., 2000), activating neuronal high-affinity GABA receptors that leads to tonic inhibition (Lee et al., 2010; Héja et al., 2012; Wójtowicz et al., 2013).

Presently, release of afformed signalling molecules is identified as a mechanism involving Ca^{2+}-mediated exocytosis and non-vesicular release. Non-vesicular release from astroglia appears as Ca^{2+} independent; it involves transporters such as glutamate-cysteine exchanger (Warr et al., 1999), the reverse mode of glutamate transporters (Nicholls and Attwell, 1990; Longuemare and Swanson, 1995; Marcaggi et al., 2005), ionotropic purinergic receptors (Duan et al., 2003), and volume-regulated anion channels (VRACs) (Kimelberg et al., 1990). However, described non-vesicular signalling occurs solely under pathological conditions (high intracellular $[Na^+]$/glutamate in combination with depolarisation caused by elevated extracellular $[K^+]$) such as ischemic or osmotic stress (Liu et al., 2006). In near-physiological conditions, the two mechanisms of non-vesicular glutamate release were suggested: Ca^{2+}-independent, via the opening of the two-pore domain potassium channel TREK-1 and the Ca^{2+}-dependent, via the opening of the glutamate-permeable anion channel Best-1 (Woo et al., 2012).

For vesicular release, astrocytes possess the required secretory machinery employing proteins of the core SNARE complex, and H^+-ATPase, which mediates loading of glutamate into vesicles (Montana et al., 2006; Bohmbach et al., 2018). It was established that the application of the H^+-ATPase inhibitor bafilomycin to astrocytic cultures significantly reduced the amount of Ca^{2+}-mediated glutamate secretion (Araque et al., 2000). In many

cases, the transmitter release is triggered by the activation of G protein-coupled receptors (GPCRs), with subsequent IP3-mediated Ca^{2+} release from internal stores. However, unlike in neurons, fusion of vesicles in astrocytes after intracellular Ca^{2+} elevation occur on a much slower scale (hundreds of milliseconds; Bezzi et al., 2004; Kreft et al., 2004). This difference leaves fact of the fast gliotransmission during physiological conditions under debate and endorses a principal specialisation of astrocytes as a major homeostatic component of the network.

1.5. Potassium signalling ensured by astrocytes

The focus of the present work is interplay between astrocytic potassium signalling and efficient operation of glutamate transporters. In this section, I describe in more details astrocytic potassium signalling. During the intense neuronal activity, the local concertation of K^+ ions might rise significantly to 4 – 5 mM (Adelman and Fitzhugh, 1975). It is reasonable to think that at the hotspots of K^+ effluxes, such as activated NMDA receptors (which could stay open for 100 – 300 milliseconds, Lester et al., 1990), this concentration could be much higher. Astrocytes provide the critical system that helps to maintain the physiological level of extracellular K^+, mainly by engaging the Na^+/K^+-ATPase, the inwardly rectifying potassium channel (predominantly Kir4.1 subtype; Ransom et al., 2000; D'Ambrosio et al., 2002) and operation of Na^+/K^+ /Cl^- co-transporters (Macvicar et al., 2002). The latter show ability to operate under condition when extracellular K^+ concentration ($[K^+]$) exceeding physiological range (Larsen et al., 2014), leaving the leading role for extracellular K^+ clearance during physiological synaptic transmission to Na^+/K^+-ATPase and inward rectifying channels. Taking advantage of K^+-selective microelectrodes and pharmacological tools D'Ambrosio et al. demonstrated a distinct impact of Na^+/K^+-ATPase and Kir channels to maintain extracellular K^+ homeostasis during high frequency simulation. Hence,

pharmacological block of Na^+/K^+-ATPase with ouabain lead to elevation of extracellular [K^+] baseline and abolish recovery after stimulus-evoked K^+ elevation (D'Ambrosio et al., 2002; Meeks and Mennerick, 2007). Meanwhile, block of Kir channels with Ba^{2+} does not affect the rate of post-stimulus recovery, but lead to an increase of extracellular K^+ baseline (D'Ambrosio et al., 2002). Stimuli-induced extracellular [K^+] accumulation would shift K^+ equilibrium potential to more positive that their membrane potential and allow for transiently negative electrochemical gradient for K^+, triggering outward K^+ current. Thus, Kir channels are capable of replenishing extracellular [K^+] during Na^+/K^+-ATPase-mediated undershoot. Genetic approach associated with conditional deletion of Kir4.1 channel subtype from astrocytes demonstrated that these channel subtype is important for setting rest membrane potential and astrocytic ability respond to the stimulus (Chever et al., 2010, Haj-Yasein et al., 2011). Together these studies implicate synergetic operation of Na^+/K^+-ATPase and inward rectifying channels to maintain K^+ homeostasis, although the relative contribution of each might vary according to the regime of activity.

After K^+ uptake into astrocyte it can be subsequently released back to extracellular space through Kir channels or to the blood flow through the astrocytic endfeet, also enriched with K^+ channels (Paulson and Newman, 1987; Chever et al., 2010). Recent computer simulation study employing astroglial model with realistic morphology also suggest that significant extracellular K^+ buffering could be achieved by ion redistribution within individual astroglia (Savtchenko et al., 2018). This process prevents excessive local astrocytic depolarisation and leads to a minimal elevation of K^+ concentration across the intracellular lumen of astroglia. Active control of extracellular [K^+] provides astrocytes with a powerful mechanism to rapidly modulate network activity (Bellot-Saez et al., 2017).

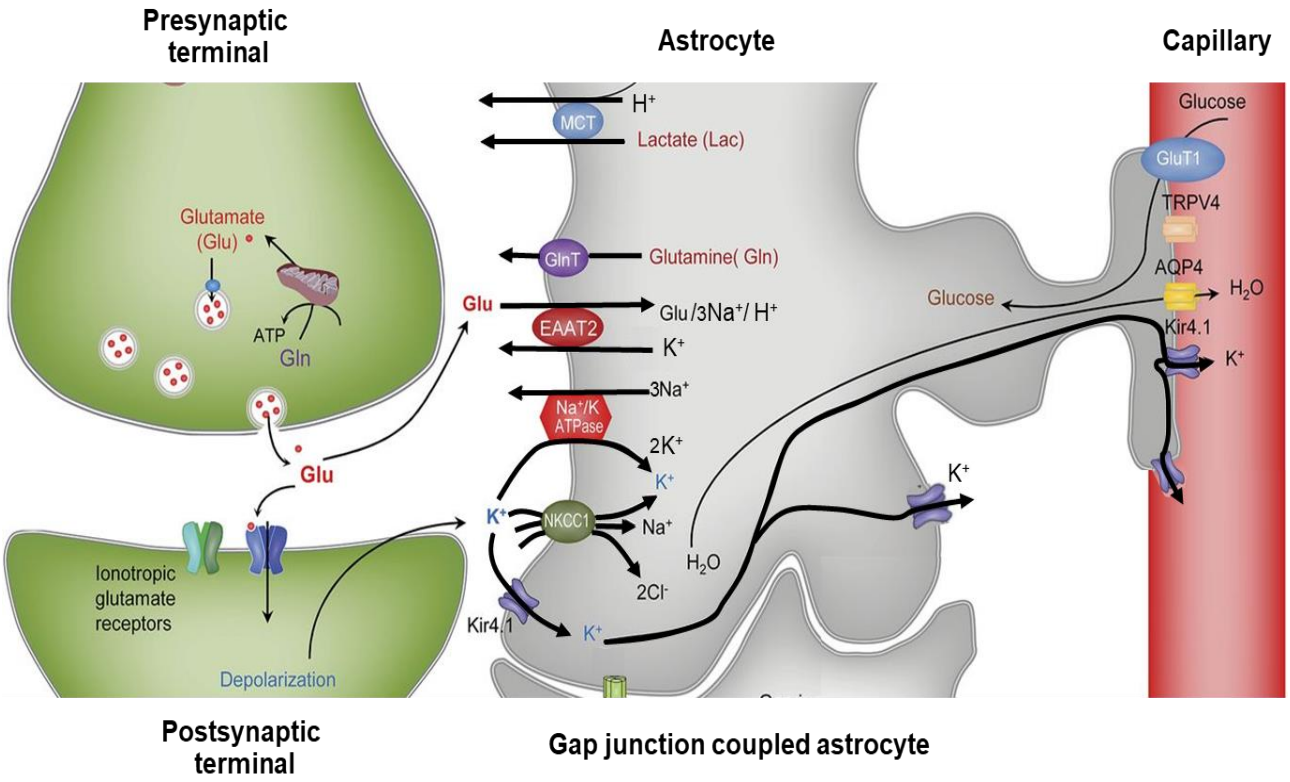

Figure 1.2 Potassium signalling ensured by 'astrocytic cradle'

Schematic representation of neuron-glial interactions: neurons represented by presynaptic and postsynaptic terminals, 'astrocyte cradle' represented by perisynaptic astrocytic process (PAPs) depicted in the middle. Astrocyte operates as 'K^+ shuttle' by ensuring rapid K^+ uptake from extracellular space through K^+ channels (mainly Kir4.1 subtype), operation of Na^+/K^+ ATPase, and $Na^+/K^+/Cl^-$ co-transporters 1 (NKCC1, which predominantly operate when extracellular [K^+] overload) and releasing K^+ back to either extracellular space or capillary through Kir4.1 channels. Astrocyte also contributes to glutamate uptake through operation of high-affinity excitatory amino acid transporters 2 (EAAT2) - secondary-active transport powered by the membrane electrical gradient where one molecule of glutamate, three Na^+ ions and one H^+ exchange for one K^+ ion. After translocation, glutamate converted to glutamine via the glutamine synthase pathway and then extruded to the extracellular space via glutamine transporter (GlnT). Astrocytic endfeet enriched with glucose transporter 1 (GluT1) allow to take up glucose and use it as a substrate for the synthesis of lactate. Lactate then shuttled from astrocytes to neurons via monocarboxylic acid transporters (MCTs).

Modified from Benarroch, 2016

1.6. Ca^{2+} signalling in astrocytes

Unlike neurons that engage regenerative membrane currents to propagate electrical signals, non-excitable astrocytes are believed to use intracellular Ca^{2+} waves for physiological communication. The field of astrocytic Ca^{2+} signalling has rapidly advanced with the development of ion-sensitive fluorescent indicators and methodological advances in fluorescent cellular imaging including two-photon excitation microscopy (Charles et al., 1991; Cornell-Bell and Finkbeiner, 1991). Historically, cellular imaging with organic fluorescent dyes led to the discovery of Ca^{2+} waves in cultured glial cells, which is generated in response to glutamate application (Cornell-Bell et al., 1990). Further studies employing ratiometric dyes found that glutamate-induced Ca^{2+} elevation is directly associated with synaptic transmission in mixed cultures (Dani et al., 1992), acute slices (Porter and McCarthy, 1996) and *in vivo* (Hirase et al., 2004; Wang et al., 2006). It has been well established that intense physiological release of neurotransmitters such as glutamate and GABA can evoke Ca^{2+} signals in astrocytes through the activation of ionotropic (Palygin et al., 2010), metabotropic (Pasti et al., 1997; Kirischuk et al., 1999; Wang et al., 2006; Biesecker and Srienc, 2015), transient receptor potential channels (TRP)(Verkhratsky et al., 2014) or GABA transporters (Boddum et al., 2016). Restricting neuronal activity (for instance, by blocking AP generation with TTX) reveal that astrocytes have a spontaneous Ca^{2+} oscillations, even in the absence of evoked synaptic transmission (Nett et al., 2002; Jiang et al., 2014). This observation prompts a straightforward suggestion that astrocytes not only passively respond to neuronal firing but could also generate their own pattern of activity, which could potentially influence synaptic transmission.

1.6.2. Basal Ca^{2+} and spontaneous Ca^{2+} events in astrocytes

Maintaining of basal Ca^{2+} level in brain cells in a diapason of 70 – 140 nM ensures a wide dynamic range required for Ca^{2+}-dependent molecular cascades. Throughout this research, basal cytosolic Ca^{2+} represents Ca^{2+} level prior to any endogenous or exogenous stimulation. Basal Ca^{2+} level represents a dynamic equilibrium between Ca^{2+} sources (such as ion channels, stores, or transporters), sinks (pumps and ion exchangers) and buffers i.e., Ca^{2+} binding proteins, active sequestration by mitochondria (Shigetomi, Patel and Khakh, 2016). Over a period of observation, basal Ca^{2+} also incorporate equilibrated spontaneous Ca^{2+} transients that occurs without stimulation. In hippocampal astrocytes, activation of transient receptor potential A1 channels (TRPA-1) underlines localised 'spotty' Ca^{2+} events that are significantly contributing to [Ca^{2+}] basal level (Shigetomi et al., 2012; Shigetomi and Jackson-Weaver, et al., 2013). Such events occur randomly, without any external stimulation (Tong et al., 2012). Ca^{2+} concentration measurements performed with the ratiometric dye Fura-2 estimating basal [Ca^{2+}] in cultured hippocampal astrocytes (i.e. during conditions of negligible light scattering) around 100 – 120 nM (Tong et al., 2012). The advance of time-resolved fluorescence microscopy (fluorescence lifetime imaging, FLIM) has enabled a similar type of measurement in organised brain tissue, with a high degree of light scattering and absorption (Zheng et al., 2015). This finding demonstrated a decrease of [Ca^{2+}] during development as well as an increase of [Ca^{2+}] levels from cell somata towards peripheral astrocytic branches. The latter difference of 20 – 30 nM was proposed to be associated with more significant Ca^{2+} influx in the peripheral part of the cell (Shigetomi et al., 2013; Otsu et al., 2015). High sensitivity to small changes in [Ca^{2+}] revealed two populations of astrocytes with different basal Ca^{2+} concentration: 70 – 75 nM and 120 – 130 nM (Zheng et al., 2015).

The basal [Ca^{2+}] level in astrocytes appears to underlie some distinct physiological properties of the cell. Its relatively small changes, from 80 to 140 mM, have been shown to trigger glutamate-induced currents in neighbouring

neurons (Parpura and Haydon, 2000). Dialysing astrocytes with high-affinity Ca^{2+} buffer - BAPTA reduces the release of purines while decreasing excitatory synaptic transmission in the hippocampus (Panatier et al., 2011). Another study of hippocampal astrocytes has demonstrated that clamping internal Ca^{2+} concentration at a low level restricts long-term potentiation (LTP) induction by limiting the occupancy NMDA receptors co-agonist sites with D-serine (Henneberger et al., 2010). This effect was reversed by applying a saturating concentration of D-serine. Continued maintenance of adequate extracellular D-serine levels is also crucial for developing full cell arborisation and a high spine density of pyramidal neurons in the cortex (Balu et al., 2012). Astrocytic [Ca^{2+}] levels also affect local blood flow. Again, BAPTA introduction to astrocytes limits the available Ca^{2+} ions and reduces the size of neighbouring arterioles (Rosenegger et al., 2015).

1.6.3. Astroglial Ca^{2+} signalling evoked by common neurotransmitters

Several in-depth physiological studies have shed light on the primary mechanisms pertinent to induced Ca^{2+} elevation in astrocytes. Astrocytes possess receptors machinery required for Ca^{2+} signalling. Mobilisation of internal Ca^{2+} was shown to depend on Ca^{2+}-permeable ionotropic receptors such as α-amino-3-hydroxy-5-methyl-4-isoxazolepropionicn acid (AMPA), N-Methyl-D-glucamin (NMDA) (Lalo et al., 2006), glutamate and purine receptors (Lalo et al., 2011; Palygin et al., 2010), and a reverse mode of the Na^{+}/Ca^{2+} exchanger (Yang et al., 2015). The majority of studies performed in near-physiological conditions report mGluRs – mediated Ca^{2+} elevation in astrocytes. Activation of metabotropic receptors leads to the production of inositol triphosphate (IP3), which in turn triggers Ca^{2+} release from the endoplasmic reticulum (ER) (Finch et al., 1991; Berridge, 2009). Among the

three IP3Rs isoforms, hippocampal astrocytes express primary subtype 2 (IP3R2) (Holtzclaw et al., 2002), suggesting that the IP3R2-mediated pathway for intracellular Ca^{2+} elevation might be predominant for astrocytes. The diffusion of IP3 cause the propagation of Ca^{2+} signals, which can be long-lasting in certain conditions (Koizumi, 2010; Kuga et al., 2011). Ca^{2+} waves have an essential role in the synaptic functioning such as triggering of the release of neurotransmitters (Henneberger et al., 2010; Koizumi, 2010) and synchronisation of neuron firing (Fellin et al., 2004).

Over the last 10 years, more detailed monitoring of Ca^{2+} activity was performed in fine astrocytic protrusions (Di Castro et al., 2011; Henneberger and Rusakov, 2012). This was mainly achieved by the introduction of genetically encoded Ca^{2+} sensors as well as improvement of imaging methods. Studies using genetically encoded Ca^{2+}-sensitive sensor (yellow Cameleon-nano 50) *in vivo* report the occurrence of spontaneous activity, predominantly in astrocytic fine protrusions rather than cell bodies, with an occasional wave-like pattern of propagation across glial syncytium (Kanemaru et al., 2014). This mechanism also was known to be IP3R2-mediated.

1.6.4. Astroglial Ca^{2+} signalling that does not involve common neurotransmitters

Several studies in cultured astroglia have shown that Ca^{2+} elevations in astrocytes are triggered not only by neurotransmitter release. It was shown that mechanical interruptions of astrocyte may induce Ca^{2+} waves followed by the concentric wave propagation to the neighbouring astrocytes via gap-junctions (Venance et al., 1997; Charles, 1998). A brief and strong acidic stimulation also increases the Ca^{2+} level in astrocytes (Nagaoka et al., 2011). Another factor that could trigger astroglial Ca^{2+} responses is a change of extracellular osmolality. Exposure to the hypo-osmotic environment was

shown to trigger cell swelling followed by a Ca^{2+} elevation (Fischer et al., 1997; Morales-Mulia et al., 1998). Listed stimuli could evoke Ca^{2+} signalling by activating transient receptor potential channels (reviewed in Verkhratsky and Burnstock, 2014). TRP channels expressed in astrocytes (TRPA-1, TRPV-4, TRPC-1, 4, 5) (Pizzo et al., 2001; Golovina, 2005; Song et al., 2005) regulate the Ca^{2+} basal level and contribute to spontaneous Ca^{2+} transients (Shigetomi et al., 2012; Shigetomi and Jackson-Weaver, et al., 2013), thus affecting the store-operated Ca^{2+} entry (Golovina, 2005).

1.7. Astrocytic glutamate transporters: structure, kinetic model and physiological impact

Astrocytes can take up to 80% per cent of released glutamate via their excitatory amino acid transporters (EAATs) (Kim et al., 2011). Glutamate uptake by astroglial transporters represents a secondary-active transport and is powered by the membrane electrical gradient where one molecule of glutamate, one H^+ and three Na^+ ions exchange for one K^+ ion (Figure 1.3a; Owe et al., 2006; Zerangue and Kavanaugh, 1996). Five subtypes of EAATs have been identified in the central nervous system (CNS) (EAAT 1-5) (Lehre et al., 1995). Glutamate transporters type 3 and 4 are expressed in neuronal cell bodies and postsynaptic terminals (Lehre et al., 1995). However, expression of EAATs type 5 is thought to be restricted to the retina (Pow and Barnett, 2000). Glial cells predominantly express two transporters subtypes, EAAT-1 and EAAT-2, also called L-glutamate/L-aspartate transporter (GLAST-1) and L-glutamate transporter (GLT-1), respectively (Chaudhry et al., 1995; Gadea and López-Colomé, 2001). The glutamate transporters type 1 is expressed mainly in Bergmann glial cells while EAAT-2 is found in PAPs (Lehre et al., 1995; Danbolt, 2001; Minelli et al., 2001). It is thus considered the critical glial glutamate transporter subtype in the context of excitatory circuit function. EAAT-2 has also been found, in low quantities, in the neuronal

terminals of excitatory synapses of hippocampal CA3 pyramidal cells (Furness et al., 2008).

1.7.1. Structural properties of excitatory amino acid transporters

The aforementioned EAATs subtypes share around 60% homology amino acid sequence identity and 30 – 40% with the bacterial glutamate transporter homologue (Tolner et al., 1992). Despite the difference in transporter structure between eukaryotic and prokaryotic cells, they do possess common features including co-transport of protons along with Na^+ ions. Therefore, the glutamate transporter homologue GltPh from *Pyrococcus horikoshii* has generally been accepted to represent a legitimate model for studying the structure of Na^+-dependent glutamate transporters. Cloning of bacterial glutamate transporter analogue GltPh allows to identifying main structural features of glutamate transporters (Yernool et al., 2004). Crystallisation experiments have revealed that the N-terminal peptide (as shown in grey in Figure 1.3b) of glutamate transporters consists of 1 – 6 transmembrane domains, while C-terminal consists of two transmembrane domains (7 and 8, as depicted with red in Figure 1.3b) and two re-entrant loops — RL1 and RL2 (Yernool et al., 2004). Being submerged into the membrane, these re-entrance loops are essential for glutamate (as shown in green in Figure 1.3b) and Na^+ (as depicted with blue in Figure 1.3b) binding sites, and also sheltering these sites from the extracellular space exposure (Bendahan et al., 2000). Studies using crystal structure of GltPh supplemented with thallium (Tl^+) ions have revealed two binding sites for Na^+: site 1 – TI2, located 'underneath' the aspartate complex; site 2 – TI1, is buried under RL2 (Boudker et al., 2007). Moreover, the crystal structure obtained from GltPh incubated with the non-transportable blocker TBOA, showed TBOA blocks RL2 in an open conformation, and thus restricting Na^+ from binding to site 2 and

preventing all further conformations. Proposed stoichiometry of the GltPh coupling ratio 1:2 (rather than the 1:3 established for mammalian glutamate transporters) explains the existence of two, rather than three, cation binding sites.

1.7.2. Glutamate transporter kinetics

Operation of glutamate transporters consists of two distinct half-cycles (Figure 1.3d; Bergles, Tzingounis and Jahr, 2002; Akyuz et al., 2013). The first half-cycle includes binding and translocation of Na^+, glutamate, and a proton inside astrocytes, with subsequent unbinding. The second half-cycle includes reorientation of the binding sites upon counter transport of K^+. Glutamate transport is also associated with an uncoupled Cl^- flux (Fairman et al., 1995); however, the physiological relevance of such transport remains under debate. One possible explanation is that the two positive charges that move into the cell with each cycle would depolarise the membrane and reduce the driving force for glutamate. The uncoupled Cl^- influx might provide an offset for depolarisation and support efficient glutamate uptake from the extracellular space. Reverse operation of astrocytic glutamate transporters, when glutamate is released to the extracellular space, is highly unlikely to occur under physiological conditions. However, it has been proposed to take place during pathological circumstances such as ischemia (Camacho and Massieu, 2006) or spinal cord injury (Li et al., 2018). Estimation of theoretical transporter kinetics in the reverse mode was performed by several computational studies (Watzke and Grewer, 2001; Zhang et al., 2007). Reverse transport was shown to be faster (around 55 s^{-1} compared to forward 24 s^{-1}) but less voltage-dependent than the forwarding one (Zhang et al., 2007).

1.7.3. Regulation of glutamate transporter operation

During synaptic transmission astrocytic glutamate transporters are activated by increased extracellular glutamate concentration (Mennerick and Zorumski, 1994). The activity of glutamate transporters can be affected by thermodynamic factors (such as Na^+/K^+ gradients or membrane potential), kinetic factors, impacting on transporter affinity, lateral diffusion or expression level. Glutamate transporters ensure Na^+-dependent glutamate uptake and thus an altered Na^+ balance, for instance, resulting from increased intracellular Na^+, will suppressed the efficacy of glutamate removal (Unichenko et al., 2012; Rimmele et al., 2017). Also absence of extracellular Na^+ has been shown to abolish glutamate transporter current, and decrease the decay time (Ƭ decay) (Grewer et al., 2000). Likewise, altered K^+ gradient has been shown to affect operation of glutamate transporters. Studies using a variety of *in vitro* preparations have shown that either a direct elevation of extracellular K^+ itself (Ransom and Goldring, 1973), or intense synaptic activity associated with K^+ accumulation in the synaptic cleft, produce depolarisation of glial cells (Orkand et al., 1966; Karwoski et al., 1989). This was confirmed *in situ* (Meeks and Mennerick, 2007) and further addressed *in vivo* (Amzica, 2002; Amzica et al., 2002; Chever et al., 2010) experiments.

Several stages of glutamate uptake by glial transporters were shown to be strongly voltage-dependent, including the binding of first and third Na^+ ion, the step re-orientating transporter's residuals inside the cell, the unbinding step for the first Na^+ and the K^+-dependent translocation (Figure 1.3d; Wadiche et al., 1995). Among the key kinetic factors, affecting transport is the phosphorylation of amino acid residues. Both EAAT-1 and EAAT-2 possess protein kinase C (PKC) phosphorylation consensus sites. However, its phosphorylation in EAAT-1 produces an inconsistent effect, while the functional effect of PKC on EAAT-2 decreases glutamate uptake (González and Ortega, 1997). Another factor affecting the efficiency of glutamate transport is an interaction either with Zn^{2+} (Vandenberg et al., 1998) or with

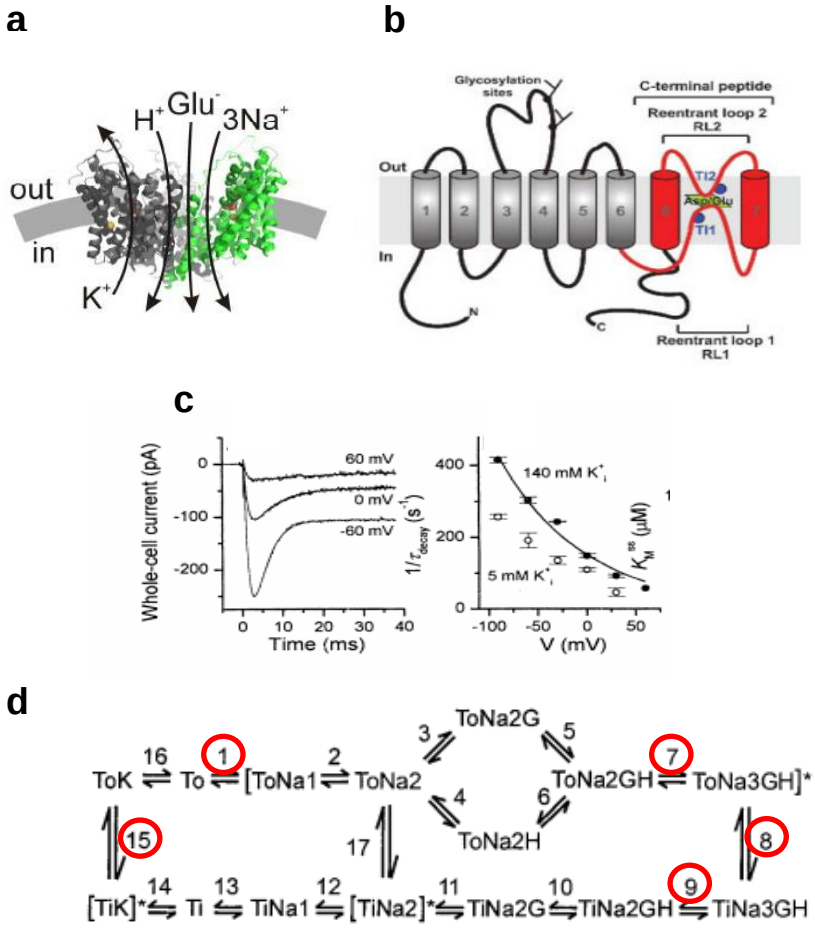

Figure 1.3 Properties of glutamate transporters

a- Stoichiometry of coupling of substrates to the co-transport of three Na^+ ions, one proton, and the counter-transport of one K^+

b- GltPh membrane topology, experiments performed with two Tl^+ ions revealed two binding sites TI1 and TI2 (blue)

c- Whole-cell recording of glutamate transporters current from HEK-293 cells at the room temperature. Glutamate currents were isolated with the application of TBOA to the perfusion. *Left*: laser-photolysis experiments at membrane potential -60, 0, 60 mV, glutamate concentration 60 µM. Voltage-dependence decay time (Ƭ decay) increase from 3,4 ms to 6,4 ms and 19 ms. *Right*: voltage-dependence of 1/Ƭ decay in presence of 140 mM extracellular K^+ and 60 µM glutamate concentration (painted circles) or 5mM K^+ and 50 µM glutamate concentration (open circles)

d- Kinetic model of the GLT-1 transporter, voltage-dependent stages marked with red circles.

a - adopted from Rauen et al., 2014, b - adopted from Grewer et al., 2008, c - from Grewer et al., 2000, d - modified from Bergles et al., 2002

arachidonic acid (Fairman et al., 1998). The expression level of glial transporters steeply increases with development (Kugler and Schleyer, 2004). In line with this observation, it has been shown that astrocytic glutamate uptake also becomes faster during postnatal development (Diamond, 2005).

A single glutamate transporter cycle was estimated to last between 12 – 70 ms (Wadiche et al., 1995; Bergles and Jahr, 1998). This is much longer than glutamate dwell-time in the synaptic cleft (Clements et al., 1992). It has been argued that transporters should be located close to the site of synaptic transmission to rapidly uptake glutamate (Diamond and Jahr, 1997), although the fast rate of extracellular glutamate buffering depends mainly on its high-affinity transporter binding rather than the slow uptake cycle (Savtchenko et al., 2018). Indeed, immunoblots studies from adult rodent hippocampal astrocytes revealed that glutamate transporters are expressed in 8500 per μm^2 (Danbolt, 2001) and located mostly in fine astroglial protrusions next to the synapses (Oliet et al., 2001; Genoud et al., 2006). A pool of glutamate transporters available to bind escaping glutamate can be increased by lateral diffusion. A recent study using single-molecule tracking of GLT-1 has shown that these transporters are highly mobile (Murphy-Royal et al., 2015). Diffusion of transporters could be slowed down by TBOA inhibition or lower temperatures (22°C). On a longer-term scale, glutamate application was also shown to increase the transporter expression level (Duan et al., 1999). These findings suggest a mechanism by which released glutamate binds to transporters and enhances its lateral mobility, which in turn allows non-bound transporters to move in and take over.

1.7.4. Astrocytic morphological plasticity and glutamate uptake ensure synaptic autonomy

Fine astrocytic protrusions make up a large sponge-like structure, filling a substantial proportion of the interstitial space between nerve cell elements.

These small structures in majority of cases tightly enwrap sites of synaptic transmission, representing somewhat a physical barrier for diffusion (Bernardinelli et al., 2014b). In the *stratum radiatum* area of the hippocampus, more than half of all postsynaptic dendritic spines are in immediate contact with PAPs (Ventura and Harris, 1999; Witcher et al., 2007). In the CA3 area of the hippocampus, astrocytic protrusions almost completely enwrap mossy fibres synapses on CA3 pyramidal cells (Rollenhagen et al., 2007). In many cases, disruption of such a physical barrier represented by the astroglial shielding affects neurotransmitter diffusion in the extracellular space (Oliet et al., 2004). It was shown that reduction of astrocytic coverage facilitates glutamate diffusion in the extracellular space and enhances glutamate spillover (Henneberger et al., 2018). Physiological stimulation of acute slices with LTP (two alternative induction protocols) leads to a significant withdrawal of fine astrocytic protrusions and enhance inter-synaptic cross-talk between neighbouring networks. Physical barrier represented by astrocytic protrusions and expression of high-affinity glutamate transporters restricts the diffusion of glutamate and activation of receptors.

Glutamate transporters regulate glutamate dwell-time in the synaptic cleft and in this way regulate exposure of both synaptic and extrasynaptic receptors to glutamate. Genetic alterations of glutamate transporters have been shown to affect synaptic plasticity in different brain regions and impairs animal's behaviour. Glial glutamate transporters knockdown mice retain less than 10% of glutamate transport, demonstrating an important contribution of glial transporters to the total glutamate transport. These mice also develop hippocampal pathology accompanied by seizures, progressive motor deficit and die prematurely (Tanaka et al., 1997). Another study using knockout mice lacking GLT-1 showed impaired LTP induced by tetanic stimulation (Katagiri et al., 2001). However, this effect was rescued using a low concentration of NMDA receptor antagonists and thus suggesting that elevated extracellular level of glutamate predominantly activate NMDA receptors. Pharmacological inhibition of astrocytic glutamate receptors with TBOA was shown to promote long-term depression (LTD) induced by low-frequency stimulation, and also

lead to impairing of spatial memory (Wong et al., 2007). Impairment of astroglial glutamate uptake subjects various receptors to excessive glutamate exposure. For instance, blockade of astrocytic (but not neuronal) glutamate transporters boosts activation of interneuronal mGluRs in the *oriens lacunosum moleculare* area (Huang, 2004) and enhances NMDA receptors-mediated glutamate spillover in the hippocampus (Asztely, Erdemli and Kullmann, 1997; Scimemi, Fine and Kullmann, 2004). Interestingly, the elimination of glutamate transporters was predicted to have little effect on EPSC mediated by low-affinity AMPA receptors (Zheng et al., 2008). In conclusion, suppression of glutamate transporters is shown to downregulate LTP (Katagiri et al., 2001; Scimemi et al., 2009) and to enhance the magnitude of LTD (Brasnjo and Otis, 2001; Wong et al., 2007), thus affecting the LTP-LTD balance.

1.8. Rationale and research objectives

It is widely recognised that astrocytes help to shape and maintain synaptic transmission by providing efficient glutamate uptake through their excitatory amino acid transporters. This process is critical to the physiological functioning of neuronal networks in the brain; however, impairment of rapid glutamate clearance by astroglial has been associated with a range of neurological pathologies. Hence, the mechanism underpinning an efficient operation of glutamate transporter could be critical for further nomination as a potential therapeutic target. Yet, the exact machinery of perisynaptic glutamate transporter under varied regimes of synaptic transmission and its use-dependent modifications remains poorly understood. This is mainly associated with the technological limitations of monitoring and probing synapses and astroglia on a sub-microscopic scale. The overall goal of the present thesis was to take advantage of newly developed imaging methods, in order to

provide novel insights into the role of astrocytic glutamate uptake by regulating excitatory synaptic transmission and its use-dependent efficacy.

To achieve this goal, I divided my research strategy into four objectives, which are as follows:

1. To acquire all advanced skills and protocols with a two-photon imaging / uncaging / FLIM system integrated with patch-clamp, including calibration of fluorescent indicators for quantitative [Ca^{2+}] readout

Summary: Combination of two-photon excitation fluorescence imaging and patch-clamp electrophysiology provides a cutting-edge approach to monitor, probe synaptic, and astroglial function *in situ*, with the highest attainable resolution and sensitivity. My first practical goal was to master in-house system dedicated to such experiments (Femtonics 2D-Femto system), including all related preparation and data acquisition protocols. Chapter 3 reflects the results of this training. Evaluation of key astrocytic properties often relies on the understanding of Ca^{2+} signals generated in local compartments of astrocytes and neurons, in organised brain tissue. In chapter 3 of my experiments, I calibrated the fluorescent Ca^{2+} indicator OGB-1 for fluorescence lifetime-based readout of absolute Ca^{2+} concentration. The established calibration curve is used for further estimation of intracellular Ca^{2+} dynamics in astrocytes and presynaptic axonal boutons in brain tissue using both fluorescent intensity and FLIM methods. Here, I also compared different methods of indicators delivery to the astrocytic syncytium (bulk loading with AM dyes versus whole-cell delivery through patch-pipette).

2. To develop an experimental protocol for monitoring and measuring intracellular [Ca^{2+}] dynamics in astrocytes using fluorescent intensity and FLIM acquisitions *in situ*

Summary: Owing to several factors, fluorescent imaging of small structures in brain slices is a challenging task, including light scattering and absorption in the tissue. Hence, a balanced protocol is essential for accurate

estimation of Ca^{2+} activity in both astrocytes and presynaptic boutons. In chapter 4, I verified the methodology of dynamic [Ca^{2+}] monitoring as described in the preceding chapter. I also evaluated the sensitivity and technical feasibility of current methods in which fluorescent intensity and FLIM readout are monitored upon application of exogenous stimuli, such as dopamine and beta-amyloid peptide.

3. To determine how extracellular K^+ accumulation affects local glutamate uptake by astrocytes

Summary: In chapter 5, I reported the results of my experiments in which I recorded glutamate transporter current from individual astrocytes in response to single and repetitive stimulation of Schaffer collaterals, in acute hippocampal slices. This approach allowed me to assess the amount of released glutamate, and the rate of glutamate uptake by astrocytic transporters. Here, I also found how the accumulation of K^+ during intense synaptic activity enhances glutamate-dependent cross-talk between neighbouring excitatory synapses.

4. To investigate the role of astrocytic K^+ buffering (and glutamate uptake) to modulate presynaptic function using cell-targeting genetic and pharmacological manipulations

Summary: I split this objective into two research lines. In chapter 6, I employed genetic upregulation of Kir4.1 channels expression level in astrocytes via viral transduction and characterised the functional properties of transduced cells. In chapter 7, I evaluated how genetic upregulation of Kir4.1 in astrocytes affect presynaptic glutamate release during repetitive discharges. For that purpose, I adapted and used virally transduced optical glutamate sensors and monitored the probability of glutamate release at varying levels of extracellular [K^+].

Chapter 2: Methods

2.1. Acute slice preparation

2.1.1. Animals

Acute slices for probing dopamine and local amyloid betta application on local Ca^{2+} dynamics were obtained from P21–28 male Sprague-Dawley rats. The rest of the experiments were performed on acute slices from P21–28 male C57BL/6 or CA1-GluN1 knockout mouse (KO) mice (Tsien et al., 1996). For viral transduction, I used P0–3 C57BL/6 pups of both genders. The control animals for these experiments came from the C57BL/6 mice line and were injected with virus-free artificial cerebrospinal fluid (ACSF) solution. Animals were housed in a controlled environment with a 12 h light cycle. All experimental protocols involving animals were carried out in full compliance with the UK Home Office (Scientific Procedures) Act under the Home Office Project Licence PPL P2E0141 E1.

2.1.2. Viral transduction

Throughout experiments in this thesis, I used two adeno-associated viruses (AAVs): 1) a glutamate sensor expressed in neurons, AAV2/1h.Synap.SF-iGluSnFR-A184V (10^{10} GC/ml; Penn Vector Core, PA, USA), to monitor glutamate responses; and 2) a virus that upregulates the expression level of Kir4.1 channels in astrocytes, namely AAV9.pZac.2.1-gfaABC1D-tdTomato:rKcnj10 (10^{10} GC/ml; Vector Builder, IL, USA). AAV injections were performed to P0–3 C57BL/6 neonatal pups in a volume not exceeding 2.5 µL per hemisphere. After analgesia (carprofen, 5mg/kg) administration and sterilization of the scull with 70% ethanol the virus was

injected to a right lateral ventricle (2/5 of the distance from the lambda suture to the eye, ~3 mm deep) using a Hamilton needle (Jankowsky et al., 2014). Injected with the virus pups were labelled with tattoo ink. Then animals were recovered in the home cage and monitored for signs of hypothermia, infection or distress. Acute hippocampal slices were prepared 2–3 weeks after AAV injection.

2.1.3. Slice preparation

Animals were anaesthetised by 5% isoflurane inhalation. Adequate anaesthesia was ensured by a lack of pedal reflexes; this was followed by cervical dislocation and decapitation. After opening up the skull, a pre-cooled scalpel was used to separate hemispheres and cut prefrontal cortex and cerebellum from the rest of the brain (Figure 2.1a). Then, the brain was extracted from the cranium and submerged in an ice-cold sucrose-based slicing solution containing (in mM): NaCl, 60; KCl, 2.5; NaH_2PO_4, 1.25; $NaHCO_3$, 26; D-glucose, 15; sucrose, 105; $CaCl_2$, 0.5; and $MgCl_2$, 7 (osmolality-adjusted to 310 mOsm). Hemispheres were subsequently separated and the hippocampi isolated. To obtain 350 µm-thick transverse slices both hippocampi were placed in an “E”-shaped agar block (Figure 2.1b) and transferred to the chamber of a Leica VT 1200S vibratome (angled to 30º, slicing speed adjusted to 0.10-0.12mm/s) filled with pre-cooled slicing solution (Figure 2.1b).

2.1.4. Slice incubation

For recovery slices were left for 15–20 min in slicing solution and for 40 min at 34°C in ACSF solution, containing (in mM): NaCl, 125; KCl, 2.5; NaH_2PO_4, 1.25; $NaHCO_3$, 26; D-glucose, 18; $CaCl_2$, 2; $MgSO_4$, 1.3

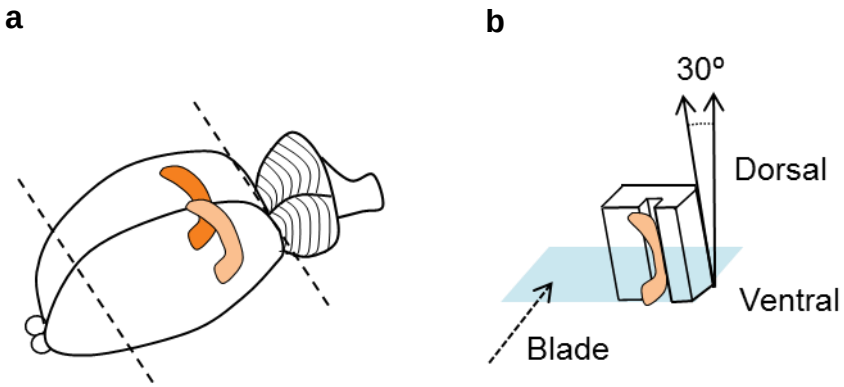

Figure 2.1 Schematic illustration of acute hippocampal slices preparation

a- Schematic representation of the separation of prefrontal cortex and cerebellum from the brain is depicted by dash lines
b- Schematic representation of isolated hippocampi placed to the "E"-shaped agar block to obtain transversal slices.

(osmolarity-adjusted to 295–305 mOsm). Slices were incubated for at least one hour before recording. In order to maintain the pH of the solutions, they were continuously oxygenated with 95% O_2/5% CO_2. To monitor Ca^{2+} activity, acute slices were bulk-loaded with the high-affinity astrocytic Ca^{2+} indicator Oregon Green BAPTA-1 (OGB-1; Thermo Fisher Scientific, MA, USA) and the morphology marker Sulforhodamine-101 (SR-101; Sigma-Aldrich, MO, USA) according to the following protocol:

1) incubate for at least 45 min in ACSF solution;

2) incubate in 20 µM SR-101 for 10 min at 34°C;

3) wash 3 times in ACSF solution;

4) incubate in 10 µM SR-101 and 5 µM OGB-1 for 40 min at 34°C;

5) wash 3 times in ACSF solution;

6) incubate in ACSF solution for 30 min.

2.2. Electrophysiology

2.2.1. Basic microscope configuration

All electrophysiological recordings were performed using a Femto-2D system (Femtonics, Hungary), based on an Olympus BX61WI microscope equipped with motorised micromanipulators and a recording submersion chamber, fully adapted for brain slice experiments. To maintain physiological conditions throughout all experiments, acute slices were perfused with oxygenated ACSF solution at 32–34ºC. The temperature of the extracellular solution was maintained by the TC07 thermo-controller (Luigs and Neumann, Germany). For whole-cell patch-clamp recording, a micropipette filled with an internal solution was set in a holder with a chloride silver wire. The microelectrode holder was then inserted into headstage (CV-7B; Axon Molecular Devices, CA, USA). Signals were amplified by a Multiclamp 700B Amplifier and the signal was converted from analogue to digital at 10 kHz using a digitiser (Digidata 1550; Molecular Devices, CA, USA). The software package WinWCP v5.4.6 (University of Strathclyde, UK) was used for signal acquisition.

2.2.2. Micropipettes and internal solutions

For patch-clamp recordings and local beta-amyloid peptide application, micropipettes were pulled from borosilicate–standard wall filament glass (G150F-4; Warner Instruments, CT, USA) and had 4–5 MΩ resistance. For whole-cell recordings from astrocytes pipettes were filled with a potassium methanesulfonate (KMS)-based solution containing (in mM): KCH_3O_3S, 135; HEPES, 10; $MgCl_2$, 4; phosphocreatine disodium, 10; Na_2ATP, 10; and NaGTP 0.4 (pH-adjusted to 7.2 with KOH; osmolarity-adjusted to 290–295 mOsM). Whole-cell recordings from pyramidal neurons were obtained using pipettes filled with a modified solution containing (in mM): KCH_3O_3S, 130;

NaCl, 8; HEPES, 10; and phosphocreatine disodium, 10; Na_2GTP, 0.4; MgATP, 4; sodium ascorbate, 3 (pH-adjusted to 7.2 with KOH; osmolarity-adjusted to 290–295 mOsM). In some experiments, to prevent K^+ efflux, KCH_3SO_3 was replaced with N-methyl-D-glucamine (NMDG)-CH_3SO_3.

2.2.3. Whole-cell patch-clamp recordings

After visualisation of the cell of interest using light microscopy, a micropipette was filled with the appropriate intracellular solution. Extra care was taken to ensure that the chloride silver wire was in contact with the internal solution. With the help of motorised manipulators, the patch pipette was lowered down to the cell of interest, and a small positive pressure was applied to prevent pipette clogging. When the internal solution contained fluorescent dyes, positive pressure was applied before lowering the pipette to the brain tissue, to limit dye diffusion and accumulation in neighbouring cells. After observing membrane invagination, the positive pressure was released to form a gigaOhm seal. Finally, negative pressure was applied to establish a whole-cell configuration.

2.2.4. Electrophysiological characterisation of astrocytes

For the purpose of my investigations, I recorded protoplasmic hippocampal astrocytes located in the CA1 *stratum radiatum* region (Figure 2.2a). These astrocytes were identified by their small soma size (~10 µm), low input resistance (~ 10–20 MΩ) and close to -80 mV (-82.66 ± 1.85 mV (*n* = 9))

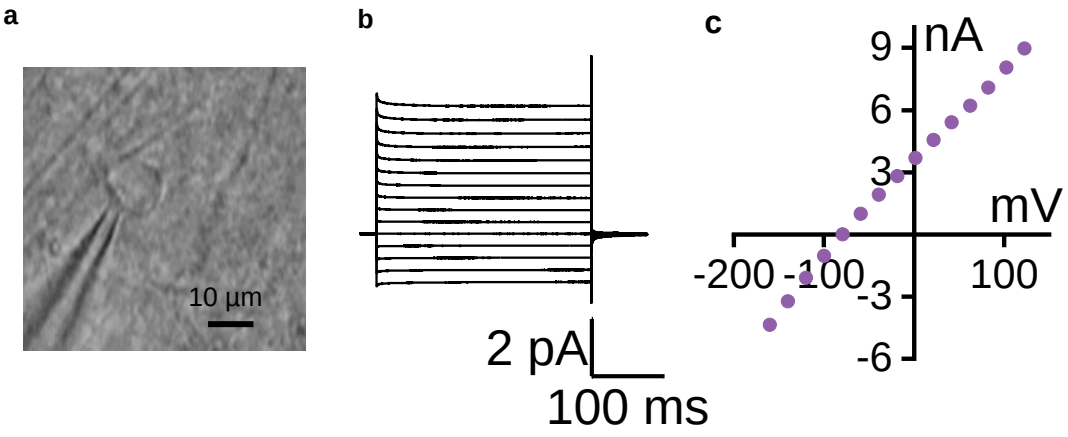

Figure 2.2 Confirmation of electrically-passive properties of astrocytes in the *stratum radiatum* region

a- Typical astrocyte located in the *stratum radiatum* region in whole-cell configuration, with the patch pipette filled with KMS-based internal solution depicted on the left
b- Whole-cell recording from the astrocyte depicted in a; recorded current changes for voltage step injections
c- A linear *I-V* curve for an astrocyte showing their passive electrical properties.

resting membrane potential. The resting membrane potential was carefully monitored throughout the experiments in current-clamp mode. Electrically passive membrane properties of astroglia were confirmed based on their linear current-voltage (*I-V*) relationship; in voltage-clamp mode, I injected voltage steps of progressively increasing amplitudes. The recorded current responses established a linear *I-V* curve (Figure 2.2b–c).

2.2.5. Electrophysiological characterisation of CA1 pyramidal neurons

Throughout the thesis, I performed recordings from hippocampal CA1 pyramidal neurons. They were identified by their smooth pyramidal-shaped soma (~30 µm), location in CA1 cellular layer and resting membrane potential of around -70 mV. The resting membrane potential was obtained at the beginning and the end of each experiment to ensure the stability of the recording.

2.2.6. Extracellular stimulation of Schaffer collaterals

Synaptic transmission in CA3-CA1 synapses was induced by stimulation of the Schaffer collaterals with a concentric electrode (FHC; ME, USA), placed at least 200 µm away from the cell of interest. The electrode was connected to a constant current stimulator (Digitimer DS3; Digitimer Ltd, UK). The duration of each stimulus was set to 200 µs throughout all recordings. Stimulation strength was adjusted to induce a response within a selected range: 6–10 pA for glutamate transporter currents, and 6–10 mV for excitatory postsynaptic potential responses (EPSPs). Stimulation of independent afferent pathways was achieved with two concentric electrodes, placed 400 µm away from each other, in opposing directions from the recording cell. High-frequency stimulation (HFS) consisted of 100 Hz trains of 1-s duration to the “active” pathway.

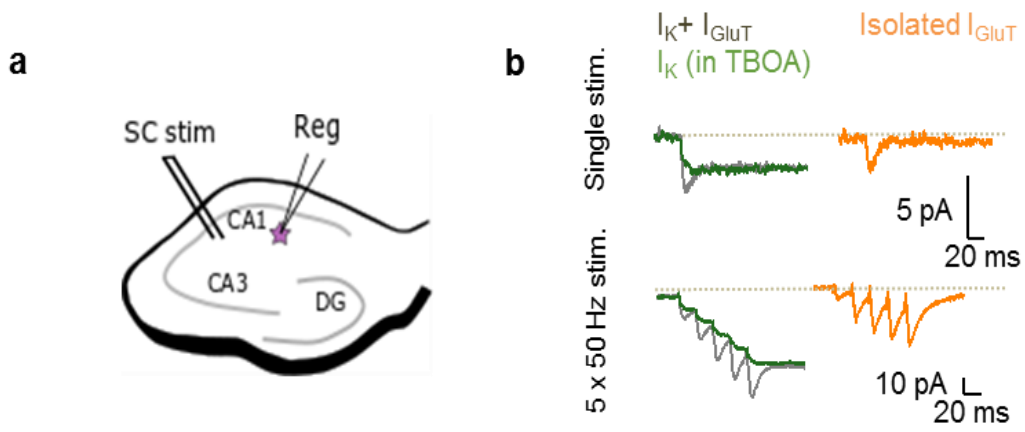

Figure 2.3 Glutamate transporter current recording from hippocampal astrocytes

a- Schematic illustration of electrode positioning for evoking inward currents in astrocytes. The concentric electrode was placed in the Schaffer collateral region in order to mimic CA3-CA1 synaptic transmission

b- Delivery of single or multiple stimuli (5 × 50 Hz) to the concentric electrode placed evokes inward currents in an astrocyte, representing a combination of the K^+ current and glutamate transporter current (I_K+I_{GluT}, grey). Application of the glutamate transporter antagonist DL-TBOA (50 µM) allows to record the K^+ current (I_K, green). Further post-hoc subtraction of the K^+ current from the mixed inward current allows to isolate the glutamate transporter current (I_{GluT}, orange).

2.2.7. Glutamate transporter current recordings from astrocytes

Glutamate transporter currents were recorded in voltage-clamp mode either with single or repetitive stimulation of the Schaffer collaterals (5 stimuli × 50 Hz) (Figure 2.3a–b). To pharmacologically separate the glutamate transporter currents from K^+ inward currents, I performed the following protocol:

1) recording of the inward current, representing both K^+ and glutamate currents;

2) application of the glutamate transporter antagonist DL-TBOA to the perfusion solution, with the subsequent recording of the K^+ current;

3) post-hoc subtraction of the K^+ current from the mixed current and glutamate transporter current measurement.

Glutamate transporter block was achieved by bath application of the glutamate transporter antagonist DL-TBOA (50 µM). At least 15 min was allowed for the antagonist to wash in.

2.2.8. Beta-amyloid peptide aggregation protocol

A Biosep-SEC-s2000 size-exclusion column (Phenomenex, CA, USA) was employed to purify HiLyte Fluor 647 beta-amyloid peptide (Aβ1–42). Prior to purification, the peptide was kept on ice, then, after purification was immediately frozen and stored at −80ºC. On the day of the experiment, purified Aβ1–42 was diluted in PBS to 500 nM and shaken at 200 rpm at 37ºC for 5 h. After that, experimental aliquots were centrifuged at 14,500 g for 10 min and then diluted to the required concentration in L15 medium (Sigma-Aldrich, MO, USA). Aβ1–42 was applied through a puff pipette positioned next to an astrocyte or CA1 pyramidal neuron of interest.

2.2.9. Chemical compounds

The list of chemical reagents purchased from Tocris Bioscience (UK) is summarised in Table 2.1. $BaCl_2$ was used either intracellularly or

extracellularly to block Kir channels. In chapter 5, I supplemented the internal solution with $BaCl_2$ to selectively eliminate K^+ channels in the patch-clamped astrocyte. In chapter 6, I used bulk extracellular $BaCl_2$ (200 µM) application. Reagents (e.g. salts for intracellular and extracellular solutions) were purchased from Sigma-Aldrich (MO, USA).

Chemical compound name	Concentration used, µM	Target
NBQX	25	AMPA receptor
D-APV	50	NMDA receptor
(+)-MK 801 maleate	4	NMDA receptor
MCPG	200	mGlu receptor (group I/II)
LY 367385	100	mGlu receptor (group Ia)
LY 341495	0.5	mGlu receptor (group II)
DL-TBOA	50	EAATs (transporters)
TTX	1	Na^+ channel
MPEP	1	mGluR5 receptor
PTX	100	$GABA_A$ receptor
CGP 55845	1	$GABA_B$ receptor
SCH 23390	20	Dopamine receptor, type-1 (D1/D5)

Table 2.1 Outline of used chemical compounds, their actions and concentrations

2.3. Two-photon imaging recordings

2.3.1. Ca^{2+}-sensitive fluorescent dye

The objectives of this thesis include studying changes in basal [Ca^{2+}] and Ca^{2+} transients upon exposure to exogenous substrates. According to the literature, the basal [Ca^{2+}] in brain cells is estimated to be around 50–140 nM (Zheng et al., 2015), with the capacity to be elevated several-fold in response to stimulation. An appropriate Ca^{2+}-sensitive indicator should have a suitable dissociation constant (Kd) (close to the midpoint of the expected Ca^{2+} range) and the capacity to change its fluorescence lifetime upon binding to Ca^{2+} (Table 2.2). Among a large variety of Ca^{2+}-sensitive fluorescent dyes, Oregon Green BAPTA dyes family demonstrate changes in lifetime decay time upon binding to Ca^{2+} in the 10–500 nM range, allowing the detection of both baseline [Ca^{2+}] and transient responses. Oregon Green 488 BAPTA-2 (OGB-2) exhibits very low fluorescence in the absence of Ca^{2+} while showing at least a 37-fold increase at a saturating level of Ca^{2+} (Kd(Ca^{2+}) ≈ 580 nM). The respective merits of the Oregon Green 488 BAPTA-1 (OGB-1) indicator include its 14-fold increase in fluorescence intensity upon Ca^{2+} binding and a Kd of ~170 nM, making the indicator more sensitive to small changes in basal [Ca^{2+}]. Additionally, OGB-1 dye fluorophore lifetime in the absence of Ca^{2+} (τ_{free}) is considerably larger than instrumental noise (introduced by detectors or lasers) of the imaging system (Zheng, Jensen and Rusakov, 2018). Hence, OGB-1 represents a more suitable Ca^{2+}-sensitive dye to estimate nanomolar changes of basal [Ca^{2+}] and its transients.

Fluorophore	λ_{em} max (nm)	τ_{free} (ns)	τ_{bound} (ns)
OGB-1 (Ca^{2+})	523	0.73	4
OGB-2 (Ca^{2+})	523	0.73	4.1
Calcium Green 1(Ca^{2+})	506	0.92	3.6
Alexa Fluor 488	519	4.1	4.1
Alexa Fluor 594	617	3.8	3.8

Table 2.2 Basic FLIM properties of conventional fluorophores

The list of common fluorophores with their emission peak wavelength (λ_{em} max), and the characteristic fluorescence lifetime for the fluorophore in the absence (τ_{free}) and saturating presence (τ_{bound}) of Ca^{2+}.

Modified from Zheng, Jensen and Rusakov, 2018

2.3.2. Morphological-tracing fluorescent dye

For detailed visualisation of the region of interest, the OGB-1 dye needs to be supplemented with a morphological-tracing dye. The combination of two fluorescent indicators was primarily based on their spectral properties, levels of brightness, photostability, pH insensitivity and water solubility. The wide selection colours from the Alexa Fluor family allowed me to choose an indicator with an optimal excitation/emission wavelength that did not overlap with the OGB-1 spectrum. Alexa Fluor-594 (Alexa-594; Thermo Fisher Scientific, MA, USA) is a red-shifted dye with maximum emission at 617 nm. The selected morphological-tracing dye did not change the fluorophore lifetime upon Ca^{2+} binding and did not contaminate the recorded Ca^{2+} signal (Table 2.2). Hence, for the fluorescent intensity and lifetime experiments, a combination of two dyes was added to an internal solution, comprising Alexa-594 (50 µM) as a

morphological tracer and OGB-1 (200 µM) as a Ca^{2+}-sensitive indicator. For experiments on the direct effect of Aβ1–42 on [Ca^{2+}] changes, slices were bulk-loaded with OGB-1 acetoxymethyl (AM) esters (5 µM) and SR-101 (10 µM).

2.3.3. Microscope configuration

I used a Femto-2D FLIM imaging system (Figure 2.4) based on an Olympus BX61WI microscope, coupled with a Time-Correlated Single Photon Counting (TCSPC) unit (Becker and Hickl GmbH, Germany) and FLIM detectors (Femtonics, Hungary). Throughout all experiments, I used a high-resolution multiphoton Olympus XL Plan N 25× water immersion objective (NA 1.05) and employed digital zooming (2×–14×) to acquire signals from small cellular structures. The imaging system was equipped with two tunable Ti: Sapphire MaiTai infrared lasers (pulsing at 80 MHz; pulse width, ~220 fs; Newport Spectra-Physics, UK). Excited emission from the sample was split into two channels by dichroic mirrors. A 720 nm short-pass filter was used to shelter high-sensitive detectors from escaping light from the laser. Additionally, emission filters were employed in front of the detectors to separate fluorescence signals emitted from different fluorophores: 500–530 nm (for OGB-1 and iGluSnFR*)* and 540–700 nm (for SR-101, Alexa-594 and tdTomato). The two-photon laser was tuned to a wavelength of: 800 nm for optimal OGB-1, SR-101 and Alexa-594 excitation; 910 nm to monitor glutamate release from individual axonal boutons expressing iGluSnFR, or 940 nm for imaging the red fluorescent protein tdTomato. To reduce phototoxicity, laser power under the objective was carefully maintained below 8 mW throughout all experiments. For FLIM an acquisition imaging system was implemented with the TCSPC unit. This unit measures the time difference between the excitation light pulse delivered from laser source and the following emitted photons from the sample.

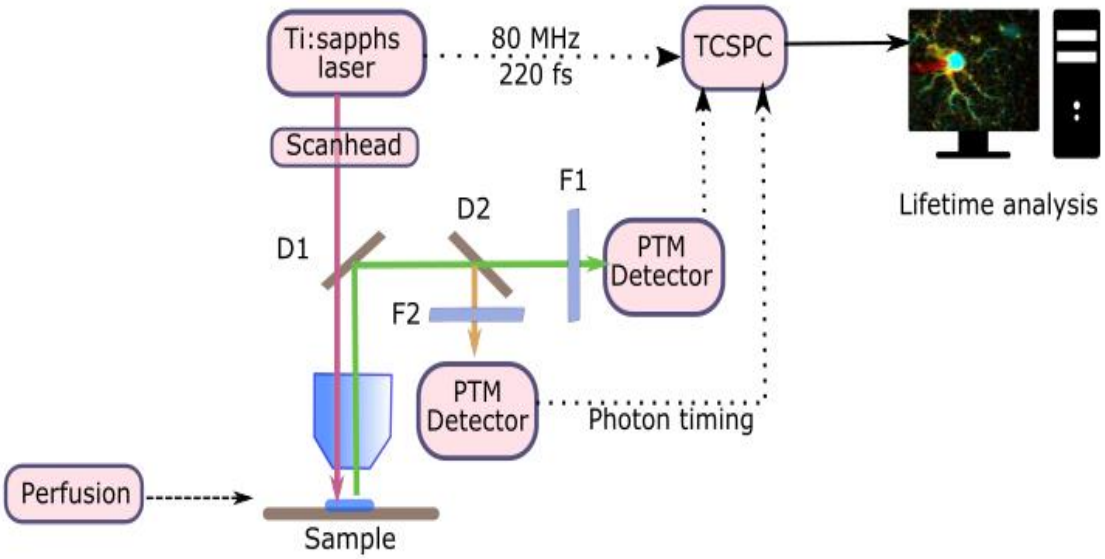

Figure 2.4 Schematic illustration of the Femto-2D FLIM imaging system

The Ti: Sapphire laser emits femtosecond infrared laser pulses (80 MHz, ~220 fs), which are capable of exciting fluorescence signals in a sample under the objective. With the help of dichroic mirrors (D1, D2), the resulting emission is split and amplified by photomultiplier detectors (PMT Detector). Emission filters (F1, F2) were set up in front of the detectors to separate fluorescence signals emitted from different fluorophores. The TCSPC stores the time delay between the first laser pulse and the arrival of the single-photon signal to the detector

2.3.4. Recording software

Separate software was used to acquire fluorescence intensity measurements and the FLIM signal. Acquisition of fluorescence intensity was performed in the MATLAB–based MES software package (Femtonics, Hungary). This allows the determination of recording parameters, and the collection, storage and analysis of data sets. The Becker and Heckl TCSPC module was controlled by Multi SPC software (SPCM; Becker and Heckl

GmbH, Germany). This software allows scanning parameters to be set and controlled, as well as the loading and saving of acquired data.

2.3.5. Fluorescence intensity and time-resolved Ca^{2+} imaging recordings from astrocytes

Two-photon excitation of the Ca^{2+}-sensitive fluorescent dyes was accomplished using femtosecond pulses of an infrared laser. Infrared light allows scattering to be minimised and imaging from a focal plane up to 100 µm deep into the organised brain tissue. Excitation of fluorophores only occurs in a narrow focal plane, reducing photobleaching and background noise. Delivery of the dye to the astrocytic syncytium was performed either with bulk loading in AM form or via direct delivery. The latter was accomplished through whole-cell patch clamping of an astrocyte. Further dye diffusion through gap junctions allows Ca^{2+} dynamics to be recorded from neighbouring astrocytes. At least 45 min was allowed for dye diffusion and equilibration. The Alexa-594 channel was used to identify a region of interest and recorded along with the OGB-1 emission channel. An average frame scan (256 × 256 pixels) included 2–3 astrocytic somas. Frame images were acquired in a meta protocol sequence, in which a 120–300-s frame scan was followed by a 5-s pause. This non-scanning gap allowed for the Z-drift of the focal plane to be adjusted (this is represented by the staggered trace shape shown in Figure 4.3c). Unless otherwise stated, images were recorded at 2 Hz frequency. During recording to estimate whether photon count is sufficient for further analysis I manually monitored pixel photon count from the dimmest part of the sample and stop acquisition once the value reached 1,000. FLIM recordings of [Ca^{2+}] from astrocytes connected via gap junctions were acquired at a laser line scanning rate of 500 lines/s and stored as a 256 × 512 × 512 x n (t,x,y,T) data cube, which represented an x-y image with the distribution of ns decay time (t) of photons at each pixel over the frame duration (T).

2.3.6. Axon tracing and spiral-scan acquisition from presynaptic boutons

To trace the axonal arbour, I introduced Alexa-594 (50 µM) into the internal solution. The Ca^{2+} sensitive dye OGB-1 (300 µM) was used to measure [Ca^{2+}] changes via FLIM imaging. Axons were identified by their smooth morphology and followed in frame scan mode from the cell soma until the first bouton was encountered. Next, a spiral-scan was performed over the bouton. The spiral-scan always started at the centre of the bouton and spread to the periphery with a 0.15–0.2 µm pitch size (Jensen et al., 2017). The shape of the scan mimicked the morphological shape of the bouton. Typical line-scan dwell-time was 1.0–1.5 ms, thus providing a comprehensive, high-resolution readout of axonal fluorescence. The spiral-scan approach was also used to record quantal glutamate release from individual boutons. This parameter was estimated from fluorescence intensity measurements. Spiral-scans were recorded by both standard analogue integration in the Femtonics MES and with the TCSPC mode in the Becker and Hickl SPCM using dual HPM-100 hybrid detectors which record changes in fluorescence intensity as well as FLIM readout.

2.4. Data analysis

2.4.1. Glutamate transporter current

For transporter current analysis, I created a script in MATLAB. Electrophysiological data files were loaded in MATLAB in ABF format. After setting parameters for the baseline, traces for the same condition were averaged. Transporter current was then isolated by point-by-point subtraction of the K^+ current from the combined current. This procedure was performed for both single and repetitive stimulations. Further analyses included finding the maximum amplitude in the region of interest and the decay time (Ƭdecay). The

amplitudes obtained were then normalised to single stimulation amplitude. The decay time was calculated as the time necessary for the final amplitude to decay to 1/e (≈ 0.37) of its maximal value.

2.4.2. Excitatory postsynaptic currents

EPSPs analysis was performed in the Clampfit 10.6 (Molecular Devices, CA, USA) software package. The ABF files obtained previously were imported into the program. After selecting the baseline and the region of interest, traces were averaged. Decay time was calculated from the time of the final amplitude until the traces reduced to 1/e ≈ 0.37 of its maximal value. The decay time from repetitive stimulation was then normalised to that of the single stimulation to assess facilitation of EPSPs.

2.4.3. Ba^{2+}-sensitive *I-V* curve

Data files recorded in WinWCP and pClamp were imported to Clampfit 10.6 for further analysis. Traces from the same condition were averaged and then baseline and region of interest were selected manually. The baseline was set before stimulation and included at least 100 ms during which a region of interest was selected over steady-state currents, which occur toward the end of the 300 ms step. Traces recorded during application of $BaCl_2$ were subtracted from control traces to obtain Ba^{2+}-sensitive currents.

2.4.4. Two-photon excitation imaging

The fluorescence intensity and lifetime changes were analysed in the MATLAB-based Fluorescent Imaging Analysis Software (FIMAS) toolbox (https://github.com/zhengkaiyu/FIMAS). This toolbox was created by Dr Kaiyu Zheng and allows analyses of intensity measurements and FLIM data to be performed.

Fluorescent intensity data

Files in MES format were loaded into the FIMAS toolbox. Estimation of astrocytic [Ca^{2+}] dynamics was assigned to the soma of the cells based on the SR-101 channel. For each region, the OGB-1 signal was normalised to the averaged fluorescence from the Ca^{2+} transient-free region, to estimate the ΔF/F signal. The signal was corrected for background noise, by subtracting the average background fluorescence recorded from an area without visible fluorescence. Additionally, the signal was corrected for dark noise of detectors, by subtracting averaged intensity signal, recorded with closed shutters. A similar approach was employed to calculate the fluorescence intensity changes in individual presynaptic boutons. To calculate ΔF/F, the OGB-1 signal was normalised to the averaged fluorescence prior to stimulation.

FLIM data

For FLIM data analysis I used an approach based on the ratiometric method of normalised total count (NTC). This method represents computationally economical approach and as an output provide a single-value for estimated Ca^{2+} (Zheng et al., 2015; Jensen et al., 2017). Relatively long acquisitions time required for the NTC approach restricts its application for measurements of rapid Ca^{2+} changes. The critical parameter for successful calculation includes sufficient amount of collected photons towards the end of integration interval. Thus, special care was taken during image acquisitions to

obtain required amount of photons. Firstly, data files in SPC format were loaded into the FIMAS toolbox. The Alexa-594 channel was used to assign regions of interest. Then the dimmest part from the region was used to select appropriate level of binning that would give at least 5-10 photons toward the end of integrated area. The chosen binning level then was applied to each pixel in the region of interest. After that obtained decay profile was normalised to its maximum value. To obtain NTC value the trace was integrated from the peak over 9-ns interval. The final step for FLIM analysis includes transformation of the obtained NTC value to the estimated [Ca^{2+}] value. It was done using inverted logistic function, measured during the calibration process in chapter 3.

2.4.5. Sampling and statistics

Throughout experiments in this thesis, I used no more than two slices per animal and recorded 3–4 cells per slice. One exception to this is in chapter 5, Figure 5.5.6; due to the complexity of the methodological approach used (whole-cell patch-clamp recording from a pyramidal neuron with iGluSnFR expression), individual spines were analysed as statistical units. In the rest of the experiments, individual cells were analysed as statistical units. Throughout all experiments, I monitored the physiological health of the recorded cells. Cells showing more than 20% change in their series resistance were excluded from further analysis. Cells showing insufficient fluorescence signal for FLIM acquisition were also discarded.

Samples were tested for normality with the Shapiro–Wilk test; for populations with a normal distribution unpaired Student's t-test was used to assess the difference between two independent populations. Paired t-test was used for comparison of means of related groups. The one-way analysis's of variance (ANOVA) with repeated measures (RM) was used to compare unpaired means between two groups in relation to one factor, while two-way ANOVA with RM was used to compare differences between three or more

groups in relation for two independent variables. For comparison of two non-normally distributed data groups, the Mann-Whitney test was used.

Chapter 3

Advancing microscopic imaging: Monitoring intracellular Ca^{2+} dynamics *in situ* using fluorescence intensity and lifetime measurements

3.1 Introduction

In brain cells, intracellular Ca^{2+} dynamics are a key regulator of signalling cascades, such as fusion and release of neurotransmitters (Katz and Miledi, 1968) or communication within and between electrically non-excitable astroglial cells (Halassa and Haydon, 2010; Di Castro et al., 2011). Intracellular Ca^{2+} pumps and buffers allow most cells to maintain their resting [Ca^{2+}] in a narrow range, from 50–200 nM (Parpura and Haydon, 2000; Zheng et al., 2015). Managing basal Ca^{2+} at low levels enables a wide dynamic range for Ca^{2+}-dependent cascades. Accurate monitoring of internal Ca^{2+} signalling both in neurons and in the astrocytic syncytium remains an essential method for the understanding of Ca^{2+}-mediated mechanisms. Pioneering work investigating intracellular Ca^{2+} dynamics was performed in cultures (Timmerman and Ashley, 1986; Malgaroli et al., 1987; Baylor and Hollingworth, 1988), with the Ca^{2+} concentration estimated as the ratio between two fluorescence intensities of ratiometric dyes, such as Fura-2 and Indo-1 (Lückhoff, 1986; Tsien, 1989). The extensive dynamic range of ratiometric dyes allows them to accurately quantify both baseline and transient activity (Grynkiewicz et al., 1985). Despite this, they have several limitations, restricting the application of such indicators in acute brain slices. For instance, the AM ester form of Indo-1 is fluorescent, and it is possible to underestimate Ca^{2+} changes in cells in which the dye is not entirely de-esterified. AM esterase accumulation in the extracellular space might produce a toxic effect, especially in organised brain tissue in which

diffusion is limited (Kao et al., 2010). Ratiometric dyes possess considerably less affinity to Ca^{2+} in cells compared to solutions which are strongly dependent from polarity, viscosity, ionic strength and the temperature of the environment (Dustin, 2001; Haugland, 2002). Critically, the main factor limiting the application of ratiometric dyes in brain tissue is light absorption and scattering within the sample. Because absorption and scattering are strongly dependent on the wavelength of the light, the ratios between two chromatically separated light signals (in either the emission or excitation channel) will vary according to the depth in optically turbid preparations, such as brain tissue. In addition, these indicators tend to generate a low signal-to-noise ratio when acquired from relatively small-sized astrocytic somas (~10–15 µm) and axonal boutons (~1–5 µm). To overcome these issues when imaging organised brain tissue, recording of Ca^{2+} dynamics has commonly been carried out using fluorescence intensity-based measures, using dyes excited within the visible light spectrum, such as OGB-1, Calcium Green 1, or Fluo-4 (Maravall et al., 2000; Grienberger and Konnerth, 2012; Chen et al., 2013). Upon Ca^{2+} binding, these indicators increase their quantum efficiency without shifting their absorption spectra. Although the bound/free ratio for these dyes is normally high, they generate a relatively high signal-to-noise ratio suitable for imaging small cellular compartments (Zheng et al., 2015; Jensen et al., 2017). With recent technological advances, in particular the fluorescence lifetime imaging microscopy (FLIM) technique, it has become possible to measure the lifetime of a fluorophore in real-time and to estimate the ionic concentration, even for low [Ca^{2+}] under resting conditions (Kuchibhotla et al., 2009; Zheng et al., 2018). A considerable benefit of this technique is that the fluorescence lifetime of an excited fluorophore does not depend on its concentration or on small Z-drifts of the focal plane, which might occur during scanning. It has been shown that FLIM readout is independent of local environmental parameters in the physiological range, including pH, temperature, micro-viscosity, [Mg^{2+}] and [Zn^{2+}] (Zheng et al., 2015). Furthermore, FLIM measurement does not appear susceptible to artefacts arising from light scattering in the tissue,

photobleaching, or physiological changes in the local environment (Zheng et al., 2015).

In this chapter, I report an adapted methodology for monitoring intracellular Ca^{2+} activity (in astrocytes and presynaptic axonal boutons) in brain slices using fluorescence intensity and FLIM measurements. In particular, the first section of this chapter describes the calibration of the fluorescent indicator OGB-1 for Ca^{2+}-sensitive FLIM readout. Calibration *in vitro* using glass coverslips with known (clamped) [Ca^{2+}] establishes a calibration curve required for further data analysis. Since one crucial factor limiting imaging in organised brain tissue is unreliable cell labelling, in the second section I compare different methods of indicator delivery to astroglia: bulk loading with AM dyes versus whole-cell delivery through a patch pipette. In the last section of this chapter, I describe a new approach to evaluate Ca^{2+} signals in axonal boutons using both intensity and FLIM readout of OGB-1.

3.2. Methods

Throughout the experiments in this chapter, I used a Femto-2D FLIM imaging system, which was integrated with a patch-clamp electrophysiology system, two femtosecond pulse MaiTai lasers, and a FLIM unit. Monitoring of Ca^{2+} activity in both astrocytes and neurons was performed in acute brain slices from P21–25 male C57BL/6 mice. Slices were either incubated with the high-affinity, cell-permeable Ca^{2+} dye OGB-1 AM together with astrocytic marker SR-101, or loaded with OGB-1 and Alexa-594 through a patch pipette.

Two-photon excitation frame images of astrocytic somata were acquired to measure changes in OGB-1 fluorescence intensity ($\Delta F/F$) and FLIM readout. Assessment of [Ca^{2+}] dynamics in axonal boutons was performed with dyes delivered directly through the patch pipette to pyramidal neurons. After whole-cell break-in, I allowed sufficient time for dyes to equilibrate across the cell, and then followed the axon, in frame-scan mode,

until the first bouton had been identified. Next, a spiral-shaped line scan was employed to acquire Ca^{2+} dynamics over the visible bouton area. Each of these line-scans started in the centre of the bouton with a total dwell time of 1–2 ms. Photon counts acquired through spiral scans were recorded using the TCSPC mode in the Becker and Hickl SPCM software, using dual HPM-100 hybrid detectors recording both fluorescence intensity and FLIM readout. The FLIM line-scan data were collected and stored in a t × x × y × T data cube representing an x-y image with the distribution of nanosecond decay times (t) of photons at each pixel over the frame duration (T).

Post-hoc FLIM analyses were performed in a custom-made data analysis toolbox, which is available online (https://github.com/zhengkaiyu/FI-MAS). The fluorescence decay curve (lifetime photon counts) was integrated over the 9 ns period and normalised to the maximum value, as described in Zheng, Jensen and Rusakov, 2018. Data from up to 5–10 neighbouring pixels were averaged to ensure that the FLIM decay traces had sufficient counts towards the tail of the decay (8–12 ns post-pulse). Data from a single trial was normally enough for boutons located closer to the surface of the tissue, whereas, for deeper-located boutons, several repetitions were required to accurately estimate Ca^{2+} dynamics evoked by an AP.

3.3. Results

3.3.1. OGB-1 calibration for [Ca^{2+}] readout

First, I calibrated the OGB-1 fluorescence lifetime for readout of [Ca^{2+}]. To accomplish this, I measured the lifetime of OGB-1 in intracellular solutions with an adjusted Ca^{2+} buffer and clamped [Ca^{2+}]. The pH was adjusted using KOH, and the KCl concentration was adjusted accordingly to keep the ionic constituents of the solution unchanged (Table 3.1). Estimated [Ca^{2+}] was calculated using MAXCHELATOR program (https://somapp.ucdmc.ucdavis.

edupharmacology/bers/maxchelator/). On the day of calibration, I prepared two solutions, with high (HS) and low [Ca^{2+}](LS). In addition, I prepared a 10 mM OGB-1 stock solution (eppendorf tube labelled ; 'F' in Figure 3.1). I added the required volume of OGB-1 to both the HS and the LS eppendorf tubes so that the total concentration reached 20 µM. Then I used a mixing eppendorf tube (labelled 'M' in Figure 3.1) to prepare a range of calibration solutions with different [Ca^{2+}] from 0–2,310 nM. The desired concentration of [Ca^{2+}] in the solution was reached by removing a particular volume of mixed solution (Figure 3.1, Table 3.2) and replacing it with HS solution.

Compound	Low [Ca^{2+}] solution, mM	High [Ca^{2+}] solution, mM
KMS	105	105
HEPES	10	10
Na-phosphocreatine	10	10
$MgCl_2$	4	4
Na_2ATP	4	4
NaGTP	0.4	0.4
BAPTA	10	5
BAPTA tetrapotassium salt	0	5
Potassium chloride	20	0
$CaCl\text{-}2H_2O$	0	10

Table 3.1 Composition of [Ca^{2+}] calibration solutions

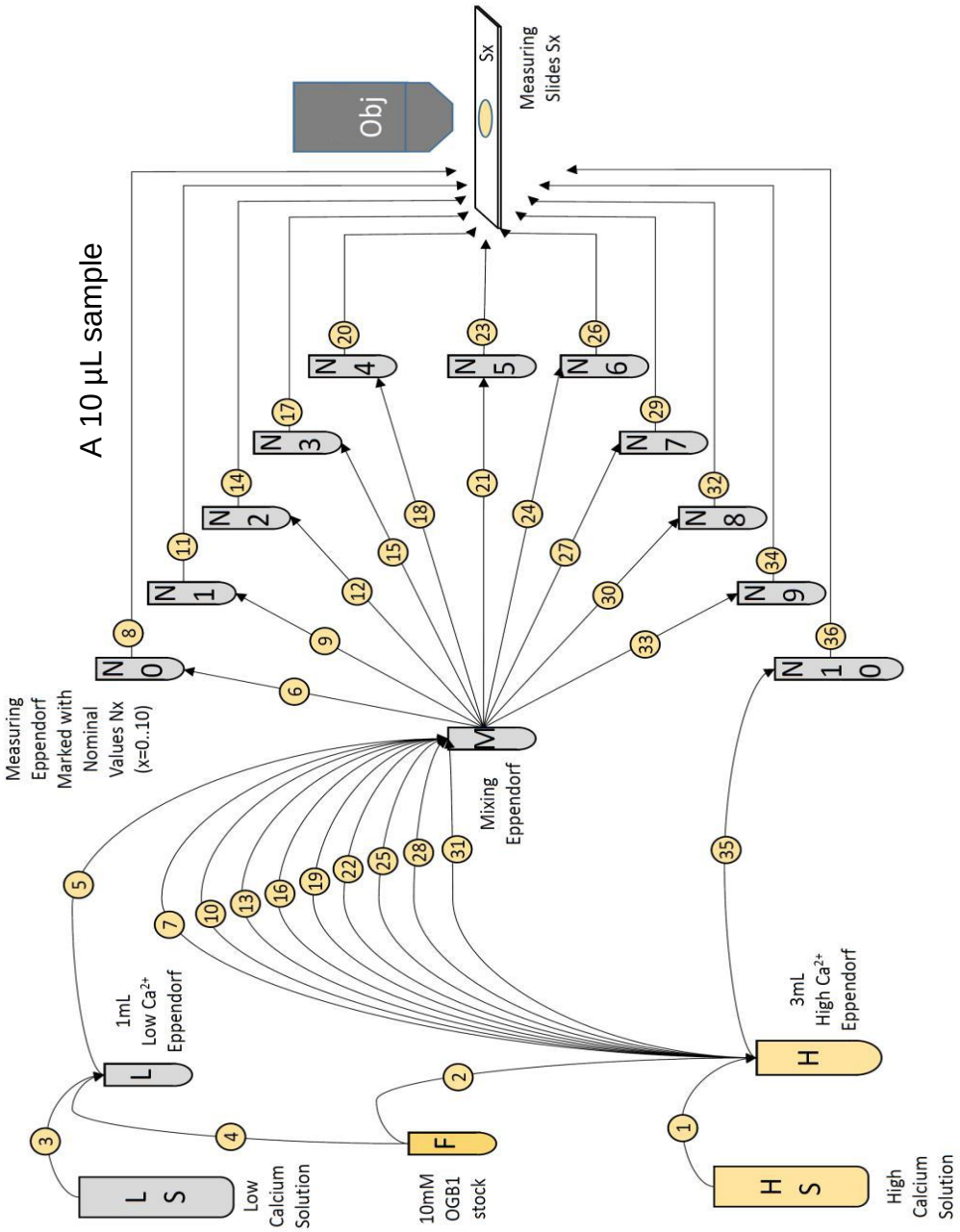

Figure 3.1 Preparation of calibration solutions with known [Ca^{2+}]

Solutions for the assessment of OGB-1 fluorescence lifetime with clamped [Ca^{2+}] were prepared on the day of calibration. Two solutions, one with high [Ca^{2+}] (HS) and one with low [Ca^{2+}] (LS), were prepared, along with a 10 mM OGB-1 stock solution (F). The mix of OGB-1 with HS and LS solutions were used to prepare a range of calibration solutions with different [Ca^{2+}], required steps are depicted with numerals in yellow circles.

Modified from Zheng et al., 2018

Eppendorf number	N0	N1	N2	N3	N4
Volume of solution to be replaced with HS, µL	100	111.1	125	142.9	166.7
Estimated [Ca^{2+}], nM	0	26	59	101	158

Eppendorf number	N5	N6	N7	N8	N9	N10
Volume of solution to be replaced with HS, µL	200	250	333.3	500	-	HS
Estimated [Ca^{2+}], nM	237	355	552	943	2000	2310

Table 3.2 Estimated [Ca^{2+}] in calibration solution

This table gives information about the steps shown in Figure 3.1. In particular, it details the volume of solution that needs to be replaced in the mixing eppendorf tube with high concentrated [Ca^{2+}] solution, the estimated [Ca^{2+}], and the corresponding eppendorf tube numbers. All the resulting mixed solutions of HS and LS were made up to a volume of 1 mL.

High and low [Ca^{2+}] solutions were prepared from the same chemical compounds used for internal solutions, in order to maximise the similarity with the experimental environment. A 10 µL sample of each solution was placed on a pre-warmed glass slide and covered with a coverslip, preventing any exposure to the air. Then a drop of water was placed on the top of each coverslip and OGB-1 lifetime was acquired for 60 ms. The temperature of the glass slide was maintained throughout the whole recording by keeping it on perfused water at 34–35°C. The lifetime of OGB-1 is plotted in Figure 3.2a, against estimated [Ca^{2+}]. In the elected range of OGB-1 concentrations from 0–2,310 nM, the normalised total photon count ratios show a near-linear relationship to [Ca^{2+}] (Figure 3.2b).

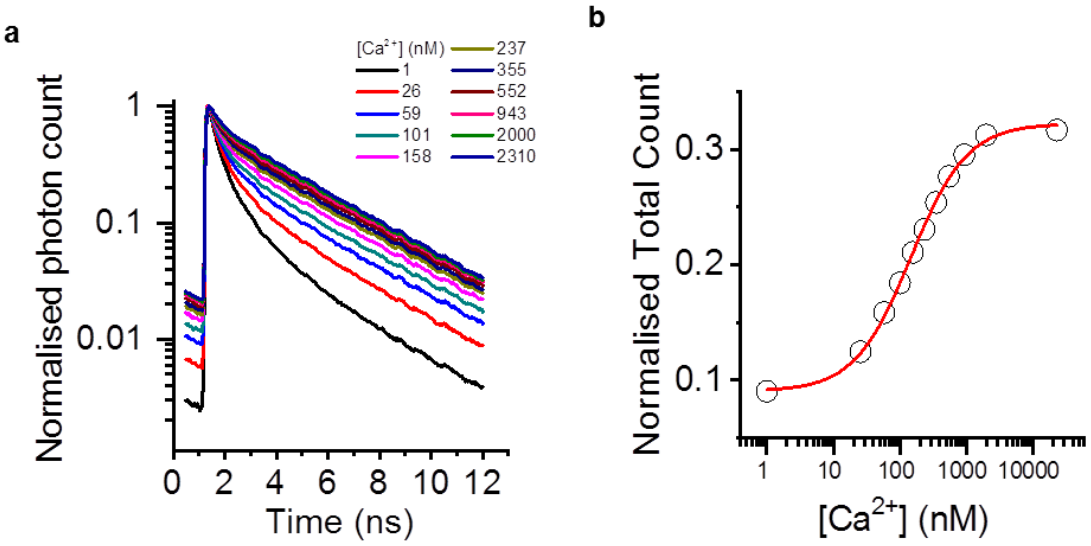

Figure 3.2 OGB-1 lifetimes for [Ca^{2+}] calibration solutions

These measurements were performed on a Femto-2D FLIM imaging system. A 10 µL sample from each of the solutions with a known [Ca^{2+}] concentration (solution compositions are given in Table 3.1; steps required for preparing solutions are depicted in Figure 3.1) were placed on a glass coverslip and maintained at 34–35ºC throughout calibration. OGB-1 excitation was performed at 800 nm wavelength. Acquisitions were performed in frame scan mode for 60 ms.

a- The fluorescence lifetime of OGB-1 normalised to the peak of OGB-1 fluorescence in solutions with known [Ca^{2+}]. FLIM measurements represent the photon count emitted by the dye bound to Ca^{2+} at the time shown in response to a single pulse. OGB-1 demonstrates longer lifetimes for higher [Ca^{2+}]

b- Summary calibration curve representing the normalised total count of photons fitted with logistic function. The linear relationship between OGB-1 lifetimes and [Ca^{2+}] are plotted on a logarithmic scale. Individual dots represent averaged lifetimes, recorded from a sample with known [Ca^{2+}] from 0–2,310 nM. The red line shows the best-fit curve for the obtained data points using a sigmoid function.

3.3.2. Astrocyte dye delivery options: AM ester loading and delivery through a patch pipette

Next, I tested two alternative approaches for dye delivery to the astrocytic syncytium: 1) bulk loading of the AM dyes; and 2) direct delivery to astrocytes through a patch pipette. Bulk loading provides labelling of multiple astrocytes, without mechanical interference or perturbation of the intracellular contents. However, this method can only stain astrocytic somata and results in poor labelling of thin astrocytic processes (Figure 3.3a). The second method is more invasive and requires a whole-cell patch-clamp of the astrocyte (Figure 3.2b). Such loading is more thorough and enables detection of subtle activity changes occurring in astrocytic processes. Moreover, the whole-cell configuration required for dye diffusion provides electrophysiological control of the membrane potential and of cell health during the experiment. Notably, whole-cell delivery of the dye to an astrocyte can be used to test gap-junction connectivity, which is an important physiological indicator of the healthy glial syncytium.

3.3.3. Comparing fluorescence intensity and FLIM measurements

Both labelling approaches enabled me to monitor Ca^{2+} dynamics in individual astrocytes (Figure 3.3c–d). Evaluating them, side-by-side allowed distinctive features of each to be established. I found that cell labelling with an AM dye was sufficient for monitoring spontaneous Ca^{2+} spikes, but only in cell somata (Figure 3.3c). However, this type of staining was not sufficient to resolve astrocytic activity in fine cell processes. On the contrary, direct delivery of the dye to the astrocyte greatly improved the signal-to-noise ratio and allowed the acquisition of basal [Ca^{2+}] fluctuations (Figure 3.3d). From

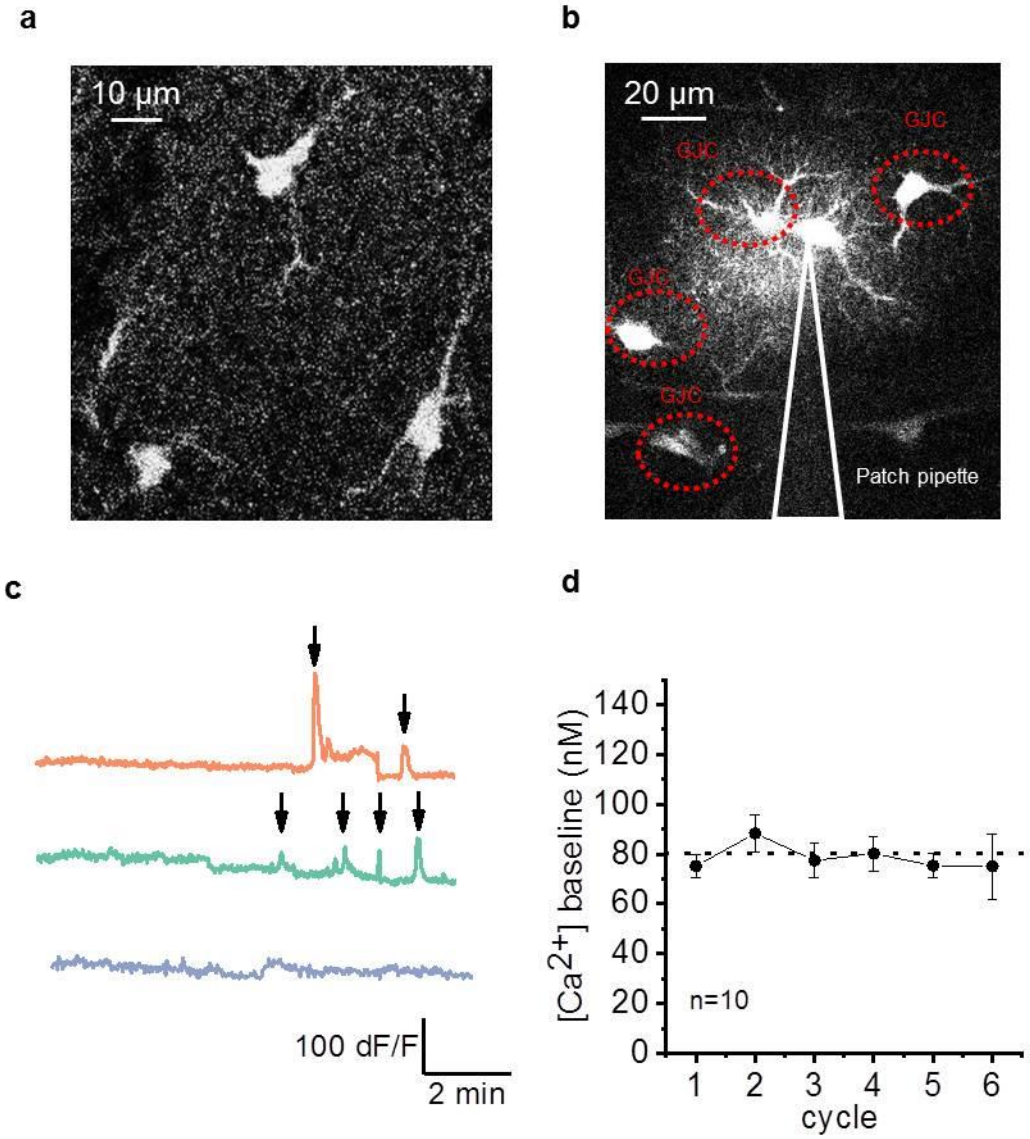

Figure 3.3 Fluorescence intensity and FLIM acquisition of [Ca^{2+}] dynamics in the astrocytic syncytium

a- Two-photon images of astrocytes in the CA1 *stratum radiatum* region showing bulk loading of a glial syncytium with OGB-1 AM and SR-101
b- Two-photon images of astrocytes in the CA1 *stratum radiatum* region (Alexa-594 channel). Delivery of OGB-1 and Alexa-594 dyes was performed through the patch pipette
c- Example traces of measured OGB-1 fluorescence intensity from the three astrocytes depicted in (a). Arrows indicate Ca^{2+} oscillations
d- The repetitive FLIM scanning cycles did not affect [Ca^{2+}] basal activity in astrocytic somata.

Data are presented as mean ± SEM.

the relatively stable FLIM readout of [Ca^{2+}] in between scanning cycles, the resting [Ca^{2+}] was estimated to be ~80 nM (Figure 3.3d).

3.3.4. Spiral FLIM-readout for the acquisition of [Ca^{2+}] in axonal boutons

The principal objective of this section was to develop and validate a protocol that would measure Ca^{2+} dynamics (via the fluorescence signal and FLIM readout) in individual axonal boutons during evoked activity in organised brain tissue. Acquiring Ca^{2+} dynamics from boutons involves registering relatively low baseline [Ca^{2+}], as well as rapid [Ca^{2+}] transients, which requires high sensitivity and excellent spatiotemporal resolution. The relatively small (1–2 µm) volume of presynaptic boutons correlates with the low photon count acquired per scan. Thus, several cycles are required for accurate estimation of [Ca^{2+}]. The typical pixel-by-pixel scanning approach does not follow the morphological architecture of a bouton, and more importantly, it would result in severe photodamage of the small structure.

To overcome these limitations, I used the spiral line-scan method, which, instead of using straight line sampling, employs circular pixel sampling, mimicking the physiological shape of boutons (Figure 3.4 and Figure 3.5a–b). A FLIM detector, equipped with analogue and photon-counting outputs represented another essential component for successful [Ca^{2+}] imaging of small structures. This setup allowed axonal boutons to be visualised using fluorescence intensity from the Alexa-594 channel and corrected any movements (Z-drift) in between cycles. To obtain a sufficient number of photons, several sets of line-scan acquisitions were needed. I tested the stability and phototoxicity of the protocol. As shown in Figure 3.5d [Ca^{2+}] remained stable across repeated cycles of FLIM acquisition, confirming that the protocol does not traumatise cells. Moreover, such an

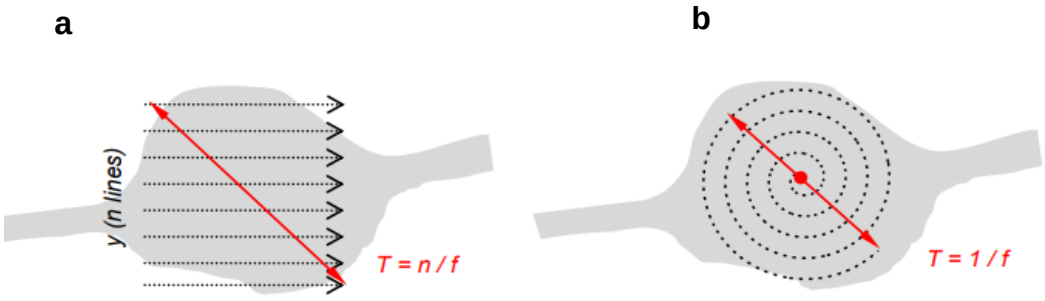

Figure 3.4 Schematic representation of the advantages of spiral scanning over frame scanning

a- A frame scan consisting of n lines with dwell-time T = n/f, where n is the number of lines required for scanning and f is the scanning frequency; schematic representation mimics presynaptic axonal bouton with 2 µm diameter

b- A spiral scan following the physiological morphology of a bouton of interest. The starting point of the scan is placed in the centre of the bouton. The time required for the acquisition of this pattern is T = 1/f, where f is the scanning frequency.

Adapted from Jensen et al., 2017.

approach has better temporal resolution compared to frame scans and allows a [Ca^{2+}] transient to be acquired in response to a single AP.

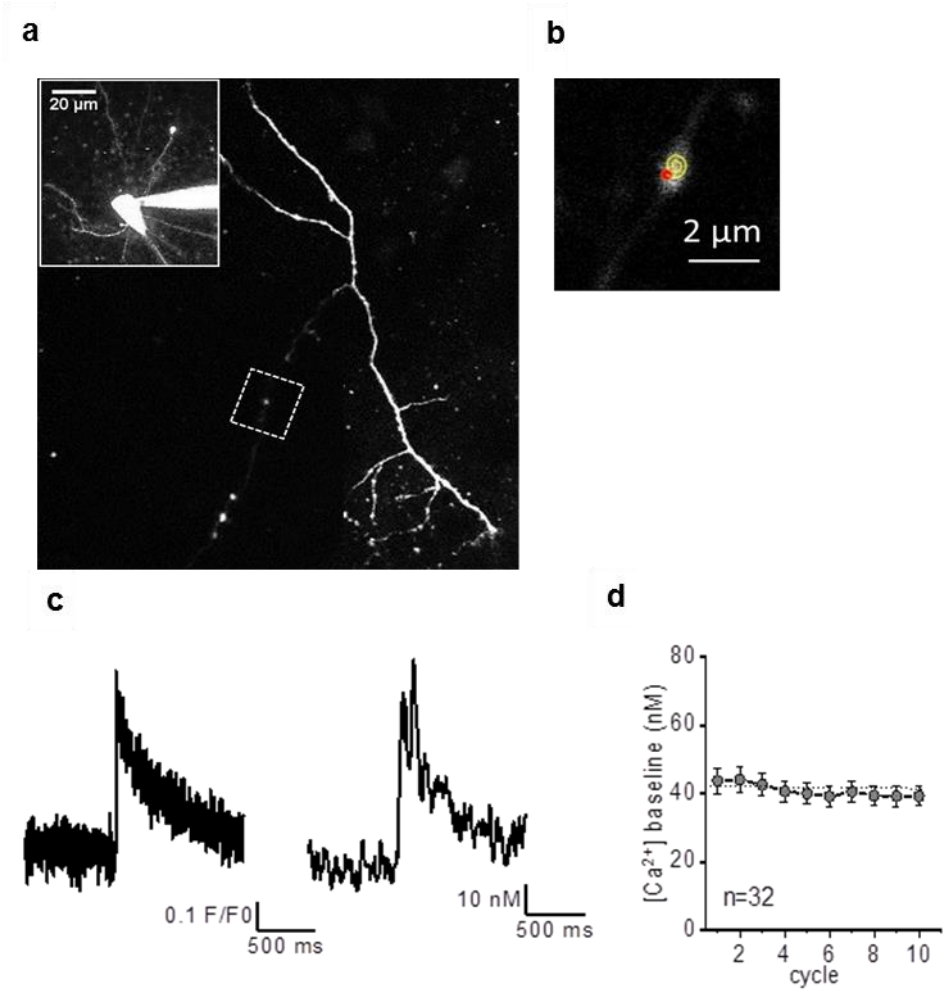

Figure 3.5 Spiral scanning enables simultaneous recording of changes in fluorescence intensity and FLIM signal in axonal boutons

a- A pyramidal neuron patched with Alexa-594. The axon was followed in frame scan mode; the bouton of interest is marked with the dotted rectangle
b- The region of interest shown in (a) by the dotted rectangle at high magnification, containing a presynaptic bouton. Scanning was performed as shown, using a spiral-shaped line centred on the bouton centroid
c- Signals measured from the depicted bouton: OGB-1 fluorescence intensity and spiral-FLIM readout of presynaptic axonal [Ca^{2+}] in response to a single AP delivered through the patch pipette
d- The summary plot representing fluctuations in basal [Ca^{2+}] in between FLIM acquisitions.

Data are presented as mean ± SEM.

3.4. Discussion

3.4.1. OGB-1 calibration for Ca^{2+} readout

3.4.2. Optimal dye delivery options to astrocytic syncytia

Several approaches are available today for labelling astrocytes, including direct dye delivery through the patch pipette, bulk loading of dye in the AM form, or the expression of genetically-encoded Ca^{2+} indicators (GECIs). AM loading allows dozens of cells to be labelled at the same time without producing a lot of mechanical damage. Although this method of dye delivery potentially allows Ca^{2+} dynamics to be measured under more physiological conditions, it is challenging to maintain the electrophysiological properties of cells throughout the experiment. The AM form of the dye is non-specific to cell types, hence preventing the separation of astrocytes from neurons, especially on the level of cell processes. Most of the time, a particular issue can be solved by introducing a second astrocyte-specific dye, for instance, SR-101. Overlapping of Ca^{2+} dye and SR-101 signals occurs only in astrocytes. However, this dye delivery method only allows activity to be measured in relative large astrocytic branches. Alternatively, the patch-clamp technique not only allows direct delivery of the indicator to the cell of interest, but also provides essential monitoring of electrophysiological parameters throughout the experiment. As described in chapter 1, neighbouring astrocytes are connected through gap-junctions that are permeable to quite large substances, so loaded dye would also diffuse through gap-junctions, confirming the physiological integrity of the astrocytic syncytium. Uncoupling of such connections are believed to be triggered by an increase in $[Ca^{2+}]$ (Peracchia, 1978, 2004) and dramatic pH changes can be used as an additional parameter for monitoring astrocytic health. Among the limitations of this method, however, are the introduction of mechanical disruption, as well as washout of the internal constituents of the cell (Kato et al., 1993).

The improved fast kinetics of GECIs allow short Ca^{2+} events to be measured on the level of minuscule astrocyte processes, as well as whole

syncytia (Ye et al., 2017). Unfortunately, the fluorescence lifetime of GECIs does not change upon Ca^{2+} binding, making FLIM acquisitions impossible. Another severe limitation of this technique is the difficulty of obtaining stable and adequate expression levels of GECIs inside cells. Furthermore, their over-expression might lead to an imbalance of Ca^{2+} buffering in the system.

3.4.3. Acquisition of Ca^{2+} signals from small structures in organised brain tissue

In this chapter, I have established and validated protocols for acquiring fluorescence intensity based-measurements and FLIM in small structures of organised brain tissue. Directly measuring [Ca^{2+}] dynamics in minuscule structures in slices is a challenging task, mostly due to light scattering and the low signal-to-noise ratio (especially under baseline conditions). Even though FLIM techniques can resolve those drawbacks, they usually require pixel-by-pixel scanning, which correlates with exposure of the region of interest to the laser and limited temporal resolution; hence, in our laboratory, an advanced approach for FLIM data analysis was developed. This method uses integrated OGB-1 fluorescence decay kinetics over 9 ns, rather than a bi-exponential approximation. Additionally, it introduces a smaller error compared to the classical technique. An improved signal-to-noise ratio could be achieved with fewer photons, meaning a reduced laser exposure time. Secondly, measuring [Ca^{2+}] dynamics in small structures is limited by the much lower number of available fluorophore molecules. This obstacle could be partially solved by extending the scanning time, which would result in slower readout and also be more traumatic to the cell. Application of spiral-shaped line-scans (rather than frame- or line-scans) enabled me to obtain [Ca^{2+}] readouts in astrocytic somata and axonal boutons in organised brain tissue. The combination of these approaches with recently developed genetically encoded sensors (e.g. iGluSnFR) and Ca^{2+} red-shifted dyes (e.g. Cal-590) would allow simultaneous

measurement of presynaptic Ca^{2+} activity and quantum release of neurotransmitters in brain tissue.

3.5. Conclusion

In this chapter, I calibrated the Ca^{2+}-sensitive dye OGB-1 for Ca^{2+} readout in solutions with known [Ca^{2+}], mimicking similar extracellular environments to those used in the experiments. Testing alternative methods of dye delivery to the astrocytic syncytium, as well as probing two acquisition paradigms, allowed the appropriateness of this methodological approach to the thesis objectives to be evaluated. For measuring evoked or spontaneous Ca^{2+} transients in astrocytes, the preferred method would be bulk loading of the dyes with fluorescence intensity measurements. For acquiring nanomolar [Ca^{2+}] changes, it would be more optimal to use direct dye delivery to the cell through the patch-pipette (due to a better signal-to-noise ratio) and FLIM imaging.

Chapter 4

Monitoring intracellular [Ca^{2+}] dynamics in astrocytes via combined fluorescent intensity and fluorescence lifetime measurements

In this chapter, I validate approach for measuring fluorescence intensity along with FLIM acquisition from astrocytes and neurons during application of exogenous substances. In order to select these substances, I applied the following criteria. First and foremost, each of the exogenous substances should be well established as a potent agent, triggering Ca^{2+} elevation in neural cells (namely astrocytes and neurons), in either cultures or organotypic slices. This property is essential for allowing fluorescent intensity and lifetime measurements to be compared to established experimental results. The next important property is that the exogenous substance should preserve the natural extracellular environment, including gap-junction connections between neighbouring astrocytes that are present in the organised brain tissue used. Here, it should be taken into account that bulk application, a commonly-used approach to applying exogenous substances to cultures, has a severe limitation in terms of diffusion within the brain tissue that requires alternative methods for controlled drug delivery to the thick acute slice. Based on the objectives of this chapter, I selected two substances: 1) dopamine, a potent endogenous neurotransmitter in the brain; and 2) beta-amyloid (Aβ) peptide, a pathological trigger of robust and long-lasting intracellular Ca^{2+} rise and Ca^{2+}-induced neuronal cell death. Later in this chapter, I describe recent findings, which demonstrate the effects of Aβ peptide and dopamine on Ca^{2+} signalling in astrocytes.

4.1. Introduction

Dopaminergic transmission contributes to locomotor control and reward-motivated behaviour (Wise, 2004), while abnormal dopamine regulation can lead to severe psychotropic pathologies, such as schizophrenia, drug addiction, or Parkinson's disease (for reviews, see Vaughan and Foster, 2013; Leyton and Vezina, 2014; Nutt et al., 2015). The primary sources of dopamine in the brain are two regions within the basal ganglia: the substantia nigra and the ventral tegmental area (Björklund and Dunnett, 2007). The hippocampus receives dopaminergic projections from both of these areas. It has been shown that these projections to the hippocampus have an impact on spatial memory formation (da Silva et al., 2012). The signalling pathway for dopamine action on different cell types includes activation of D1 and D2 receptor groups, which are both linked to a variety of intracellular signalling cascades (Missale et al., 1998). Activation of D1 receptors (D1/D5 receptor subtypes) stimulates cyclic adenosine monophosphate (cAMP) formation and activation of protein kinase A (PKA), which is capable of phosphorylating numerous target proteins. One such protein, DARPP-32, underlies further downstream effects on a handful of effector proteins. It has been shown that DARPP-32 activation leads to enhancements of AMPA receptor- (Roche et al., 1996) and L-type Ca^{2+} channel-mediated conductance (Surmeier et al., 1995), whereas it leads to inhibition of voltage-dependent Na^{+} channels (Cantrell et al., 1997), N/P-type Ca^{2+} channels (Surmeier et al., 1995) and γ-aminobutyric acid type A receptors ($GABA_A$) (Flores-Hernandez et al., 2000). In contrast, activation of D2 receptors (D2, D3, and D4 receptor subtypes) inhibits adenylyl cyclase (AC) and suppresses PKA activation, leading to an intracellular [Ca^{2+}] rise.

A series of studies has been performed to establish how dopamine affects neuronal pathways and astrocytic functioning in cultures. Activation of D1 receptors in cultured astrocytes stimulates cAMP production and PKA activation (Zanassi et al., 1999) and evoked elevation of Ca^{2+} (Parpura and Haydon, 2000; Requardt et al., 2012). Also, D2 receptors activation was shown

to induce Ca^{2+} signalling in cultured astrocytes (Khan et al., 2001; Reuss and Unsicker, 2001). In the first section of this chapter, I probe the effects of dopamine on changes in [Ca^{2+}] in astroglia in organised brain tissue.

Accumulation of Aβ peptide is implicated in Alzheimer's disease (AD) as one of the principal components of amyloid plaques. The pathological brain tissue phenotype of AD patients is associated with Aβ plaque accumulation, which typically extends from the entorhinal cortex to the hippocampus and neocortex. At the network level, it has been demonstrated that Aβ oligomers, extracted from the cerebrospinal fluid of Alzheimer's patients, inhibit LTP (Walsh et al., 2002). Aβ oligomers were shown to affect neurons directly by binding to a wide range of receptors, including lipid, proteoglycan and protein receptors. Detailed studies have shown that the soluble oligomeric Aβ which is proposed to underlie the neurotoxic effect binds to the p75 neurotrophin receptor (Yaar et al., 1997), the low-density lipoprotein receptor-related protein (Zlokovic et al., 2010), the β-adrenergic receptor (Wang et al., 2010), the nicotinic acetylcholine receptor, and NMDA receptors (De Felice et al., 2007; Costa et al., 2012). In astrocytes, Aβ peptides operate via metabotropic glutamate receptors, namely mGluR5 (Casley et al., 2009; Lim et al., 2013), or the cellular prion protein, PrPc (Laurén et al., 2009). Conformational changes of PrPc were shown to underlie encephalopathies and cause neurological disorders, while Aβ interaction with mGluR5 has been shown to trigger Ca^{2+} release from intracellular stores. Although it is currently well established that accumulation of Aβ and neurofibrillary tangles in AD lead to gradual synaptic degeneration and subsequent neuronal cell loss (Vargas-Caballero and Robinson, 2003), the underlying cellular mechanisms are still poorly understood. Following the onset of AD, both neurons and glial cells have been found to be severely dysfunctional, making it unclear which cell type undergoes damage first. Previously, it has been shown that application of oligomers rather than monomers elevates intracellular Ca^{2+} in human neuroblastoma cells (Demuro et al., 2005). Interestingly, when applied to neuron–astrocyte co-cultures, Aβ oligomers do not affect intracellular Ca^{2+}

signalling in neurons, but trigger a prominent elevation of Ca^{2+} in astrocytes, potentially via Aβ-induced formation of membrane channels (Abramov et al., 2003). Majority of studies investigating Aβ effect on Ca^{2+} elevation in astrocytes have been performed in cultured, isolated cells or organotipic slices. Taking into account major difference between astrocytes in culture and *in situ,* the Ca^{2+} signalling in astrocytes exposed to Aβ in organised brain tissue yet to be investigated. Furthermore, I take advantage of the FLIM technique to evaluate, astrocytic [Ca^{2+}] dynamics following Aβ oligomer application in organised brain slices.

4.2. Methods

Monitoring Ca^{2+} activity in astrocytes and neurons was performed using hippocampal slices from P21–25 male Sprague Dawley rats. Acute slices were either incubated with the cell-permeable Ca^{2+}-sensitive dye OGB-1 AM along with the astrocytic marker SR-101 or loaded with OGB-1 and Alexa-594 through the patch pipette. At least 45 min was allowed for dye diffusion and equilibration in the whole-cell configuration.

A Biosep SEC-s2000 size exclusion column was employed to purify Aβ1–42 peptides. Peptide samples were frozen and stored at −80^{0}C. On the day of the experiment, purified Aβ was diluted to 500 nM in phosphate-buffered saline (PBS) and left shaking at 37°C at 200 rpm for 5 h. Next, the sample was centrifuged at 14,500 g for 10 min and diluted to the final concentration in L15 medium. During experiments to restrict Aβ oligomer interaction to cells located closer to the surface of the slice, I applied Aβ locally to the cell of interest through a pressurised micro-pipette. Oligomer diffusion was monitored by the spread of Alexa-594 dye, which was also added to the pipette. Dopamine (100 µM) was added to the perfusion solution, with a further washout period. After establishing a 10–15 min baseline, either Aβ or dopamine was applied to the brain tissue for 10 min, with a subsequent washout period. Changes in [Ca^{2+}] dynamics were acquired with Femto 2-D system in two-photon frame imaging

scanning mode over cell somata. Images were recorded in laser line-scan mode, set to 500 lines per second and stored in 256 × 512 × 512 × n (t × x × y × T) format. This format represents x-y images with a nanosecond delay time distribution (t) of photons at each pixel for the duration of the scan (T). Each of the frame scans took 120–300 s to record (depending on the signal brightness); these were averaged over time separately.

4.3. Results

4.3.1. Dopamine application induces bidirectional [Ca^{2+}] responses in astrocytes in brain tissue

Pioneering studies performed in cell cultures have shown that dopamine application increases magnitude and frequency of Ca^{2+} dynamics in astrocytes. Firstly, I tested how astrocytic [Ca^{2+}] in organised brain tissue is affected by dopamine application. Hippocampal astrocytes showed a prominent [Ca^{2+}] increase in response to application of dopamine to the bath perfusion system, from 100.28 ± 5.47 nM to 123.12 ± 11.28 nM ($n = 15$; $p < 0.05$, one-sample t-test; Figure 4.1a–b). The dopamine-induced [Ca^{2+}] transient was followed by a below-baseline [Ca^{2+}] decrease to 85.84 ± 5.64 nM ($p < 0.05$, one-sample t-test; Figure 4.1a–b) during the dopamine washout period. It should be noted that dopamine administration triggers Ca^{2+} responses at both gap-junctions and in patched astrocytes. However, due to the proximity of the dialyzing pipette, the [Ca^{2+}] baseline level in patched cells was already high (155.75 ± 7.09 nM; Figure 4.1c). Hence, the cell soma and processes of the patched astrocyte showed little capacity to change [Ca^{2+}]

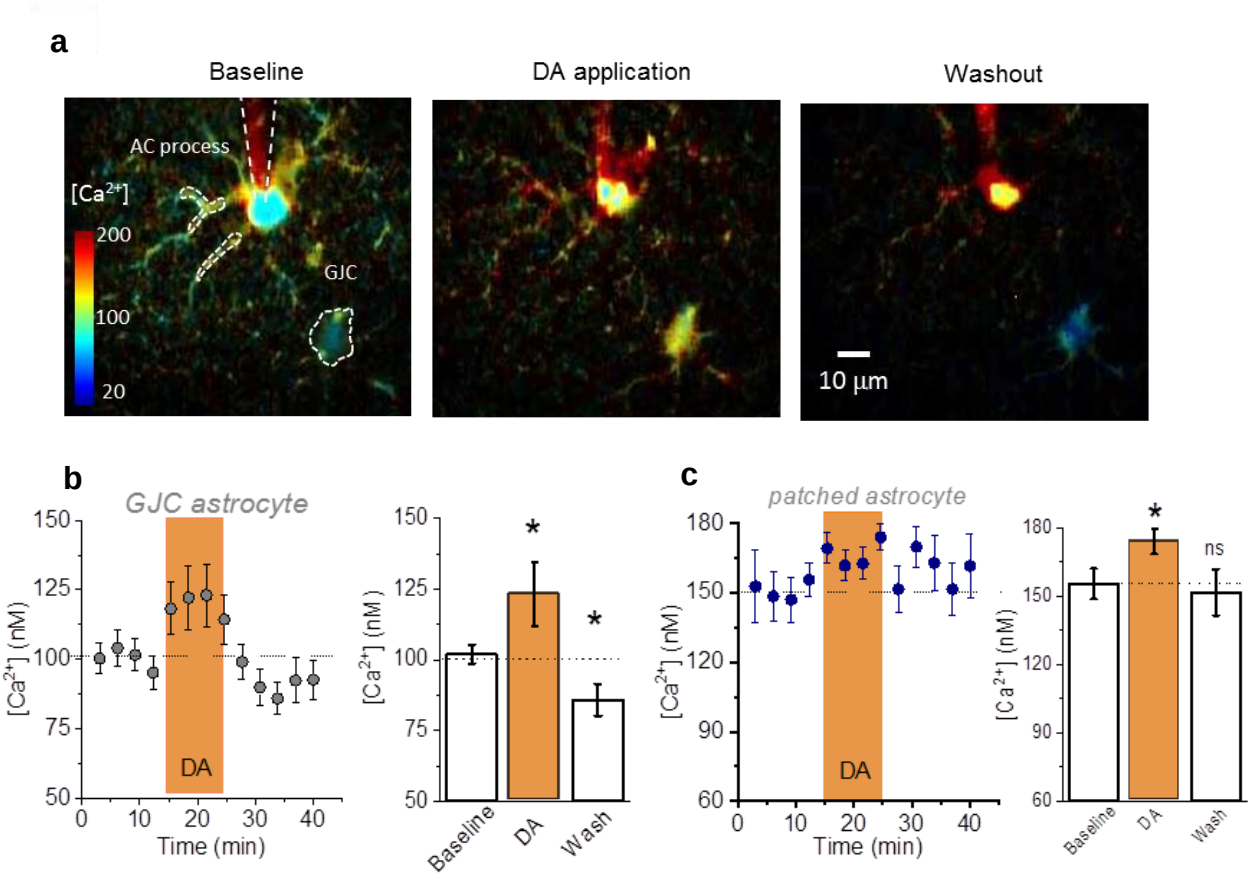

Figure 4.1 Dopamine application induces bidirectional [Ca^{2+}] response in astrocytes

a- Monitoring of basal [Ca^{2+}] in hippocampal astrocytes during baseline, dopamine application, and washout periods. Direct delivery of the dyes was performed through the patch pipette, as depicted on the first image. The gap-junction astrocyte is marked with a dotted line. Internal [Ca^{2+}] levels are colour-coded according to the false colour scale bar

b- The average time course of intracellular [Ca^{2+}] fluctuations during dopamine application to gap-junction astrocytes (100 µM, orange bar). Each scanning frame was acquired for 120–300 s. The bar graph shows a statistical summary. The dashed line indicates the significance level relative to baseline

c- The average time course of intracellular [Ca^{2+}] fluctuations during the application of dopamine to patched astrocytes (100 µM, orange bar).

Dopamine application – DA; gap-junction connected astrocyte – GJC astrocyte.

Data are presented as mean ± SEM; *p < 0.05.

upon dopamine application (174.04 ± 5.69 nM; n = 8; $p < 0.05$, one-sample t-test; Figure 4.1c), most likely because of the perturbing influence of cell dialysis.

The findings from these experiments indeed confirm that dopamine application to the organised brain tissue induces an elevation in the basal level of [Ca^{2+}] in astrocytes. Importantly, the advanced FLIM approach used allowed me to identify a novel dopamine-induced decrease of [Ca^{2+}] to below baseline.

4.3.2. D1/5 receptor blockage eliminates the dopamine-induced increase in [Ca^{2+}]

To identify the particular dopamine receptor subtype responsible for the dopamine-induced effect on astrocytic [Ca^{2+}], I blocked type-1 dopamine receptors by introducing SCH23390 to the perfusion solution. This antagonist blocks D1/5 receptors, leaving D2/3 receptors subtypes unaffected. Under these conditions, dopamine application does not produce any detectable [Ca^{2+}] elevation in astrocytes, although SCH23390 treatment alone was accompanied by a decrease of basal [Ca^{2+}] in astrocytes from 103.08 ± 2.79 nM to 95.15 ± 2.70 nM and 81.16 ± 5.00 nM during washout period (n = 11; $p < 0.05$ and $p < 0.001$, respectively, one-sample t-test; Figure 4.2a). This suggests that D2/3 receptor activation can reduce Ca^{2+} mobilisation.

4.3.3. Dopamine-mediated [Ca^{2+}] elevation in astrocytes is independent of neuronal firing activity, and of metabotropic glutamate or GABA receptors

Bulk application of dopamine to organised brain tissue affects dopaminergic neurons, which in turn might indirectly modulate Ca^{2+} dynamics by targeting astrocytic receptors. To eliminate the effect of dopamine on

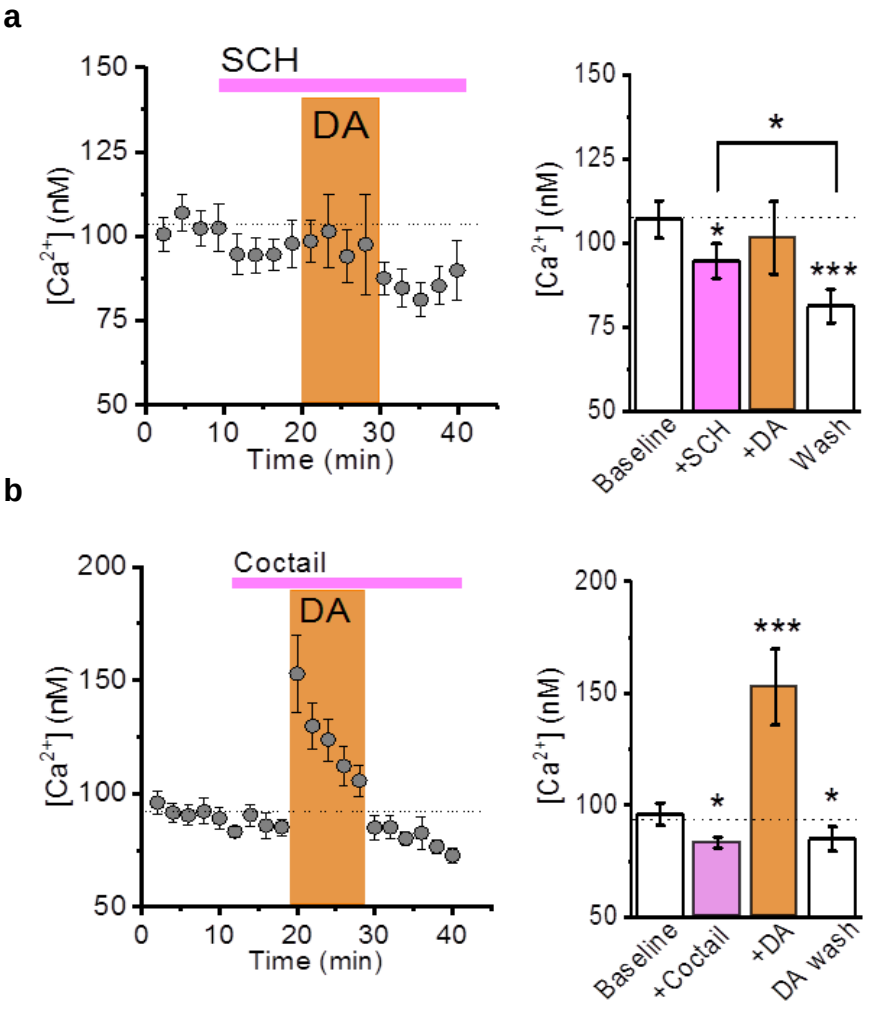

Figure 4.2 Dopamine induces an increase in [Ca^{2+}] via astrocytic D1/5 receptors but not through neuronal signalling

a- Time course of intracellular [Ca^{2+}] changes in astrocytes upon application of the D1/5 receptor antagonist SCH23390 (20 µM, pink) and dopamine (100 µM, orange), as indicated; the bar graph represents a statistical summary of the experiments depicted in the plot to the left

b- Time course of intracellular [Ca^{2+}] changes in astrocytes upon application of a cocktail of blockers and dopamine (100 µM, orange); the bar graph represents a statistical summary of the experiments depicted in the plot to the left.

Dopamine application – DA; SCH23390 application – SCH

Data are presented as mean ± SEM; *p < 0.05, ***p < 0.001, significance level relative to baseline [Ca^{2+}] (dashed line).

neurons a cocktail of ionotropic and metabotropic receptor blockers was applied, comprising: the Na^+-channel blocker TTX (1 µM); the mGluR5 blocker MPEP (1 µM); the mGluR5 blocker LY367385 (100 µM); the mGluR2/3 blocker LY341495 (500 nM); and the $GABA_B$ receptor blocker CGP (1µM). The suppression of neuronal activity did not affect dopamine-mediated [Ca^{2+}] transients, and the [Ca^{2+}] increased from a baseline level of 96.01 ± 4.92 nM to 152.89 ± 17.00 nM ($n = 17$; $p < 0.001$, one-sample t-test; Figure 4.2b). The data from this recording was not significantly different from the data obtained in the control condition. Dopamine washout was linked with a small [Ca^{2+}] decrease from 96.01 ± 4.92 nM to 84.98 ± 5.47 nM ($n = 17$; $p < 0.05$, one-sample t-test; Figure 4.2b), consistent with some contribution of neuronal activity to basal astrocytic [Ca^{2+}].

4.3.4. Aβ application induces a Ca^{2+} increase in astrocytes in organised brain tissue of acute slices

In the experiments in this section, I first tested whether astrocytes in organised brain tissue respond to Aβ application with an increase in Ca^{2+} level. Indeed, astrocytes loaded with OGB-1 AM dye showed an increase of fluorescent intensity upon exposure to Aβ. Application of Aβ through a pipette enables localised effects on a single astrocyte to be detected and compared with Ca^{2+} levels in neighbouring gap-junction astrocytes. For application, the pipette was filled with Aβ oligomers (500 nM; Figure 4.3a–b). Localised delivery of Aβ to the cell of interest evoked a Ca^{2+} transient, which had terminated by the end of the pressurised application of Aβ. Exposure to Aβ did not trigger an increase in the frequency of Ca^{2+} oscillations, but rather caused a slow increase in baseline Ca^{2+}. Monitoring of Ca^{2+} activity from gap-junction connected cells did not show any changes (Figure 4.3c), suggesting that the extracellular environment represents a physical barrier, restricting Aβ diffusion to neighbouring astrocytes.

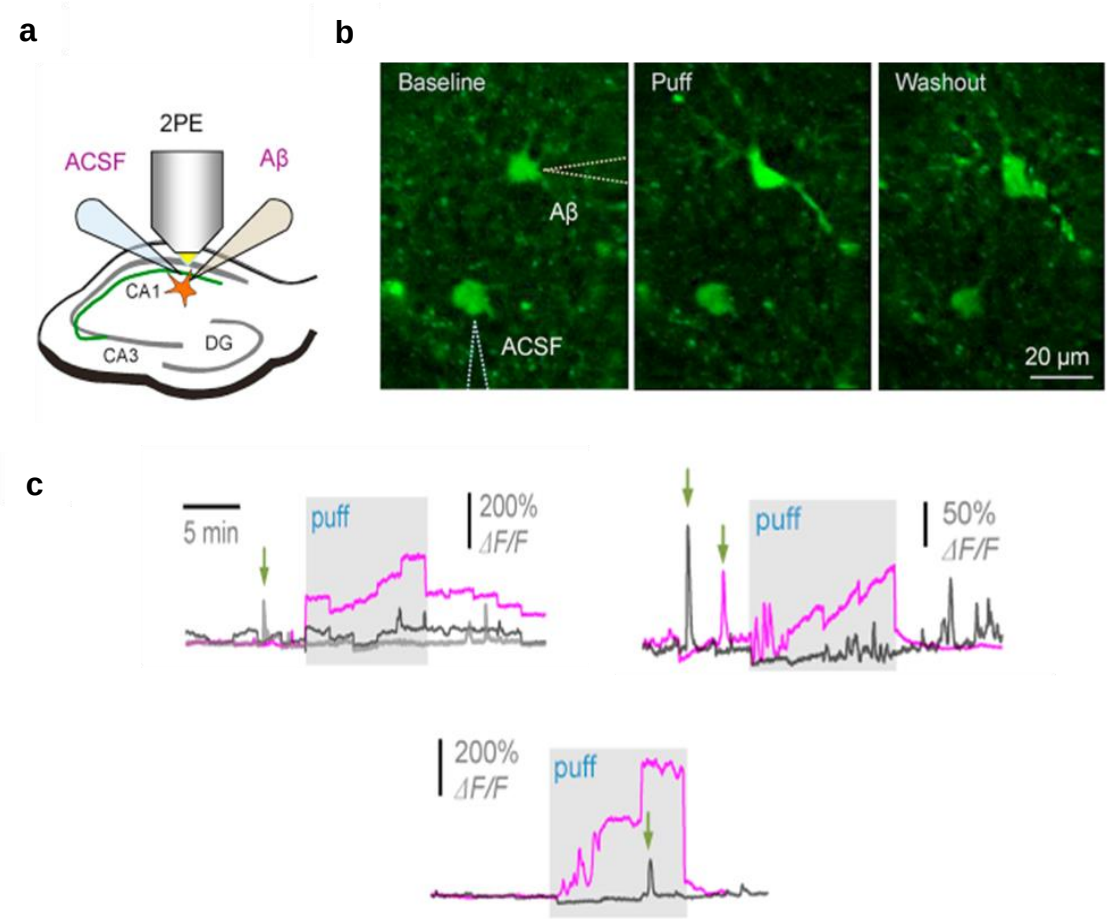

Figure 4.3 Aβ oligomer application increases Ca^{2+}-dependent fluorescence in astrocytes

a- Scheme of imaging experiments with localised substance delivery via two pressurised micropipettes

b- An example of individual astrocytes during the baseline, 10 min Aβ oligomer application, and washout periods, as labelled. Pipette positions are depicted with dotted lines

c- Three examples depicting an increase in Ca^{2+} fluorescence upon application of Aβ oligomers. Pressurised ACSF solution application in the same experiments did not produce any effect on astrocytic Ca^{2+} (black traces). The no-puff example is depicted on the left plot (grey trace). Arrows indicate examples of spontaneous Ca^{2+} elevations in astrocytes. The staggered shape of the trace reflects the periodic focal corrections which occurred during long recording sessions.

4.3.5. Aβ-mediated Ca^{2+} elevation does not depend on its pressurised application

Whilst pressurised application provides targeted Aβ delivery restricted to the cell of interest in the tissue, the method has limitations. It has been previously established that the air pressure required for local delivery might affect the surrounding tissue by producing mechanical artefacts and trigger Ca^{2+} transients in astrocytes (Newman, 2001; Angulo et al., 2004). To remove this mechanical artefact, I placed a patch pipette filled with Aβ-free ACSF solution and applied the same amount of pressure to neighbouring gap-junction astrocytes. Local ACSF solution application did not produce any change in Ca^{2+} dynamics (Figure 4.3c, black traces); suggesting that pressurised delivery of compounds in the conditions described does not increase Ca^{2+} levels or spontaneous activity.

4.3.6. Aβ-mediated $[Ca^{2+}]$ increase in targeted astrocytes

Next in our plans was the estimation of $[Ca^{2+}]$ elevation upon Aβ application. Astrocytes were patched with the dye OGB-1, which is highly sensitive to free nanomolar levels of Ca^{2+}. After diffusion to neighbouring astrocytes, $[Ca^{2+}]$ signals were recorded from gap-junction connected cells (Figure 4.4a–b). Localised Aβ delivery for 10 min elevated basal astrocytic $[Ca^{2+}]$ from 73.83 ± 3.51 nM to 140.12 ± 35.33 nM ($n = 4$; $p < 0.05$, paired-sample t-test; Figure 4.4c). Again, this $[Ca^{2+}]$ elevation had terminated by the end of oligomer application and returned to baseline. Meanwhile, neighbouring gap-junction astrocytes, located 50–100 µm from the application site, showed no change in $[Ca^{2+}]$ (75.15 ± 4.47 nM to 72.54 ± 7.78 nM; $n =10$; $p > 0.05$; Figure 4.5a). These findings are consistent with previous fluorescent intensity-based experiments, indicating that astrocytes are capable of increasing $[Ca^{2+}]$ in response to local Aβ application and that $[Ca^{2+}]$ in neighbouring gap-junction astrocytes remains unaffected. This may be due to the relatively large size of

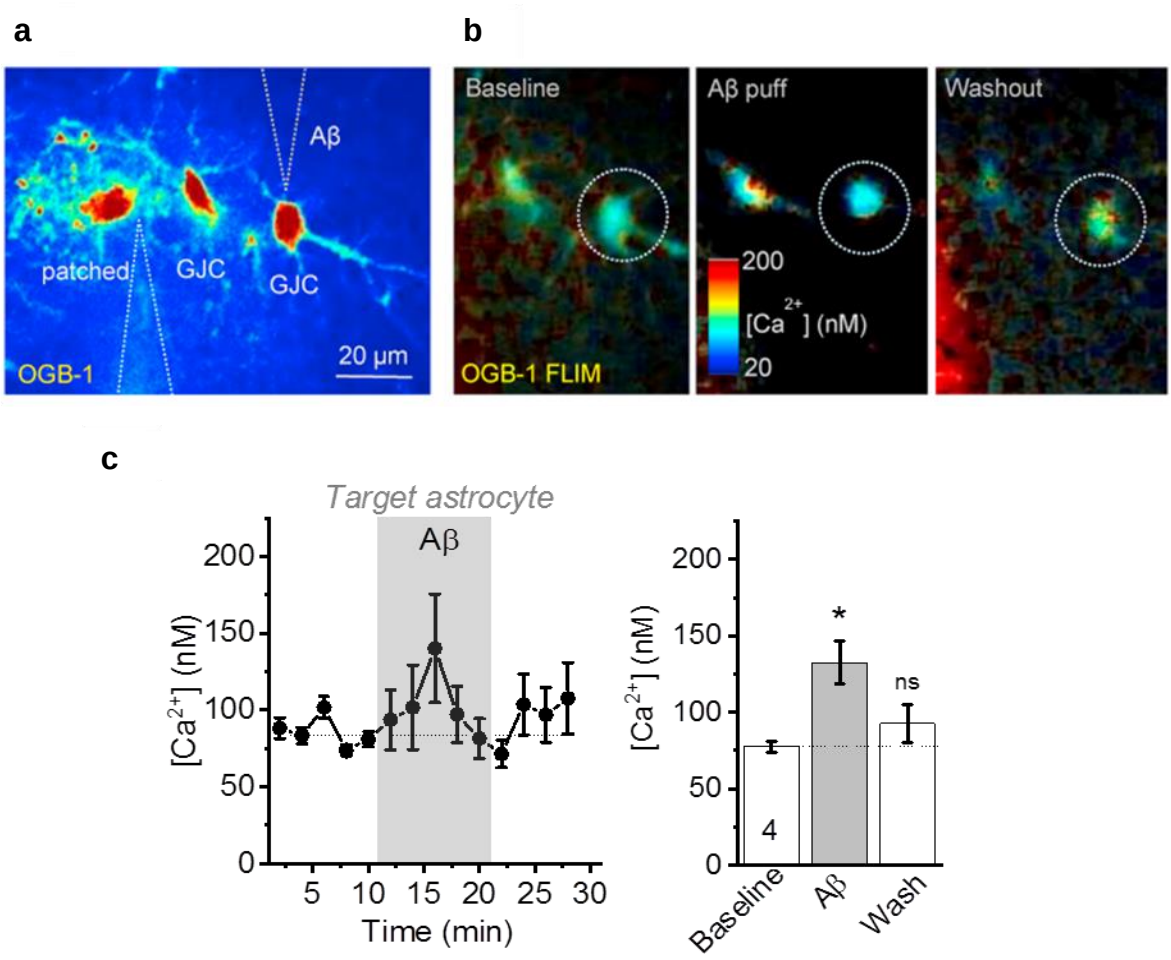

Figure 4.4 Aβ oligomer application induces reversible increases in [Ca^{2+}] in targeted astrocytes

a- An example of the experimental setup, showing a patched astrocyte with gap-junction cells. Localised Aβ application was performed through the pipette, as shown in the upper right corner. The false-colour intensity image acquired in the OGB-1 channel

b- Monitoring astrocytic [Ca^{2+}]: OGB-1 FLIM-based [Ca^{2+}] maps recorded for the baseline, Aβ oligomer application and washout periods. The target astrocyte is indicated by the circle

c- Statistical summary of experimental data for targeted astrocytes. Because the [Ca^{2+}] peak was reached at a different time in each cell, the comparison was made in individual cells based on the [Ca^{2+}] peak over baseline; the bar graph represents a statistical summary of the experiments depicted in the plot to the left.

Data are presented as mean ± SEM; ns: $p > 0.05$; *$p < 0.05$.

the oligomers and their restricted movement in organised tissue. Changes in astrocytic basal [Ca^{2+}] do not readily propagate to adjacent cells via gap junctions.

4.3.7. Aβ application does not affect [Ca^{2+}] levels in CA1 pyramidal neurons

Cultured neurons had been shown to respond to Aβ application with Ca^{2+} increases; here, I tested how a localised application of Aβ affects neuronal [Ca^{2+}] dynamics in organised brain tissue. Oligomers were delivered through the pressurised pipette to the somata of CA1 pyramidal neurons. The pipette was placed at the same distance from the targeted cell as in the astrocyte-targeting experiments. Because of low photon counts in thin neuronal dendrites, the [Ca^{2+}] signal was acquired from the somatic region. Application of Aβ oligomers induced a small basal [Ca^{2+}] transient in neuronal somata from 97.00 ± 16.75 nM to 109.71 ± 14.58 nM ($n = 3$; $p > 0.05$, paired-sample t-test; Figure 4.5b), suggesting that Aβ application primarily affects astrocytic, rather than neuronal, [Ca^{2+}] dynamics.

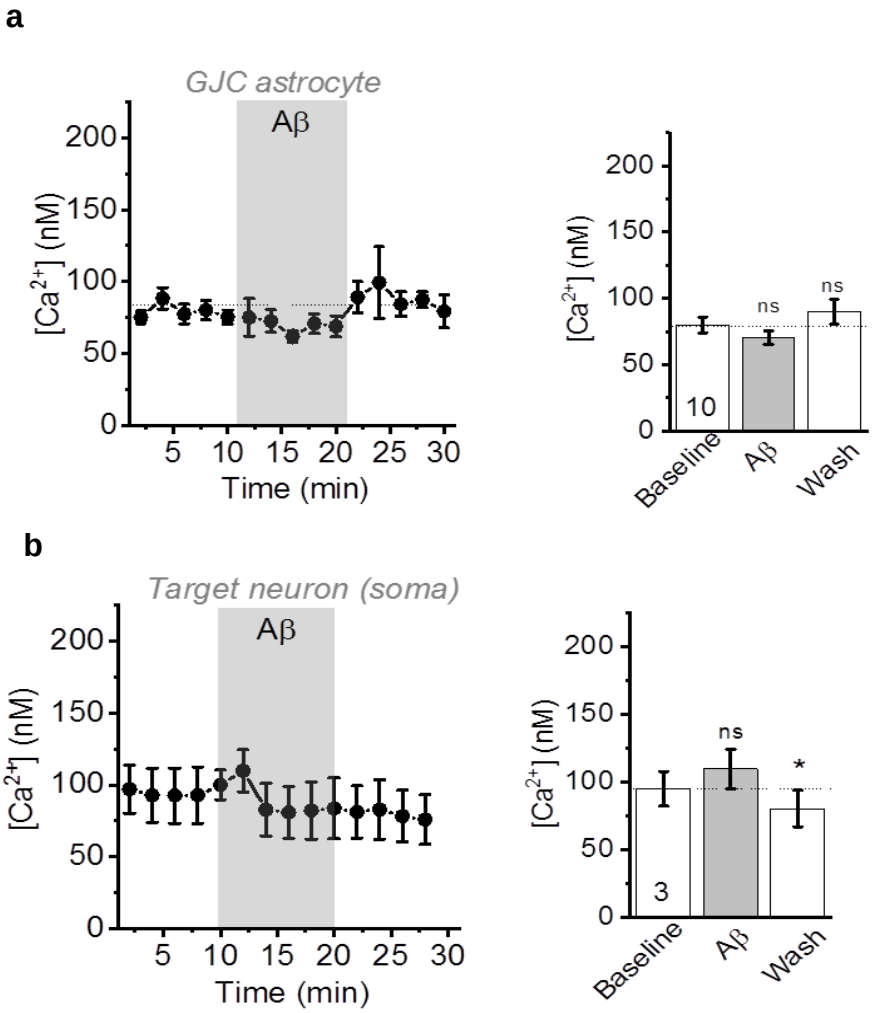

Figure 4.5 Aβ oligomers do not affect [Ca^{2+}] dynamics in neighbouring astrocytes and cause a small increase in [Ca^{2+}] activity in CA1 pyramidal neurons

a- Statistical summary of experiments, showing that Aβ oligomer application to targeted astrocytes does not affect [Ca^{2+}] signalling in neighbouring gap-junction cells; the bar graph represents a statistical summary of the experiments depicted in the plot to the left

b- Statistical summary of experiments, showing that Aβ oligomer application to CA1 pyramidal neurons does not affect [Ca^{2+}] signalling; the bar graph represents a statistical summary of the experiments depicted in the plot to the left.

Gap-junction connected astrocyte – GJC astrocyte.

Data are presented as mean ± SEM; ns: $p > 0.05$; *$p < 0.05$.

4.4. Discussion

In this chapter, I have tested novel methodological approaches to monitor intracellular Ca^{2+} under pharmacological manipulations by applying dopamine or Aβ to astrocytes and neurons in acute brain slices. In the sections below, I evaluate the feasibility of these imaging methods by comparing the data obtained to published findings, mainly collected in cell cultures.

4.4.1. Dopamine-mediated [Ca^{2+}] signalling in astrocytes in brain tissue versus cell culture studies

One of the main results of this section is that astrocytes in acute hippocampal slices respond to dopamine application with an [Ca^{2+}] elevation. Dopamine has previously been shown to elevate [Ca^{2+}] levels in cultured astrocytes; using Fluor-3 AM, Parpura and Haydon (2000) showed that exposing astrocytes to 50 µM dopamine increased their internal [Ca^{2+}] to 3.5 µM. The application of ratiometric dyes by Vaarmann et al. (2010) allowed dose-depended relationships between the Ca^{2+} response and dopamine concentrations from 0.1–100 µM to be estimated; the maximum [Ca^{2+}] amplitude was reached upon exposure to 150 nM dopamine. Similarly, Requardt et al. (2012) showed a dose-dependent increase of the Ca^{2+} frequency, with a maximum of a two-fold change in fluorescence intensity. Here, taking advantage of the FLIM approach I showed that application of dopamine triggers an [Ca^{2+}] elevation in astrocytes, on average from 100 nM to 120 nM. Obtained in this chapter the dopamine-mediated rise in [Ca^{2+}] corresponds to results from cell culture studies over the last decade. The dramatic increase in [Ca^{2+}] levels reported in Parpura and Haydon (2000) might be explained by the method of dopamine application they used. The use of the pressurised application in cell culture might produce mechanical disruptions of the cells. Moreover, in cultures dopamine has also been shown to trigger neurotransmitter release from neurons (which could affect astrocytic

Ca^{2+} signalling through mGluR activation). It can also affect hippocampal interneurons by decreasing GABA release (lack of network inhibition might increase spontaneous glutamate release and contribute to the elevation of Ca^{2+} in astrocytes). In this chapter, I have shown that elimination of these factors by a potent drug cocktail (including an inhibitor of neuronal firing, and mGluR and GABA antagonists) does not suppress dopamine-mediated [Ca^{2+}] elevation in astrocytes.

My subsequent finding was that dopamine-mediated Ca^{2+} transients in astrocytes are followed by [Ca^{2+}] drop to below baseline during the washout period. A similar Ca^{2+} decrease was documented previously in cell culture studies (Khan et al., 2001). An earlier study in neurons of the nucleus accumbens showed that activation of type-2 dopamine receptors leads to a decrease of Ca^{2+} influx through L-type Ca^{2+} channels (Perez et al., 2011). Indeed, premature astrocytes have been shown to express functional voltage-gated calcium channels (VGCCs, including L-type Ca^{2+} channels) (Padmashri and Sikdar, 2007), contributing to the proposed effect of dopamine on decreases in [Ca^{2+}] levels in astrocytes.

4.4.2. Aβ-induced effects on astrocytic [Ca^{2+}] elevation in brain tissue versus changes in cell cultures

Another main finding in this chapter is that astrocytes in acute slices are capable of responding to localised Aβ oligomer application with an [Ca^{2+}] elevation comparable to that in cultures. The Aβ1–42 oligomers have previously been shown to induce an elevation in Ca^{2+} in astrocytes across a wide concentration range. Abramov et al. (2003) showed that astrocytes in cell cultures exposed to Aβ oligomers in a wide range of concentrations from 100 nM to 10 M exhibit irregular Ca^{2+} signalling. Further studies revealed a dose-dependence of intracellular Ca^{2+} signalling depending on the particular method of Aβ oligomer application used. For instance, Demuro et al. (2005) showed

that application of oligomers sharply elevated intracellular Ca^{2+}in astrocytes, with a maximum three-fold increase upon application of 12 g/ml oligomers (equivalent to about 150 nM). More recent findings reported by Drews et al. (2016) used delivery of oligomers directly to the cell surface in a concentration range found in patient CSF, confirming that intracellular Ca^{2+} in astrocytes increases upon Aβ1–42 application in a dose-response manner. A two-fold elevation of Ca^{2+} levels was caused by an increase in oligomer surface concentration from 5 to 500 pM, with maximum influx reached at a concentration of 1750 pM. Termination of Aβ exposure returns Ca^{2+} levels either to baseline or even below. Here, I showed that local application of Aβ oligomers to acute slices induced a two-fold [Ca^{2+}] elevation in the astrocyte of interest, which is in line with the results of published studies. Taking advantage of FLIM-based measurements, I also showed that an increase occurs, on average from a baseline level of 70 nM to an elevated level of 160 nM. Termination of pressurised delivery was accompanied by a return of [Ca^{2+}] back to the basal level. Even though the concentration of Aβ that I applied to astrocytes (1–10 nM near the surface of the cell) exceeds the Aβ concentration range found in the CSF of AD patients, it did not spread to neighbouring gap-junction astrocytes. This suggests that the extracellular environment in acute brain slices might play an essential role in spreading the large Aβ molecules. Moreover, an Aβ-mediated Ca^{2+} elevation in the astrocyte of interest did not propagate to the neighbouring cells via gap-junctions, also arguing for a further protective mechanism.

Several attempts were made to understand which cell type is more affected by exposure to Aβ oligomers. Primary culture studies have shown that bulk application of Aβ oligomers leaves Ca^{2+} dynamics in neurons unchanged (Abramov et al., 2003, 2004). A more recent finding suggests that local delivery of Aβ oligomers alters Ca^{2+} dynamics in astrocytes, but to a lesser degree than in neurons (Drews et al., 2016). In this chapter, I showed that neurons in hippocampal slices respond to Aβ oligomer application with an elevation of intracellular Ca^{2+}, up to 110 nM. Taking into account that the baseline level of Ca^{2+} in neurons is slightly higher compared to that in astrocytes and that the

Aβ-evoked response is smaller, I conclude that neurons can respond to Aβ exposure by elevating Ca^{2+}, but to a lesser degree than astrocytes.

The experimental findings in this section are in line with the previously reported Aβ oligomer-mediated [Ca^{2+}] elevation in astrocytes. Such an elevation does not lead to cell death; it does, however, provoke glutathione depletion in both astrocytes and neurons. The latter makes neurons more vulnerable to disruption produced by oxidative stress. This potential mechanism might explain the finding of memory impairment by Aβ oligomers *in vivo* (Walsh et al., 2002).

4.5. Conclusion

In this chapter, I have validated a methodology of fluorescence intensity and FLIM acquisition, along with experimental protocols for measuring dynamic [Ca^{2+}] changes in astrocytes in physiological and pathological conditions. Even though the main purpose of this chapter was to endorse advanced imaging approaches along with different options of substances delivery to the cells in acute brain slices, acquired data allow me to obtain following findings. Firstly, astrocytes *in situ* show bidirectional respond to dopamine application: profound Ca^{2+} elevation, followed by below baseline [Ca^{2+}] decrease during washout period. Furthermore, described [Ca^{2+}] elevation depended on D1/D2 receptors while the [Ca^{2+}] decrease involved D2 receptors only. Recorded dopamine-induced Ca^{2+} elevation was independent of neuronal firing activity, and of metabotropic glutamate or GABA receptors. Although dopamine-induce Ca^{2+} elevation is a well-documented by several studies performed in cultures, discovered in this chapter dopamine-dependent [Ca^{2+}] decrease is a novel finding. Secondly, in this chapter I demonstrated local delivery of Aβ oligomers to astrocytes *in situ* induce [Ca^{2+}] increase. This effect is well established in the literature, mainly through experiments performed in cellular cultures or organotipic preparations. Here, taking

advantage of direct delivery of Aβ oligomers to the astrocyte of interest (even with oligomers concentration exceeding the range associated with AD) afformed [Ca^{2+}] increase only was measured in targeted astrocyte. Aβ oligomers left intact [Ca^{2+}] levels in neighbouring astrocytes, suggesting key role of extracellular environment in prevent spreading of large Aβ aggregates in the tissue.

Chapter 5

Synaptic accumulation of K^+ slows down glutamate uptake by astrocytic transporters and enhances glutamate spillover

5.1. Introduction

Accurate signal transduction in the brain depends on maintaining a low extracellular concentration of the main excitatory neurotransmitter glutamate. Accumulation of extracellular glutamate leads to excitotoxicity, making neurons vulnerable to pathologies such as stroke, epilepsy, Parkinson's disease, and Alzheimer's disease (for a review see Meldrum, 2018). The low glutamate concentration in the synaptic cleft is achieved by rapid diffusion escape (Rusakov and Kullmann, 1998; Bergles et al., 1999) followed by uptake by Na^+-dependent high-affinity glutamate transporters (Diamond and Jahr, 1997; Bergles and Jahr, 1998) from a family of excitatory amino acid transporters (EAATs). Both neurons and glial cell express glutamate transporters. Predominantly expressed in astrocytic processes, the EAAT-1 and EAAT-2 transporter subtypes are responsible for the majority of glutamate uptake (Haugeto et al., 1996). These transporters provide efficient electrogenic glutamate uptake by transporting three Na^+ and one H^+ ion inside the cell while extruding one K^+ ion down its concentration gradient. The Na^+/K^+ balance is essential for the efficient functioning of the glutamate transporter (Unichenko et al., 2012; Rimmele et al., 2017). Glial cells are depolarised in response either to artificial elevation of extracellular K^+ (Ransom and Goldring, 1973) or to synaptic transmission associated with K^+ accumulation in the synaptic cleft (Amzica et al., 2002; Meeks and Mennerick, 2007; Chever et al., 2010). Moreover, high-frequency electrical stimulation of Schaffer collaterals in the hippocampus not only triggers long-term potentiation (LTP) but also leads to sustained depolarisation of astrocytes, which is abolished by an NMDA

receptor antagonist (Ge and Duan, 2007). This effect is considered to be mediated by suppressing the operation of astrocytic transporters. Despite the fact that astrocytes are indeed depolarised during synaptic transmission and possess voltage-dependent properties (Wadiche et al., 1995; Grewer et al., 2000), the efficiency at which they take up glutamate under physiological synaptic transmission remains poorly understood.

In this chapter, my experimental data provide novel insights into the mechanism of astrocytic transporter glutamate uptake during physiological K^+ accumulation and the implications of this uptake for cross-talk between neighbouring synapses.

5.2. Methods

To meet the objectives of this chapter, I performed recordings from astrocytes and neurons in acute hippocampal slices from P21–25 wild type (WT) male C57BL/6 or CA1-GluN1 KO mice (Tsien et al., 1996). Recordings were performed on a Femto-2D system, equipped with motorised manipulators, which are required for patch-clamp recordings. During all experiments, the temperature of the extracellular solution was maintained at 32–34°C.

Synaptic responses were elicited by stimulation of SC with a concentric electrode, which was placed 150–200 µm from the recorded cells. Whole-cell recordings from astrocytes were obtained using patch electrodes filled with a KMS-based solution containing (in mM): KCH_3O_3S, 135; HEPES, 10; $MgCl_2$, 4; phosphocreatine disodium, 10; Na_2ATP, 10; NaGTP, 0.4 (pH adjusted to 7.2 with KOH; osmolarity-adjusted to 290–295 mOsM). Pharmacological isolation of the glutamate transporter current was achieved by recording the inward current in the control condition and during application of the transporter antagonist DL-TBOA (50 µM); this was followed by post-hoc subtraction of K^+ currents from the mixed current. Whole-cell recordings from CA1 pyramidal neurons were performed using patch electrodes filled with a modified KMS-

based solution containing (in mM): KCH_3O_3S, 130; NaCl 8; HEPES, 10; phosphocreatine disodium, 10; Na_2GTP, 0.4; MgATP, 4; and Na-ascorbate, 3 (pH adjusted to 7.2 with KOH; osmolarity-adjusted to 290–295 mOsM). For experiments in sections 5.3.7. to 5.3.9, I used an NMDG-based internal solution to eliminate postsynaptic K^+ efflux. Recorded signals were amplified with a Multiclamp 700B amplifier, filtered at 2–5 kHz, and recorded and digitised at 4–10 kHz with the National Instruments card (Texas, USA).

For two-photon excitation fluorescent intensity imaging, emitted light from the sample was split into two channels: 500–530 nm (for iGluSnFR, two-photon excitation wavelength 910 nm) and 540–700 nm (for Alexa-594, two-photon excitation wavelength 800 nm). For visualisation of the cell of interest, I supplemented the internal solution with the morphological tracer dye Alexa-594. Fluorescence intensity data collected from dendritic spines with the line-scan at a rate of ~500 Hz. The signal for each dendritic spine was calculated as the averaged fluorescence normalised to the baseline segment prior to stimulation (ΔF/F). In section 5.3.8, I employed acute slices transduced with a glutamate sensor (iGluSnFR) to directly assess glutamate spillover. To achieve this, injections of the glutamate sensor AAV2/1 h.Syn iGluSnFR (1×10^8 genomic copies in an injected volume) were performed to P0–3 neonatal pups in a volume not exceeding 2.5 µL per hemisphere. The virus was injected to a right lateral ventricle (2/5 of the distance from the lambda suture to each eye) using a Hamilton needle (Jankowsky et al., 2014). Acute hippocampal slices were prepared 2–3 weeks after AAV injection. Glutamate uncaging was employed, using application of caged L-glutamate (4-methoxy-7-nitroindolinyl-caged L-glutamate, 200 µM) to the perfusion solution, and carried out using a Mai-Tai laser tuned to 720 nm. The uncaging spot was selected based on the Alexa-594 channel and was located next to the somata of the astrocytes.

5.3. Results

5.3.1. NMDA receptors-mediated K^+ efflux facilitates amplitude of the astrocytic glutamate transporter current

Shih et al. (2013) have shown that K^+ accumulation in hippocampal CA3–CA1 synapses underlies activity-dependent facilitation of presynaptic glutamate release. Here, by assessing the amplitude of glutamate transporter currents, I examine if repetitive SC stimulation affects astrocytic glutamate uptake (I_{gluT}; Figure 5.1a–c). Indeed, the recorded glutamate transporter currents demonstrated activity-dependent facilitation, with an increase of the response amplitude to each stimulus (recordings for the control group, performed in the absence of any ionotropic receptors antagonists are depicted in grey in Figure 5.1b–c). As previously suggested (Shih et al., 2013), activity-dependent facilitation of glutamate release is mediated by K^+ efflux through NMDA receptors. To determine the predominant receptor subtype responsible for K^+ accumulation in the given conditions and its impact on astrocytic glutamate currents, I employed a pharmacological block of ionotropic receptors. Either D-APV or D-APV/NBQX were added to the perfusion system to block NMDA or NMDA/AMPA receptors, respectively (Figure 5.1b). Application of D-APV significantly reduced activity-dependent facilitation of glutamate transporter currents ($n = 6$; $p_{APV} < 0.001$, $p_{stimulus} < 0.001$, $p_{APV \times stimulus} < 0.01$, two-way RM ANOVA; Figure 5.1c). While simultaneous introduction of D-APV and NBQX to the perfusion system did not reduce the facilitation of transporter currents any further. These results indicate that NMDA, rather than AMPA, receptors are the predominant source of K^+ accumulation during synaptic transmission.

5.3.2. NMDA receptors-mediated K^+ efflux slows down the glutamate uptake rate by astrocytic transporters

The same data set (TBOA-sensitive currents) was used to estimate the efficacy of glutamate transporter glutamate uptake, measured as the decay time (Ƭ decay). This parameter is obtained from the exponential approximation of the current decay, from the peak to the baseline. I found that, during single stimulations, astrocytic glutamate transporters the decay time was 5.75 ± 0.65 ms (n = 12; Figure 5.1d). Interestingly, in spite of the ionotropic receptor block, the decay time stayed in the range of 5–6 ms. In particular, the time was not affected by D-APV (Ƭ decay = 5.26 ± 0.80 ms, n = 6; p > 0.05 for the difference between the control and D-APV groups; Figure 5.1d) or D-APV/NBQX application (Ƭ decay = 4.83 ± 0.92 ms, n = 6; p > 0.05 for the difference between the control and D-APV/NBQX groups, two-sample t-test; Figure 5.1d).

The activity-dependent facilitation of the amplitude of glutamate transporter currents suggests that major changes in decay time might occur during repetitive stimulation. Indeed, delivery of five stimuli to SC induced an increase in decay time to 23.65 ± 3.22 ms (n = 12; p < 0.001 for the difference compared to the single stimulation, paired-sample t-test; Figure 5.1d). Application of D-APV diminished the prolongation of decay time to 12.71 ± 1.91 ms (n = 6; p < 0.01 for the difference with the control group, two-sample t-test; Figure 5.1d). An even greater reduction was observed during the application of D-APV and NBQX together; however, their combined effect was not significant compared to D-APV alone (Ƭ decay = 7.91 ± 1.35 ms, n = 6; p < 0.001 for the difference with the control group, p > 0.05 for the difference with the D-APV group, two-sample t-test; Figure 5.1d). These findings suggest that during repetitive stimulation NMDA receptor-mediated K^+ efflux is sufficient to slow down the rate of glutamate uptake by astrocytic transporters.

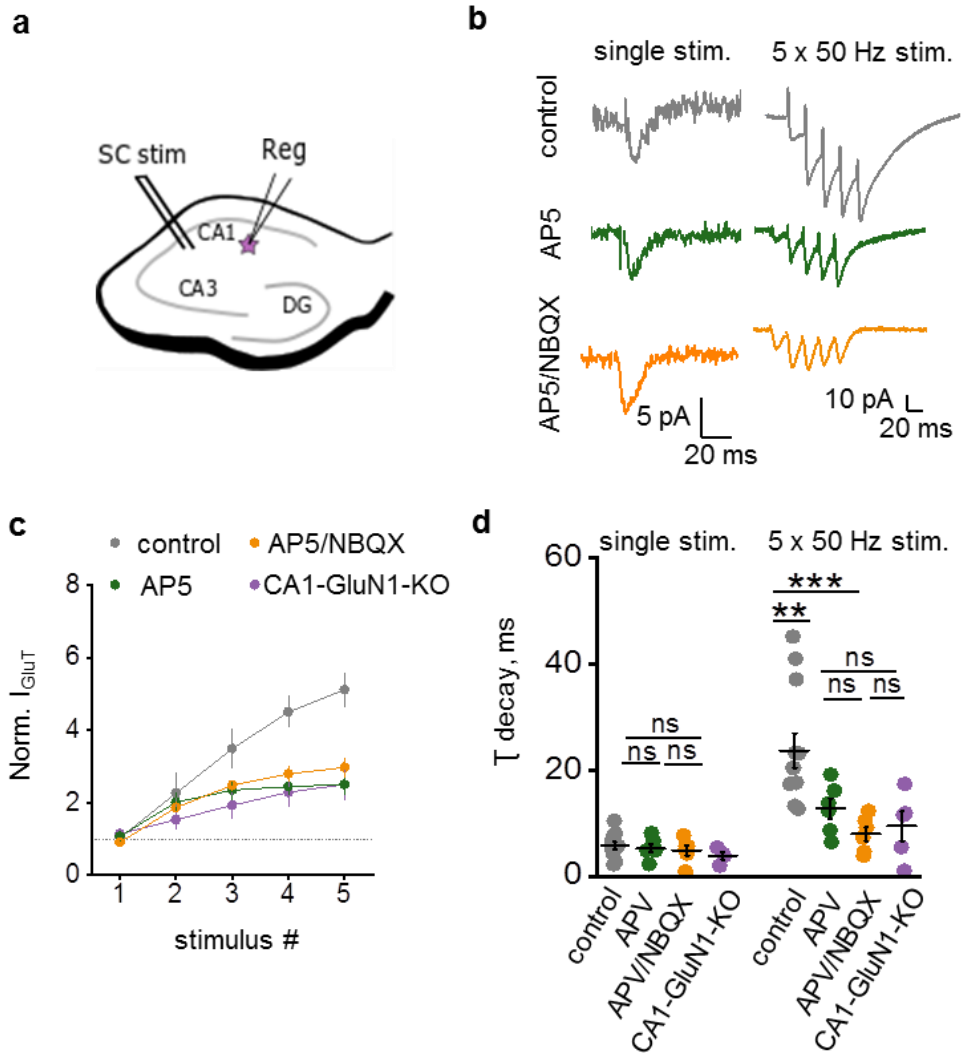

Figure 5.1 Activity-dependent K^+-efflux through postsynaptic NMDA receptors facilitates the glutamate transporter current

a- Scheme representing electrode positions required for recording inward currents in a CA1 *stratum radiatum* astrocyte

b- Sample traces of glutamate transporter currents (I_{GluT}) recorded in the absence of any receptor antagonists (control, grey), or with the application of D-AP5 (green) or D-AP5/NBQX (orange)

c- Glutamate transporter current amplitudes (I_{GluT}) during repetitive synaptic stimulation (5 × 50 Hz), normalised to the amplitude of I_{GluT} in response to a single stimulation. Activity-dependent facilitation in the control group (grey) was reduced by the application of D-APV (green) or D-APV/NBQX (orange), and in CA1-GluN1-KO mice (purple)

d- The time required for glutamate translocation by transporters (τ decay) in response to single or repetitive stimulation. The decay time recorded for

single stimulation did not significantly differ between control (grey), APV (green), or D-APV/NBQX groups (orange), or in CA1-GluN1-KO mice (purple). The decay time in the control group was significantly larger in response 5 × 50 Hz stimulation than in the D-APV or D-APV/NBQX groups or in CA1-GluN1-KO mice.

Data are presented as mean ± SEM; ns: $p > 0.05$; **$p < 0.01$, ***$p < 0.001$.

5.3.3. Postsynaptic NMDA receptors are a predominant source of K^+ efflux

The activity-dependent recruitment of NMDA receptors increases the amplitude of the transporter current at the same time as extending its decay time. However, the application of an NMDA receptor antagonist in the perfusion solution blocks receptors in both pre- and postsynaptic terminals, which prevents their individual impacts from being separated. With the aim of identifying the role of postsynaptic NMDA receptors in the mechanism described, I recorded astrocytic glutamate transporter currents from a conditional knockout mice line. CA1-GluN1-KO mice lack the GluN-1 subunit of functional NMDA receptors in CA1 pyramidal neurons (Tsien et al., 1996). The recorded activity-dependent facilitation of the transporter current was not significantly different from that recorded when NMDA receptors were blocked with D-APV (Figure 5.1c). The lack of functional postsynaptic NMDA receptors in CA1-GluN1-KO mice did not significantly reduce the decay time of the glutamate transporter current, evoked either with single (τ decay = 3.82 ± 0.69 ms, n = 4; $p > 0.05$ for the difference with the D-APV group, two-sample t-test) or with repetitive stimulation (τ decay = 9.42 ± 2.82 ms, n = 5; $p > 0.05$ for the difference with the D-APV group, two-sample t-test; Figure 5.1d). These results indicate an inconsequential effect of presynaptic NMDA receptors on activity-dependent facilitation of transporter currents. This implies that during neuronal firing, the more substantial proportion of K^+ ions accumulates through postsynaptic NMDA receptors.

5.3.4. Recruitment of additional Schafer collaterals fibres does not affect glutamate uptake by astrocytic transporters

The proposed mechanism of transporter current facilitation is mediated by K^+ efflux through postsynaptic NMDA receptors. At the resting membrane potential, NMDA receptors are blocked with Mg^{2+} ions and their removal is essential for current flow (Nowak et al., 1984). This process has been shown to be voltage-dependent. Accordingly, the induction of larger postsynaptic depolarisation would recruit more NMDA receptors and produce extensive K^+ efflux. In this section, I address how the engagement of additional SC fibres would affect glutamate transporter currents. To investigate this, I recorded glutamate transporter currents evoked under either weak or strong stimulation (traces normalised to a single stimulation of SC depicted in Figure 5.2a). Firstly, I recorded glutamate transporter currents during weak stimulation of afferent fibres (stimulation strength was adjusted to evoke a ~10 pA amplitude inward current). Next, I increased the stimulation strength (the strong stimulation condition) to evoke double the latter inward current amplitude. Increasing the stimulation strength increased the absolute glutamate transporter current amplitude from 11.74 ± 0.84 pA to 17.07 ± 1.80 pA ($n = 8$; $p < 0.05$, paired sample t-test; Figure 5.2b). Notably, there was no significant enhancement of the normalised glutamate transporter current facilitation ($n = 7$; $p_{strength} > 0.05$, $p_{stimulus} < 0.001$, $p_{strength \times stimulus} > 0.05$, two-way RM ANOVA; Figure 5.2c). Increasing the stimulation strength left the decay time of the transporter current evoked by a single stimulation unaffected (Ƭ decay = 5.89 ± 1.34 ms, $n = 6$; $p > 0.05$, paired sample t-test; Figure 5.2d). Unexpectedly, strong repetitive stimulation did not affect the decay time (Ƭ decay = 25.29 ± 3.77 ms, $n = 6$; $p > 0.05$, paired sample t-test; Figure 5.2d). This finding suggests that both stimulation strengths activate sufficient numbers of NMDA receptors. Moreover, the recruitment of additional NMDA receptors does not affect activity-dependent facilitation of glutamate transporter currents.

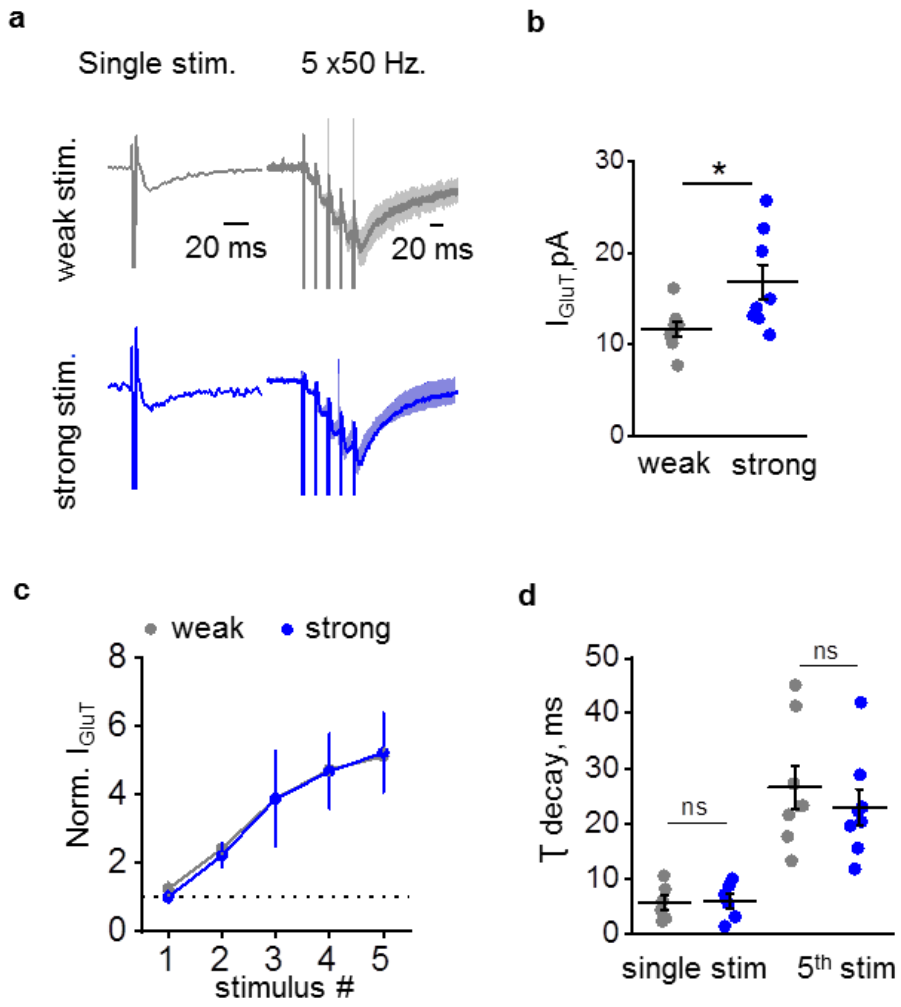

Figure 5.2 Recruitment of additional Schafer collaterals fibres does not affect astrocytic glutamate transporter currents

a- Glutamate transporter current (I_{GluT}) recorded during weak (grey) or strong (blue) SC stimulation. The traces are normalised to a single stimulation delivered to SC and traces for the 5 × 50 Hz stimulation averaged across all experiments

b- Summary plot showing an increase in the absolute amplitude of I_{GluT} with strong stimulation

c- The increase in stimulation strength did not affect activity-dependent facilitation of normalised glutamate transporter current (I_{GluT})

d- The decay time of glutamate transporter currents did not change with increasing stimulation strength.

Data are presented as mean ± SEM; ns: $p > 0.05$, *$p < 0.05$.

5.3.5. Depolarisation of the astrocytic membrane but not a decrease in K^+ gradient slows down glutamate uptake by transporters

Two mechanisms could contribute to the prolongation of the glutamate transporter current: 1) depolarisation of the astrocytic membrane; and 2) decrease of the transmembrane K^+ gradient. To investigate the relative impact of these two factors, we recorded glutamate transporter current in response to glutamate uncaging (uI_{GluT}). The uncaging spot was next to the astrocytic soma, to facilitate voltage transfer from the clamp pipette (Figure 5.3a). An increase in the extracellular [K^+] caused concentration-dependent depolarisation of the astrocyte held in current-clamp mode. In particular, the increase of extracellular [K^+] from 2.5 to 7.5 mM depolarised the astrocytic membrane to 9.80 ± 1.00 mV (n = 12), while exposure to 20 mM [K^+] further depolarised the membrane to 43.80 ± 1.30 mV (n = 4), relative to the resting membrane potential of the cell (Figure 5.3b). Such K^+-induced depolarisation was mimicked by holding the cell in voltage-clamp mode at membrane potentials equivalent to those produced by the applications of K^+. Membrane depolarisation alone or during the application of corresponding concentrations of K^+ induced a similar reduction in glutamate transporter current (n = 7; $p_{K^+} > 0.05$, $p_{depolarisation} < 0.001$, $p_{K^+ \times depolarisation} > 0.05$, two-way RM ANOVA; Figure 5.3c). These findings suggest that depolarisation alone modulates glutamate uptake, while increases in [K^+] do not have an additive effect. We also observed a depolarisation-dependent increase in the decay time of the glutamate transporter current (n = 8; $p < 0.01$, one-way RM ANOVA; Figure 5.3d). No decrease in the amplitude of the glutamate transporter current was measured when a cell was held at a constant membrane potential of -85 mV while extracellular [K^+] was changed (2.5 mM: n = 4; 7.5 mM: n = 8; 20 mM: n = 4; $p > 0.05$, one-way RM ANOVA; Figure 5.3e).

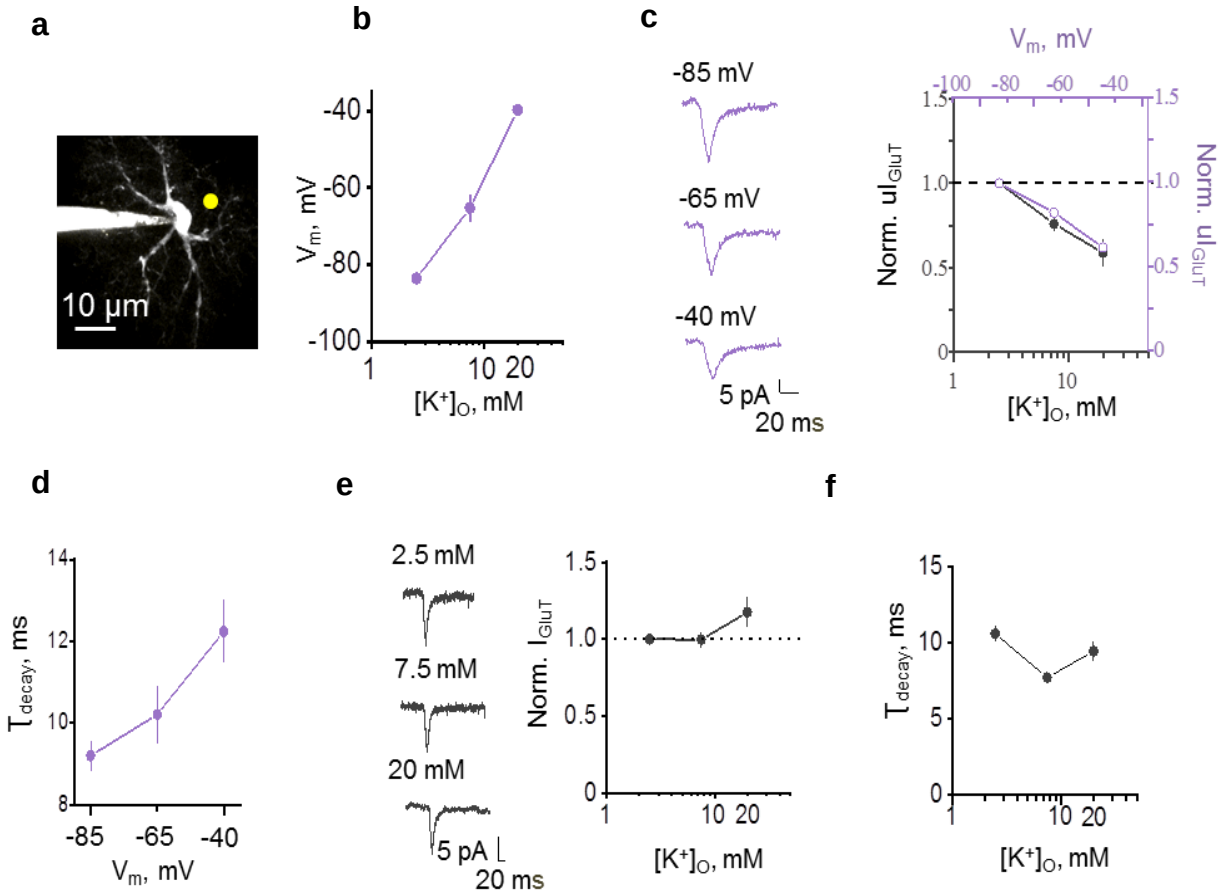

Figure 5.3 Astrocytic depolarisation slows down glutamate uptake by transporters

a- Image of the experiment performed, with a CA1 *stratum radiatum* astrocyte patched with the morphological tracer Alexa-594. The glutamate uncaging spot (yellow dot) was placed next to the cell soma.

b- Elevation of extracellular $[K^+]$ led to depolarisation of the astrocytic membrane

c- *Left*: Sample glutamate transporter current traces evoked by glutamate uncaging (ul_{GluT}) while holding the astrocyte at different membrane potentials (Vm). *Right*: Summary plot showing normalized ul_{GluT} amplitude recorded from cells voltage-clamped at -85, -65, and -40 mV (purple circles) and in the cells clamped at the same voltages, but with $[K^+]$ corresponding to the voltages in (b) (2.5, 7.5, and 20 mM; black circles). Increasing $[K^+]$ did not have any additional effect on cell depolarisation

d- Summary plot showing the decay time of ul_{GluT} while cells were voltage-clamped at -85, -65, and -40 mV

e- *Left:* Sample traces of ul_{GluT} produced by glutamate uncaging while holding an astrocyte at -85 mV and exposing it to K^+ at 2.5, 7.5, and 20

mM; *Right*: Summary plot showing normalised uI_{GluT} amplitude in cells exposed to different $[K^+]$

f- Summary plot showing the decay time of uI_{GluT} in the cells depicted in c and voltage-clamped at -85 mV and exposed to $[K^+]$: 2.5, 7.5, and 20 mM

Data are presented as mean ± SEM.

Experiments were performed by Dr Pei-Yu Shih.

Moreover, the glutamate decay time stayed the same and did not show any significant increase (2.5 mM: n = 11; 7.5 mM: n = 7; 20 mM: n = 4; $p < 0.01$, one-way RM ANOVA; Figure 5.3f). Thus, the rise in extracellular $[K^+]$ affected the rate of glutamate uptake by transporters mainly via depolarisation of the astrocytic membrane, rather than by reducing the transmembrane K^+ gradient.

5.3.6. Increase of glutamate transporters decay time is abolished by the blockade of astrocytic Kir channels

Next, to evaluate the impact of K^+ channels on resting membrane potential and transporter decay time, I recorded transporter currents from astrocytes using modified internal solutions. Introduction of $BaCl_2$ to the solution predominantly blocks the pore of the Kir4.1 channel (traces normalised to a single stimulation of SC depicted in Figure 5.4a). Such an alteration produced small but significant depolarisation of the astrocytic membrane (V_m = -82.66 ± 1.85 mV for the control group, n = 9; V_m= -71.42 ± 1.73 mV for the group with $BaCl_2$ in the solution, n = 7; $p < 0.01$, two-sample t-test; Figure 5.4b). Blocking the K^+ conductance in astrocytes did not change the activity-dependent facilitation of glutamate transporter current amplitude (n = 6; $p_{BaCl2} > 0.05$, $p_{stimulus} < 0.001$, $p_{BaCl2 \times stimulus} > 0.05$, two-way RM-ANOVA; Figure 5.4c). However, I did record changes in the glutamate transporter decay time induced by a single stimulation, which increased from

5.93 ± 0.41 ms to 18.55 ± 2.79 ms (n = 6; $p < 0.01$ for the difference with the control group, two-sample t-test; Figure 5.4d). Interestingly, the increase in decay time was similar to the decay time evoked by repetitive stimulation under the control condition (τ decay = 20.03 ± 4.59 ms, n = 6; $p > 0.05$, two-sample t-test; Figure 5.4d). Recordings of glutamate transporter currents from patch-clamped astrocytes with $BaCl_2$ under repetitive stimulation did not show any further increase in decay time (τ decay = 20.03 ± 4.59 ms, n = 6; $p < 0.05$, paired-sample t-test; Figure 5.4d). Therefore, supplementation of the internal solution with $BaCl_2$ makes the astrocytic membrane insensitive to activity-dependent K^+ accumulation. These findings suggest that astrocytic Kir4.1 channels-depended membrane depolarisation slows down the rate of glutamate transporter.

5.3.7. K^+ efflux through NMDA receptors extends glutamate dwell-time: electrophysiological observations

The glutamate transporter current recorded from astrocytes does not faithfully represent changes in extracellular glutamate concentration. In fact, when glutamate translocation is reduced, more transporters can diffuse to the site of the synaptic transmission and participate in the buffering of extracellular glutamate (Murphy-Royal et al., 2015). Increased buffering capacity is likely to increase glutamate dwell-time in the synaptic cleft extending activation time of neuronal receptors. Here, to investigate physiological effect of prolonged glutamate presence in and around the synapse, we recorded excitatory postsynaptic potentials (EPSPs) from CA1 pyramidal neurons. To evaluate the K^+-mediated effect on glutamate dwell-time, pyramidal neurons were patch-clamped either with a KMS-based internal solution or with a solution in which K^+ ions were replaced with $NMDG^+$ ions (the NMDG-based internal solution) (Figure 5.5a).

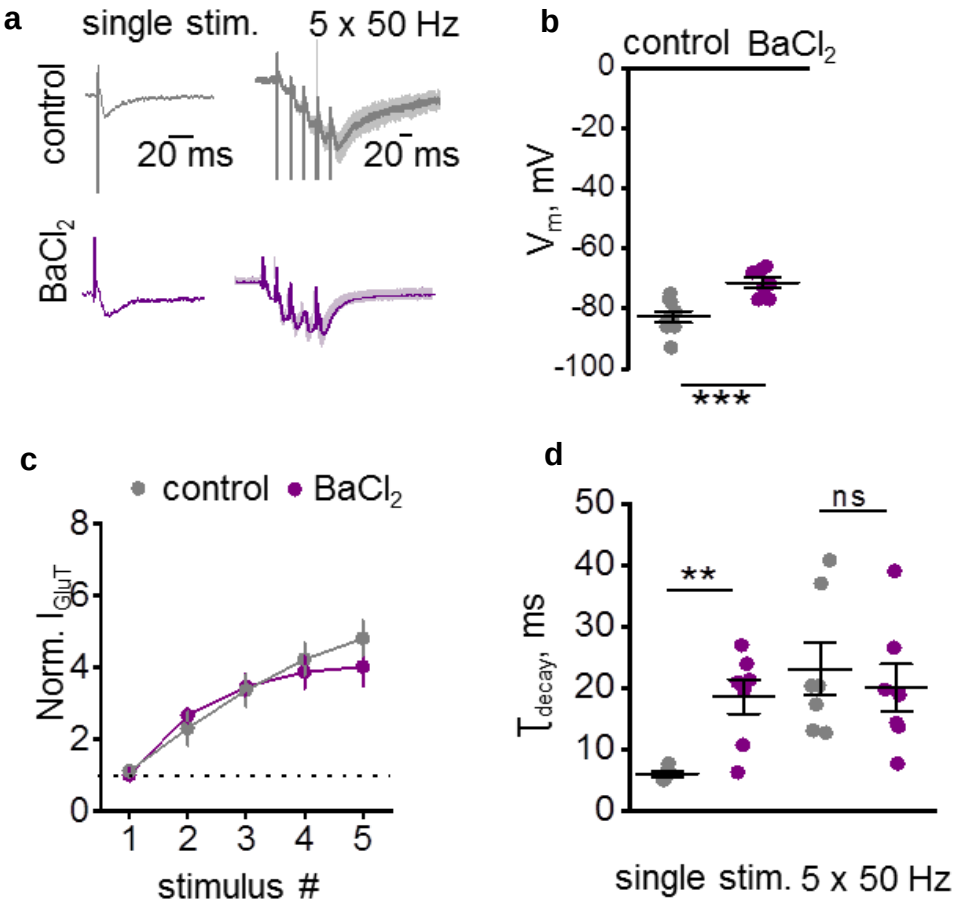

Figure 5.4 Blocking astrocytic K^+ channels extend decay time of glutamate transporter current

a- Glutamate transporter current (I_{GluT}) recorded with KMS-based intracellular solution (grey) and solution implemented with $BaCl_2$ (purple). The traces are normalised to a single stimulation delivered to SC and traces for the 5 × 50 Hz stimulation averaged across all experiments

b- The summary plot shows that supplementation of the internal solution with $BaCl_2$ depolarise astrocytic membrane

c- The summary plot shows that implementation of the intracellular solution with $BaCl_2$ does not affect activity-dependent facilitation of astrocytic glutamate transporter currents

d- The summary plot shows that supplementation of the internal solution with $BaCl_2$ increase glutamate transporter currents decay time for single stimulation and left intact glutamate transporter current evoked with repetitive stimulation.

Data are presented as mean ± SEM; ns $p > 0.05$, **$p < 0.01$ and ***$p < 0.001$

The KMS-based solution allowed K^+ efflux through postsynaptic receptors, which accelerates EPSP decay time. Therefore, the decay time of EPSPs evoked by a single stimulation of SC was smaller in the KMS (τ decay = 91.61 ± 20.63 ms, n = 7) than in the NMDG recordings (τ decay = 210.87 ± 24.52 ms, n = 6; $p < 0.01$, two-sample t-test; Figure 5.5b). Similarly, the decay time of EPSPs evoked by a 5 × 50 Hz stimulation was smaller in the KMS-based solution (τ decay = 136.52 ± 17.02 ms, n = 6) compared to the NMDG-based solution (τ decay = 221.90 ± 23.51 ms, n = 6; $p < 0.05$, two-sample t-test; Figure 5.5c). Post-hoc measurement of the decay time ratio, calculated as τ(5 × 50 Hz) / τ(single), revealed that indeed, the decay time of postsynaptic potentials was longer when cells were patch-clamped with the KMS-based internal solution (τ decay ratio = 1.4 ± 0.14, n = 6; $p < 0.05$, single sample t-test for the ratio) rather than the NMDG-based internal solution (τ decay ratio = 1.06 ± 0.05, n = 6; $p > 0.05$, single sample t-test for the ratio; Figure 5.5d). This finding suggests that glutamate dwell-time in the synaptic cleft is regulated by K^+ efflux from the postsynaptic neuron. Alternatively, this result may reflect voltage- and activity-dependent regulation of the K^+ current curtailing EPSPs.

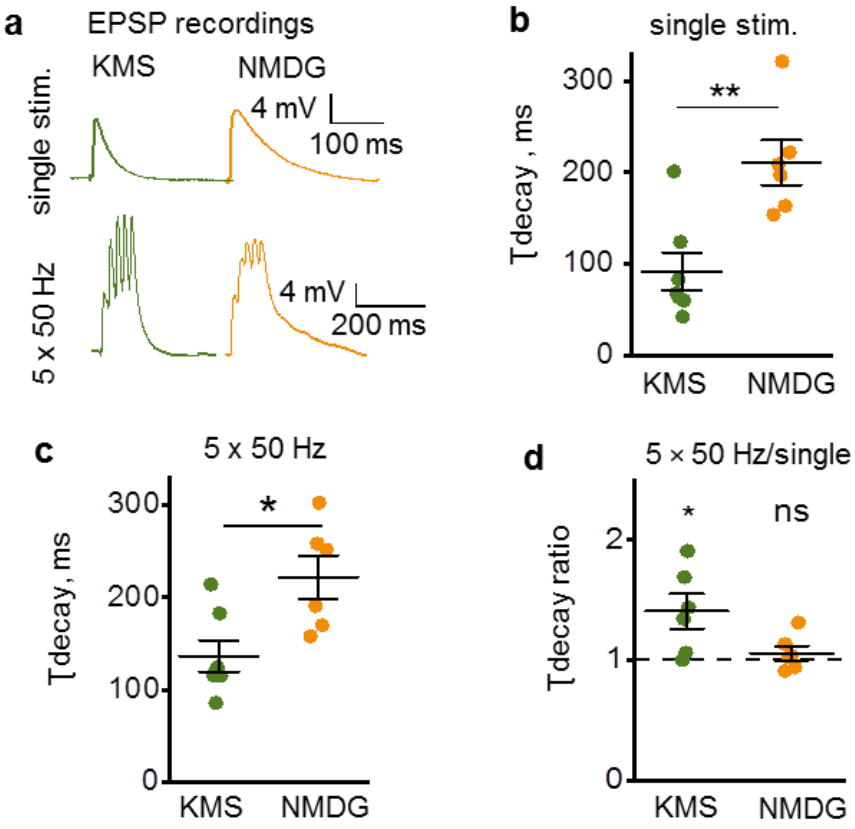

Figure 5.5 K^+ efflux extends glutamate dwell-time in the synaptic cleft: electrophysiological observations

a- Sample traces of EPSPs recorded from CA1 pyramidal neurons filled with KMS- or NMDG-based internal solutions in response to single and 5 × 50 Hz SC stimulation

b- Summary plot of EPSP decay time in response to a single stimulation. Replacing intracellular K^+ (green) with $NMDG^+$ (orange) significantly increased the decay time to both single and 5 × 50 Hz SC stimulation

c- Summary plot of EPSP decay time in response to 5 × 50 Hz stimulation; colour coding is the same as in (b)

d- Summary plot representing the decay time ratio of EPSPs (EPSP decay time evoked by 5 × 50 Hz stimulation/EPSP decay time evoked by a single stimulation). Activity-dependent prolongation of EPSPs was observed when the cells were filled with a KMS- but not with an NMDG-based solution

Data are presented as mean ± SEM; ns: $p > 0.05$, *$p < 0.05$, **$p < 0.01$.

Experiments were performed by Dr Yulia Dembitskaya.

5.3.8. K^+ efflux through NMDA receptors extends glutamate dwell-time: iGluSnFR fluorescence observations

To further address whether K^+ accumulation extends glutamate dwell-time in the synaptic cleft, I directly measured postsynaptic glutamate transients with the genetically-encoded glutamate sensor – iGluSnFR (Figure 5.6a). To achieve this, CA1 pyramidal neurons expressing glutamate sensor were loaded either with KMS- or with NMDG-based intracellular solution supplemented with the morphological-tracer dye Alexa-594. Next, I recorded the fluorescence intensity signal from individual dendritic spines using the line-scan method (Figure 5.6a–c). Synaptic transmission was induced by SC stimulation with 5 stimuli at 50 Hz. The decay time of glutamate transients was significantly longer in cells loaded with the KMS-based intracellular solution (τ decay = 31.56 ± 2.04 ms, n = 53 spines) than the NMDG-based solution (τ decay = 21.80 ± 1.65 ms, n = 20 spines; $p < 0.001$, two-sample *t*-test; Figure 5.6d). This finding underlines the fact that K^+ efflux from the postsynaptic terminal does indeed contribute to a prolongation of glutamate dwell-time and extensive accumulation of glutamate.

5.3.9. K^+ efflux through NMDA receptors enhances glutamate spillover

Extending glutamate dwell-time in the synaptic cleft environment might enhance spillover and facilitate inter-synaptic crosstalk. To test this hypothesis, I stimulated independent populations of afferent fibres converging on the same recorded cell (the two-pathway experiment described in Scimemi, 2004). Such an approach allowed me to test NMDA receptor-mediated crosstalk between neighbouring networks and estimate the amount of spillover. In brief, I made a cut between the CA2 and CA1

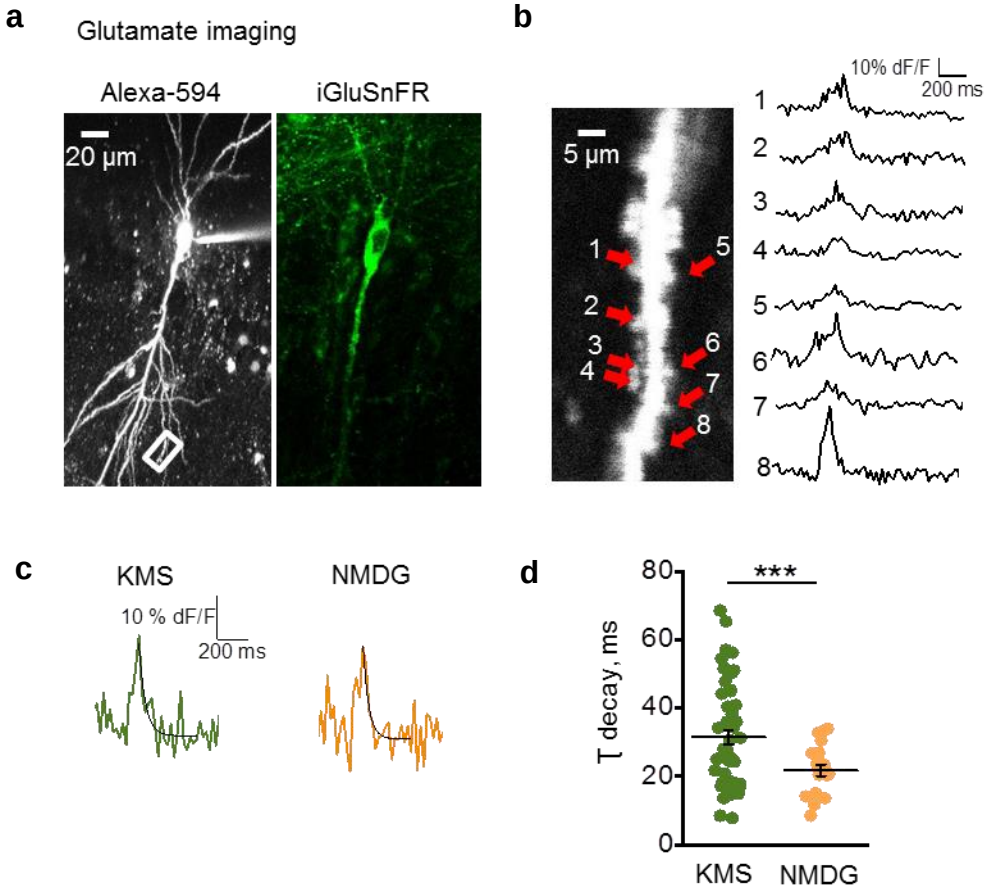

Figure 5.6 K^+ efflux extends synaptic glutamate dwell-time: iGluSnFR fluorescence observations

a- Glutamate imaging of a CA1 pyramidal neuron expressing the glutamate sensor (iGluSnFR) and loaded with Alexa-594 through the patch pipette
b- *Left:* Zoomed area depicted with the rectangle in (a), showing individual dendritic spines. Arrows indicate the analysed spines. *Right*: Glutamate fluorescence intensity traces recorded at the corresponding spines
c- Glutamate fluorescence intensity traces recorded with KMS- or NMDG-internal solution; exponential fit represented by the black line
d- Summary plot showing the decay time of glutamate transients in dendritic spines from two neurons. The substitution of K^+ with $NMDG^+$ shortened the glutamate dwell-time around dendritic spines.

Data are presented as mean ± SEM; ***p < 0.001.

regions to prevent the spread of recurrent activity and recorded NMDA receptor-mediated EPSPs. To isolate the NMDA component, I performed these recordings with AMPA and $GABA_A$ receptor antagonists, and to remove the Mg^{2+} block from NMDA receptors, I used depolarising voltage steps to -40 mV. To elicit synaptic transmission from independent pathways, two concentric electrodes were placed in CA1 *stratum radiatum* on opposite sides of the recorded cell (Figure 5.7a). The lack of any cross-facilitation of EPSPs in response to paired stimulation was used to confirm independence of the pathways (Figure 5.7b). After baseline recordings in both pathways, the stimulation of one pathway was stopped (silent pathway) and the activity-dependent NMDA receptor blocker MK-801 (4 µm) was introduced to the perfusion system. High-frequency stimulation (HFS) was delivered to the active pathway. This stimulation led to the blockade of NMDA receptors at active pathway synapses and some synapses at the silent pathway, which were reached by glutamate escaping from the active synapses (Figure 5.7c). The proportion of synapses blocked by MK-801 in the silent pathway was estimated upon drug washout and was larger when the cell was filled with the KMS- (42.02 ± 4.74 % of baseline, n = 7) than the NMDG-based intracellular solution (63.91 ± 6.15 % of baseline, n = 6; $p < 0.05$, two-sample *t*-test; Figure 5.7d). This finding highlights the importance of K^+ efflux from the postsynaptic terminal and suggests that K^+ efflux from the postsynaptic neuron promotes glutamate spillover-mediated synaptic crosstalk.

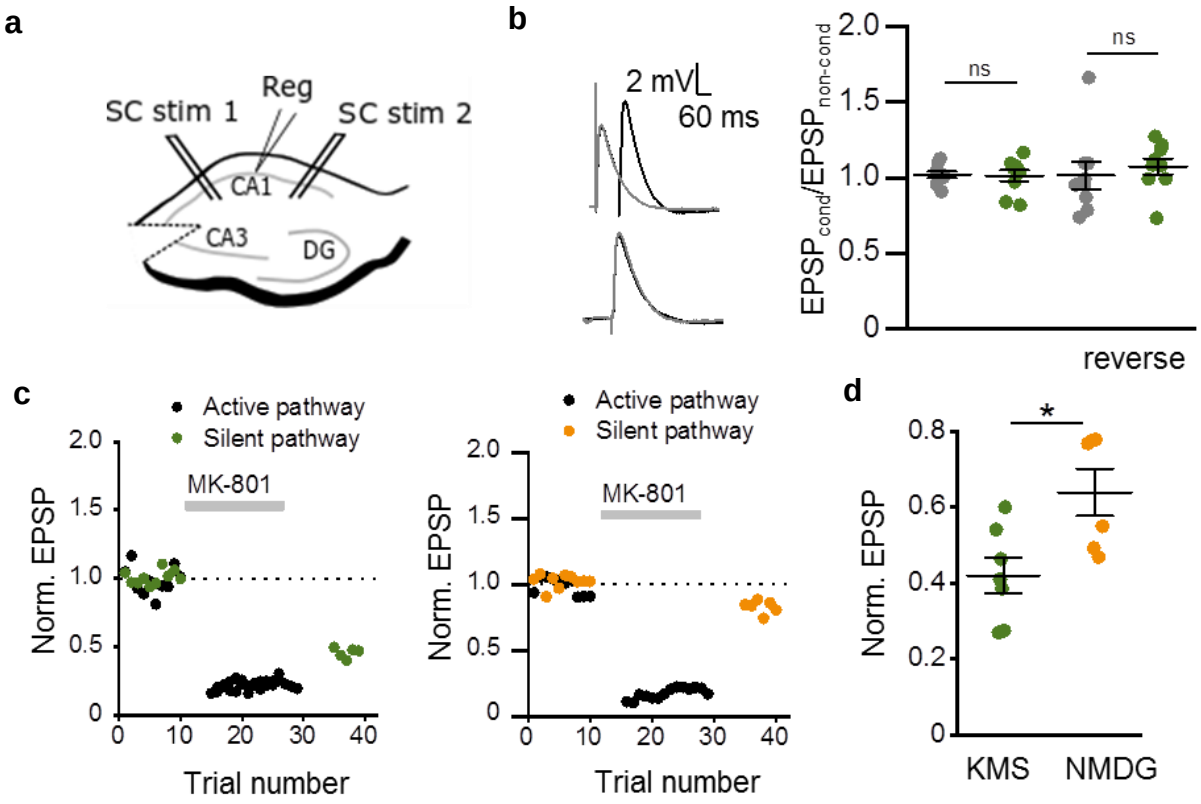

Figure 5.7 K^+ efflux through NMDA receptors enhances crosstalk between neighbouring networks

a- Scheme representing the electrode positions required for activating two populations of independent afferent fibres, converging on the recorded cell. EPSPs were recorded from CA1 pyramidal neurons

b- Testing the independence of the afferent pathways. *Left*: Sample traces of conditioned EPSPs (EPSPs in the silent pathway were preceded by EPSPs in the active pathway) and unconditioned EPSPs. *Right*: Ratios of EPSPs obtained with alternating pathway stimulation did not show enhanced cross-facilitation, confirming the independence of the stimulated pathways

c- Single-cell example for KMS- (*left*) and NMDG-based internal solutions (*right*); the baseline represents the normalised EPSP amplitude of for each pathway. Application of 4 µm MK-801 is indicated with the grey bar

d- Summary plot showing EPSP reduction in the silent pathway. EPSPs were normalized to their baseline amplitude. The reduction was more substantial when the postsynaptic cell was filled with the KMS-based internal solution.

Data are presented as mean ± SEM; ns: $p > 0.05$, *$p < 0.05$.

5.4. Discussion

In this chapter, I have reported a mechanism underlying the reduction in the efficacy of astrocytic glutamate transporters that occurs during physiological synaptic transmission. Below, I discuss the relevance of my findings to the current literature, their impact on physiological signalling in the hippocampus, and clarify the importance of the methodological approach used for isolating the glutamate transporter current.

5.4.1. Critical methodological limitations in recording glutamate transporter currents from astrocytes

It is well-established that high-affinity astrocytic glutamate transporters rapidly take up almost all of the glutamate released during synaptic transmission (Danbolt, 2001; Kim et al., 2011). Their complex stoichiometry allows the amount of glutamate released to be estimated by measuring the amplitude of evoked inward currents in astrocytes, as suggested by earlier studies (Bergles and Jahr, 1997; Diamond et al., 1998). Some studies, in addition to blocking transporters, have introduced a block of K^+ channels either with bulk $CdCl_2$ or $BaCl_2$ application (Meeks and Mennerick, 2007; Afzalov et al., 2013; Armbruster et al., 2016; Dvorzhak et al., 2016). The crucial property of glutamate transporters is that their operation is strongly voltage-dependent (Wadiche et al., 1995; Grewer et al., 2000). As I showed here in section 5.3.6 and as also reflected in a paper published by our laboratory (Lebedeva et al., 2018), blocking astrocytic K^+ conductance leads to profound depolarisation of the cells, making them insensitive to further accumulation of extracellular $[K^+]$. Thus, Ba^{2+} or any other K^+ channel blockers could not be used to investigate the relationship between physiological K^+ accumulation and glutamate uptake provided by transporters. However, alternative approach using glutamate transporter inhibitor - TBOA allowed recording of the K^+ current; and isolate

glutamate current with post-hoc subtraction (Shimamoto et al., 1998; Jabaudon et al., 1999).

As established in the chapter, the slowing down of the astrocytic glutamate transporter rate is mediated by K^+ efflux through postsynaptic NMDA receptors. Hence, the presence of functioning NMDA receptors is essential for triggering this mechanism. This factor presents another methodological issue. An early study demonstrating that synaptic activation evokes an astrocytic glutamate transporter current was performed by Bergles and Jahr (1997). To eliminate the postsynaptic current they used an antagonist of NMDA receptors that resulted in a restriction of extracellular [K^+] accumulation. Later, the same authors also attempted to evaluate the glutamate transporter time course under physiological stimulation, but the recording was also conducted during blockade of ionotropic glutamate receptors, including NMDA receptors (Diamond, 2005). Experiments under the same experimental conditions reveal that enhancing the stimulation frequency does not affect the transporter decay time (Diamond and Jahr, 2000); this has also been confirmed in the cortex (Capuani et al., 2016; Rimmele et al., 2017). Importantly, restriction of physiological [K^+] accumulation in the synaptic cleft would not reflect the impact of a voltage-dependent component on glutamate transporters operation. In this chapter, I demonstrated that recording the astrocytic glutamate transporter current with TBOA application but without ionotropic receptor antagonists (in particular NMDA receptor antagonists) is a valid technique for providing information about pre- and post-synaptic activity during neuronal firing. Such an approach allowed me to demonstrate an activity-dependent facilitation of glutamate transporter current evoked with repetitive stimulation of SC.

5.4.2. Activity-dependent facilitation of astrocytic glutamate transporter currents is underlined by NMDA receptors-mediated K^+ efflux

Probably one of the most exciting findings from this chapter is that both the amplitude and the decay time of synaptically induced glutamate currents in hippocampal astrocytes increase in an activity-dependent manner. Glutamate transporter current amplitude increased with each following stimulus in the absence of ionotropic receptor antagonists, suggesting that more glutamate was released from presynaptic terminals and consequently sensed by astrocytic transporters. This finding is in line with the study of Shih et al. (2013), which showed that K^+ accumulation through NMDA receptors could contribute to the enhanced neurotransmitter release. Indeed, in my experiments, glutamate transporter current potentiation was suppressed by blockade of postsynaptic NMDA receptors, which serve as a major source of K^+ efflux. Application of TBOA allowed me to estimate the decay time for glutamate transporters. The increase in the decay time was also abolished by blockade of NMDA receptors. Interestingly, the decay time of the glutamate transporter current, evoked by a single stimulation delivered to the SC does not change upon exposure to different receptor antagonists or even in recordings from knockout animals. Thus, astrocytic glutamate transporters are capable of translocating glutamate within the 5–6 ms range, regardless of the level of K^+ accumulation through ionotropic receptors. Below, I compare the glutamate transporter decay time results obtained in this chapter to established findings, considering the methodological limitations mentioned and the variability of cell types used for these experiments.

The glutamate transporter current decay time recorded from HEK cells at room temperature was estimated to be around 5–10 ms (Grewer et al., 2000). Although astrocytic transporter capacity was shown to be diminished at temperatures below physiological levels, transporters only show a tendency to be overwhelmed with 4 or more stimuli (Diamond and Jahr, 2000). This allows me to conclude that the decay time of recorded in this chapter astrocytic

glutamate transporter current evoked with single stimulation fits well with established findings. More recent experiments recording the astrocytic glutamate transporter current in physiologically-relevant conditions and applying TBOA have allowed the current decay time to be evaluated, which is also within the range of 6–6.5 ms (Armbruster et al., 2016). Thus, the decay time reported in this chapter evoked by a single stimulation of the SC is consistent with the literature. Several attempts were made to evaluate astrocytic transporter efficiency during repetitive stimulation. However, recordings in earlier studies were routinely performed in the presence of NMDA, AMPA, and $GABA_A$ receptors antagonists in the perfusion system (Diamond and Jahr, 2000; Meeks and Mennerick, 2007; Capuani et al., 2016). Blocking postsynaptic ionotropic receptors restrict $[K^+]$ accumulation in the synaptic cleft. Thus, the above studies reported that transporter current decay time evoked by repetitive stimulation does not significantly change from the current decay time induced by a single stimulation, and stays within the 5–10 ms range. When I used antagonists of ionotropic receptors to identify the major source of K^+ during repetitive stimulation of the SC, the recorded glutamate transporter current decay time was also within the 7–13 ms range. Hence, a part of the results presented in this chapter is in agreement with the literature. Moreover, the proposed mechanism for regulating transporter efficiency through NMDA receptor-mediated K^+ accumulation has not been previously reported.

5.4.3. Can astrocytic glutamate transporters be overwhelmed?

It has been previously shown by Diamond and Jahr (2000) that astrocytic glutamate transporters are not overwhelmed during high-frequency stimulation (Diamond and Jahr, 2000). However, their blockade of NMDA receptors did not allow them to investigate the impact of accumulated K^+ in the cleft. Nonetheless, the proposed mechanism involves K^+ efflux from postsynaptic NMDA receptors, with further astrocytic membrane depolarisation. In this

chapter, I tested the hypothesis that stronger synaptic stimulation would recruit more NMDA receptors, leading to a greater K^+ accumulation. As a result, transporter efficiency for glutamate uptake would be reduced. Although I adjusted the stimulation strength to evoke two-fold greater currents, I did not find any difference in the glutamate transporter time course. This effect might be explained by the fact that stronger stimuli simply recruit more synapses: this would not increase local hotspots of extracellular K^+ accumulation near individual connections. In such cases, glutamate transporters effectively clear extracellular glutamate in the hippocampal *stratum radiatum* region either with a weak or with a strong stimulation of the SC. Among studies investigating the ability of glutamate transporters to translocate glutamate in different conditions, I found only one showing an activity-induced slow-down of glutamate uptake and an extended glutamate dwell-time in the synaptic cleft (Armbruster et al., 2016). This recent study was performed in cortical astrocytes, under the AMPA and NMDA receptor blockade, along with bulk $BaCl_2$ application (to block astrocytic K^+ conductance). Increased stimulation, from a single to 10 stimuli at 100 Hz, produced a significant increase in glutamate transporter current decay time from 10 to 20 ms. These results might be explained either by the different properties of astrocytes in the cortex compared to the hippocampus or by using higher frequency and longer-lasting stimulation. An increase in the number or frequency of stimuli might underlie the more profound effect on astrocytic membrane potential (even though astrocytes would already be depolarised by $BaCl_2$). Recording glutamate transporter current during more frequent or prolonged stimulation might shed light on astrocytic transporter efficiency in the hippocampus.

5.4.4. Astrocytic depolarisation underlies changes in the decay time of glutamate transporters

One finding from this chapter suggests that it is astrocytic membrane depolarisation, rather than the K^+ gradient, that underlies the suppression of glutamate uptake. We showed that direct depolarisation of an astrocyte on its own mimicked the effect of K^+ elevation on the suppression of glutamate transporter currents. Depression of both the glutamate transporter current amplitude and the decay time was abolished when cells were held at a constant membrane potential (-85 mV). In contrast to our findings, glutamate application to HEK cells expressing GLT-1 voltage-clamped at -80 mV revealed that exposure of the cells to 8 mM K^+ caused a small reduction in both the amplitude and the decay time of recorded glutamate currents (Rimmele et al., 2017). This finding suggests that the glutamate transporter rate is not entirely determined by changes in the resting membrane potential. A potential explanation might be hidden in the operation of the transporter cycle. Glutamate translocation by transporters is performed in two distinct half-cycles. The second half-cycle ensures the reorientation of transporter residues back to the extracellular space and anticipates the start of the next cycle. Kanner (2006) proposed that an elevated level of extracellular K^+ might increase the chance that transporters stay in the inward-facing conformation and thus limit glutamate uptake.

5.4.5. K^+ efflux from the postsynaptic terminal extends glutamate dwell-time in the cleft

One hypothesis for the efficient regulation of glutamate concentration in the cleft includes rapid glutamate binding to transporters (Diamond and Jahr, 1997). Steady-state experiments have revealed that glutamate binding to the transporter is more rapid (around $1–2 \times 10^7\ M^{-1}s^{-1}$) than its translocation phase.

Astrocytic processes facing the synaptic cleft have been shown to express a large number of glutamate transporters — up to 8500 per μm^2 (Lehre and Danbolt, 1998; Otis and Jahr, 1998), which are capable of rapid glutamate binding. In such circumstances, it would require tens to hundreds of microseconds to buffer the released glutamate (Clements et al., 1992). Furthermore, according to Grewer et al. (2000), 500 µs are required for glutamate to dissociate from the transporter-binding site, which is 10 times faster than a complete translocation cycle. All of the above implies a higher chance that glutamate might bind to and dissociate from transporters several times before it is translocated or diffuses away. However, it is still possible to speculate about which process (buffering or translocation) predominantly takes place under physiological conditions. The ambiguity arises from the estimated transporter rates. The majority of these studies are based on steady-state kinetics of transporters obtained at room temperature and do not account for the sensitivity of transporters to temperature changes (Diamond and Jahr, 2000; Wadiche and Kavanaugh, 2018). Thus, glutamate translocation closer to physiological temperatures might be preferred. Here, considering the limitation of glutamate transporter current for representing the buffering of glutamate, we performed recordings from postsynaptic neurons and estimated glutamate dwell-time by analysing EPSP decay time. An activity-dependent prolongation of EPSPs was observed when the postsynaptic cell contained a physiological concentration of K^+, but not when the K^+ was replaced with $NMDG^+$ ions. This suggests that K^+ efflux from the postsynaptic neuron extends the glutamate time course in the synaptic cleft. Furthermore, direct acquisition of the glutamate dwell-time with a glutamate sensor revealed a decrease in decay time of glutamate transients when K^+ in the postsynaptic cell was replaced with $NMDG^+$. This confirmed that glutamate is present for a longer time in the synaptic cleft only when K^+ efflux from postsynaptic NMDA receptors occurs. Thus, this suggests that glutamate translocation does indeed contribute to activity-dependent changes in decay time during synaptic transmission.

5.4.6. Physiological relevance

The findings reported in this chapter suggest that during synaptic transmission, NMDA receptor-mediated K^+ accumulation depolarises the astrocytic membrane and suppresses the rate of glutamate uptake by astrocytic glutamate transporters. This mechanism underlies the extended glutamate dwell-time in the synaptic cleft. Using stimulation of independent afferent pathways, we demonstrated that glutamate spillover is more profound when NMDA receptor-mediated K^+ efflux occurs. Previous simulation studies suggest that K^+ can elevate up to 5 mM in the synaptic cleft during single EPSC (Shih et al., 2013a). However, it remains unknown to what extend perisynaptic astrocytic processes could be depolarised under physiological transmission. It is a challenging task and cannot be directly measured, because astrocytic processes are beyond optical resolution for voltage imaging and cannot be accessed with electrode-based techniques. In this chapter, we found that elevation of extracellular K^+ to 10 mM lead to -65.2 ± 4.41 mV astrocytic depolarisation by which significantly increases the decay time of uIGluT.

What could be the physiological role of this phenomenon? The precise maintenance of glutamate concentration by glutamate transporters is known to underlie several physiological phenomena. A reduced glutamate uptake rate might boost glutamate spillover (Rusakov and Kullmann, 1998) and not only activate receptors in neighbouring synapses, but also mobilise extracellular NMDA receptors, producing a lower LTD threshold (Wong et al., 2007). Moreover, downregulation of astrocytic glutamate transporters has been shown to increase the magnitude of mGluR–dependent LTD (Brasnjo and Otis, 2001) and impair LTP via chronic NMDA receptor activation (Katagiri et al., 2001). On the contrary, a lower amount of available glutamate, resulting from the upregulation of glutamate transporters, limits the activation of various receptors. For example, reducing the activation of presynaptic mGluRs prevents LTD, whereas sufficiently restricting the activation of kainite receptors decreases the magnitude of LTP (Omrani et al., 2009). Moreover, LTP itself changes the ability of a synapse to release K^+ to the extrasynaptic space.

Although the increased number of AMPA receptors after LTP do not contribute significantly to K^+ efflux due to their fast inactivation, they can facilitate activation of NMDA receptors by removing their voltage-dependent block. Therefore, LTP not only increases the quantal efficiency of the synapse, but also promotes K^+-dependent facilitation of glutamate release and spillover at the synapse. K^+-dependent facilitation of presynaptic glutamate release after LTP could be linked to the putative perisynaptic mechanism of LTP.

Recent studies have drawn attention to local signalling mediated by changes in ionic concentrations in the synaptic cleft and in the perisynaptic space. Since the volumes of these spaces are minuscule, the concentration changes could be profound. The K^+ clearance mechanisms of astrocytes can, therefore, serve as an essential factor in regulating mechanisms of synaptic plasticity, hence learning and memory.

5.5. Conclusion

The overall finding from this chapter is that during synaptic transmission, K^+ efflux from postsynaptic NMDA receptors leads to profound $[K^+]$ accumulation in the synaptic cleft. This K^+ build-up ensures astrocytic depolarisation and slows down glutamate uptake by astrocytic glutamate transporters. This mechanism boosts extrasynaptic glutamate escape, or spillover, which affects accurate signal transduction in brain circuits. Our finding emphasizes the physiological importance of changes in ionic concentrations in the synaptic cleft and perisynaptic space.

Chapter 6

Functional properties of astrocytes with genetic upregulation of Kir4.1 channel expression

6.1. Introduction

The inward rectifying K^+ channels of 4.1 subfamily keep the astrocyte resting membrane potential close to K^+ equilibrium potential (Kofuji et al., 2000; Neusch et al., 2001; Olsen et al., 2006). A loss of functionality, or a reduction of astrocytic Kir4.1 expression has been found in various neurodegenerative disorders, including hippocampal sclerosis (Kivi et al., 2000), Huntington's disease (Dvorzhak et al., 2016), and epilepsy (Steinhäuser et al., 2012). Genetic deletion of Kir4.1 results in severe pathology and lethal phenotype in early postnatal development of mice (Neusch et al., 2001). Strikingly, mice with conditional knock-out of Kir4.1 restricted to astrocytes are characterised by ataxia, seizures and early lethality, confirming the importance of this subtype of K^+ channels (Chever et al., 2010). Lack of Kir4.1 expression in astrocytes leads to profound membrane depolarisation associated with impaired K^+ buffering and decrease of glutamate uptake (Casper et al., 2007). These factors result in a decrease of spontaneous neuronal activity and an enhancement of synaptic potentiation. It has been shown that these effects can be rescued by restoring Kir4.1 channel expression levels, prolonging the survival rate of mice and pointing out that they can serve as a potential target for aforementioned diseases treatment (Tong et al., 2014; Dvorzhak et al., 2016). Thus, astrocytic Kir4.1 channels represent an important component ensuring physiological conditions for synaptic transmission, through 1) maintaining efficient glutamate uptake (by determining resting membrane potential); and 2) regulating release probability from presynaptic terminal (by maintaining extracellular $[K^+]$ levels) (Casper et al., 2007). However, these

properties of Kir4.1 channels in astrocytes were not quantified with necessary precision to evaluate their effects on synaptic transmission.

Since the loss or deletion of Kir4.1 channels enormously affects astrocytic maturation and brain development in general, it cannot serve as an accurate tool to quantify Kir4.1 channels impact on glutamate transporters efficiency. Therefore, I used a contrasting approach — the genetic upregulation of Kir4.1 expression in astrocytes. To further pursue this idea, here I test a methodology for over-expressing Kir4.1 channels in astrocytes, followed by a characterisation of cells properties.

6.2. Methods

To achieve genetic upregulation of Kir4.1 channel expression in astrocytes, I used an AAV selected from the 9 serotypes under the gfaABC1D promoter, which preferentially targets astrocytes and delivers tdTomato-tagged Kir4.1 channels (AAV9 pZac2.1-gfaABC1Dpromoter > tdTomato: rKcnj10). Injections of AAV were performed to P0–3 neonatal pups in a volume not exceeding 2.5 µL per hemisphere. The virus was injected to a right lateral ventricle (2/5 of the distance from the lambda suture to each eye) using a Hamilton needle. Acute hippocampal slices were prepared 2–3 weeks after AAV injection. For control experiments, I used littermates injected with the same amount of virus-free ACSF solution. Acute hippocampal slices were prepared as outlined in the methods section. To prevent photobleaching of the tdTomato fluorescent marker, I restricted slice exposure to light and kept them in the darkroom during the incubation period.

CA1 *stratum radiatum* astrocytes with upregulated Kir4.1 channel expression were identified using Femto-2D system in two-photon mode by tdTomato fluorescence (Figure 6.1a—c). Then by switching from two-photon to transparent light mode, I identified the soma of the cell and patch-clamped it. Additional confirmation of Kir4.1 channel over-expression was performed after establishing a whole-cell configuration. Occasionally, I patched

astrocytes without visual fluorescence that were located next to astrocytes with Kir4.1 channel over-expression. If these astrocytes form functional gap-junction connections with Kir4.1 over-expressing astrocytes (which could be identified by the diffusion of morphological tracer dye through gap-junctions), then they also were used for analysis and were termed ‘cells forming gap-junction connections to an astrocyte with upregulation of Kir4.1 channels’ (GJ to Kir4.1). Whole-cell recordings of astrocytes were performed with a KMS-based internal solution. In order to characterise [Ca^{2+}], the baseline internal solution was supplemented with Ca^{2+}-sensitive OGB-1 dye. Sufficient time was allowed for dye diffusion to gap-junction connected astrocytes and for equilibration before recordings. The [Ca^{2+}] baseline signal from 2-3 astrocytes was recorded in frame scan mode, which was performed over the cell soma at 2 Hz. In order to isolate the Kir current, the extracellular Kir channel blocker $BaCl_2$ (200 µM) was added to the perfusion system. The *I-V* relationship was measured before and during extracellular application of $BaCl_2$, and using post-hoc point-by-point subtraction, the Ba^{2+}-sensitive K^+ component was isolated.

6.3. Results

6.3.1. Hippocampal astrocytes express Kir4.1 channels conjugated with the tdTomato fluorescent marker

The custom-designed virus was aimed to enhance Kir4.1 channel expression in astrocytes. The virus was conjugated with the fluorescent marker tdTomato to able easy visualise expressing cells with fluorescence

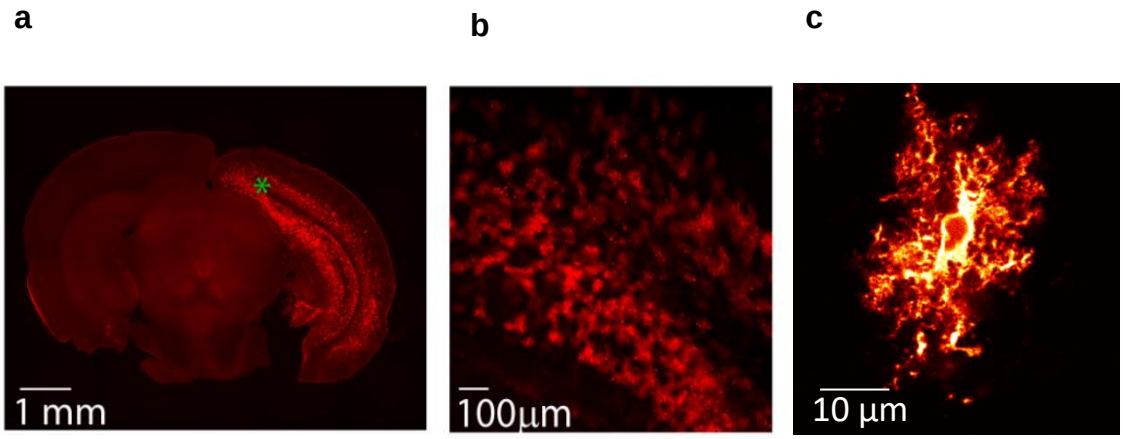

Figure 6.1 Astrocytes show tdTomato fluorescence associated with upregulated levels of Kir4.1 channels

a- Whole-brain coronal slice obtained from a P21 mouse injected with a virus that enhances expression of Kir4.1 channels. This virus is conjugated with a tdTomato fluorescent marker
b- Zoomed area from (a) (marked with the star), confirming virus expression in the hippocampus
c- Two-photon tdTomato fluorescence signal recorded from an individual astrocyte in the CA1 *stratum radiatum* region of the hippocampus.

I performed viral injections to the neonatal animals. Dr Rob Wykes performed slicing and imaging.

microscopy. The injection of the Kir4.1 virus into neonatal mice did not change survival rates and allowed me to perform experiments using P21–28 animals. Then I validated whether the injection of this virus would have significant tdTomato fluorescence level in astrocytes. A strong tdTomato fluorescence signal was detected from different brain regions, including the hippocampus (Figure 6.1a–b). Expression of this virus was restricted to astrocytes and allowed to clearly distinguish astrocytic somata, main branches, and small protrusions (Figure 6.1c).

6.3.2. Genetic upregulation of Kir4.1 channel expression in astrocytes enhances Ba^{2+}-sensitive currents

To confirm that expression of the virus resulted in successful delivery of functional Kir4.1 channels, I documented electrophysiological properties of hippocampal astrocytes (Figure 6.2a). Since Kir4.1 channels are the predominant channel subtype expressed in astrocytes, the one that determines the astrocytic resting membrane potential near K^+ equilibrium potential (EK), I started by characterising cells' resting membrane potential (Vm). Upregulation of Kir4.1 channels did not produce a significant change in resting membrane potential (-78.78 ± 1.25 mV; n = 13; Figure 6.2b) compared to control astrocytes, recorded from WT animals injected with virus-free ACSF solution (-80.44 ± 2.61 mV, n = 5; $p > 0.05$, two-sample t-test; Figure 6.2b). TdTomato-negative astrocytes located in close proximity to Kir4.1 over-expressing astrocytes and connected with them via functional gap-junction connections also did not show any changes to their resting membrane potential (-79.34 ± 1.79 mV, n = 5; $p > 0.05$ for the difference with the WT group, two-sample t-test; Figure 6.2b). Application of $BaCl_2$ in low-concentration to the perfusion system preferentially blocked Kir and produced significant depolarisation in all recorded astrocytes. Exposure to $BaCl_2$ produced a significant depolarisation of WT astrocytes to -69.88 ± 2.43 mV (n = 5; $p < 0.05$; paired t-test; Figure 6.2b). Astrocytes with upregulated Kir4.1 expression level also showed a shift in there resting membrane potential to -65.41 ± 2.70 mV (n = 13; $p < 0.001$; paired t-test; Figure 6.2b) when $BaCl_2$ was applied. Likewise, GJ-connected to Kir4.1 over-expressing astrocytes also were depolarised to -67.6 ± 3.22 mV (n = 5; $p < 0.05$; paired t-test; Figure 6.2b). To compare in which group application of $BaCl_2$ produces more substantial depolarisation I calculated the difference between resting membrane potential during $BaCl_2$ applications, and in control conditions.

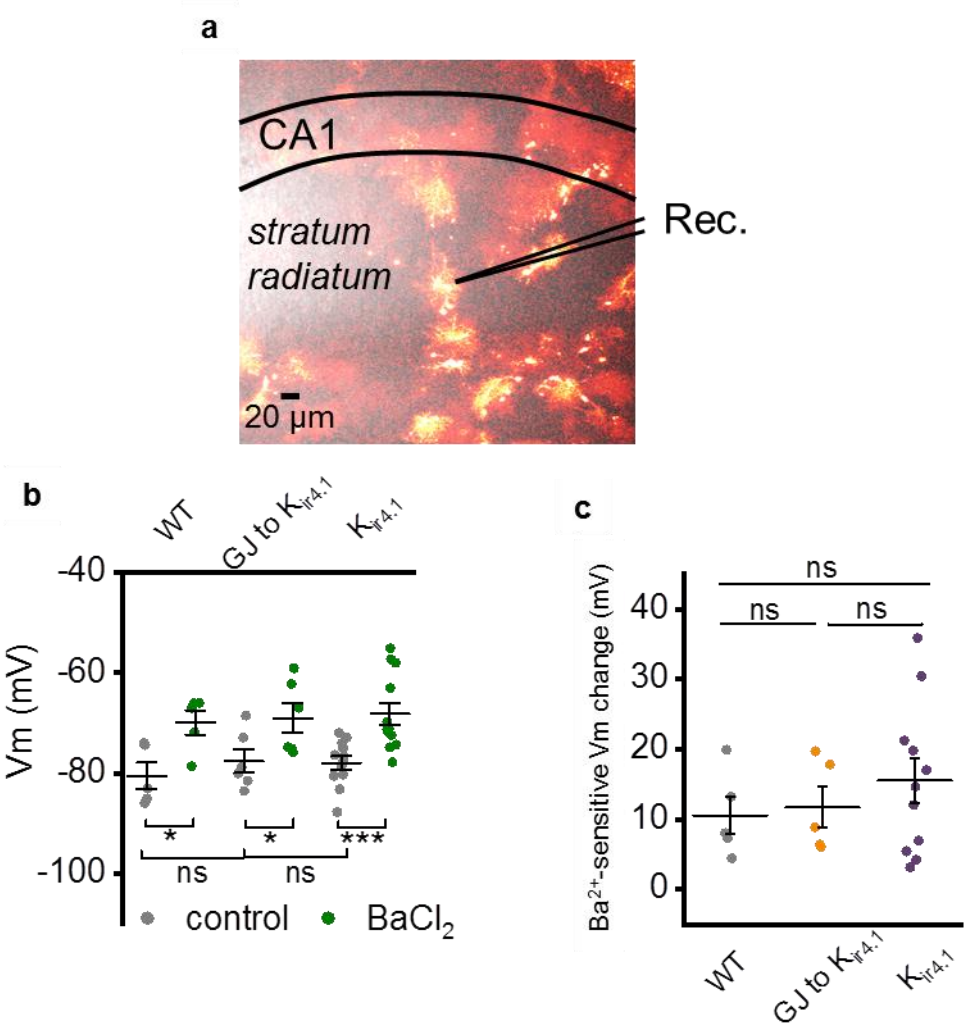

Figure 6.2 Upregulation of Kir4.1 channel expression does not affect astrocyte resting membrane potential

a- An acute hippocampal slice with Kir4.1 over-expressing astrocytes identified by their tdTomato fluorescence signal. Recording of electrophysiological activity was performed in whole-cell mode through a patch pipette

b- Upregulation of Kir4.1 channels did not affect the astrocytic resting membrane potential. Introduction of a low concentration of $BaCl_2$ to the perfusion system preferentially blocked Kir channels. This demonstrates the impact of Kir in setting the resting membrane potential

c- Application of $BaCl_2$ produced astrocytic depolarisation, with a more substantial but non-significant drop of membrane potential in Kir4.1-over-expressing astrocytes.

Data are presented as mean ± SEM; ns: $p > 0.05$, *$p < 0.05$, **$p < 0.01$, and ***$p < 0.001$.

TdTomato-negative astrocytes located in close proximity to Kir4.1 over-expressing astrocytes showed a greater change in the resting membrane potential 11.74 ± 2.97 mV (n = 5) compared to the WT group 10.56 ± 2.73 mV (n = 5), however it did not reach significant level ($p > 0.05$; two-sample t-test; Figure 6.2c). Changes of recorded resting membrane potential from the Kir4.1 channels over-expressing astrocytes also demonstrated a trend to increase, by 15.49 ± 3.24 mV, when compared to the WT group (n = 11; $p > 0.05$; two-sample t-test; Figure 6.2c).

The delivery of additional Kir4.1 channels to astrocytes did not affect input resistance (Rin) (24.79 ± 2.72 MOhm, n = 15) when compared to the WT group (26.05 ± 2.38 MOhm, n = 8; $p > 0.05$, two-sample t-test; Figure 6.3a). TdTomato-negative astrocytes located in close proximity to Kir4.1 over-expressing astrocytes showed a similar range of values for input resistance (19.72 ± 2.89 MOhm, n = 7; $p > 0.05$ for the difference with the WT group, two-sample t-test; Figure 6.3a). As anticipated, application of $BaCl_2$ significantly increased input resistance in all recorded astrocytes. The WT group demonstrated increase in their input resistance to 32.20 ± 2.42 MOhm (n = 8, $p < 0.01$; paired t-test; Figure 6.3a), while tdTomato-negative astrocytes GJ-connected to Kir4.1 over-expressing cells also showed a significant increase in the input resistance to 30.02 ± 3.48 MOhm (n = 14, $p < 0.05$; paired t-test; Figure 6.3a). Among all groups, the most profound increase in the input resistance was measured for Kir4.1 over-expressing astrocytes (38.07 ± 2.44 MOhm, n = 15, $p < 0.0001$; paired t-test; Figure 6.3a). To evaluate in which group application of $BaCl_2$ had more of an effect, I measured changes in the input resistance upon exposure to $BaCl_2$. As shown in Figure 6.3b the most profound Ba^{2+}-mediated increase of the input resistance was observed between the WT group (5.96 ± 1.29 MOhm, n = 8) and Kir4.1 over-expressing astrocytes (14.57 ± 1.59 MOhm, n = 15; $p < 0.01$; two-sample t-test). Next, to test whether Kir4.1 over-expressing astrocytes display enhanced K^+ currents, I measured the *I-V* relationship before (Figure 6.4a–b) and during application of $BaCl_2$. The post-hoc subtraction of the traces recorded

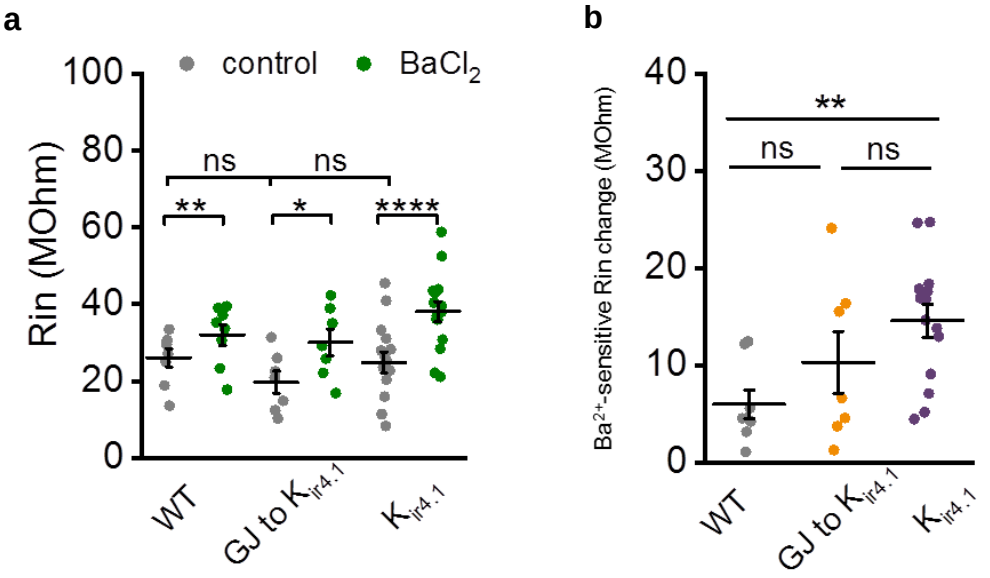

Figure 6.3 Upregulation of Kir4.1 channel expression increases Ba^{2+}-sensitive input resistance in astrocytes

a- Upregulation of Kir4.1 channel expression did not affect astrocytic input resistance in any of the conditions. Introduction of $BaCl_2$ to the perfusion system blocked Kir channels and increased the input resistance (Rin)

b- Application of $BaCl_2$ produced a significant increase in input resistance in Kir4.1 over-expressing astrocytes.

Data are presented as mean ± SEM; ns: $p > 0.05$, *$p < 0.05$, **$p < 0.01$, and ***$p < 0.001$.

with $BaCl_2$ from those in control conditions enables isolation of the Ba^{2+}-sensitive K^+ currents (Figure 6.4c–d). Kir4.1 over-expressing astrocytes demonstrated a significant enhancement of K^+ currents at -120 mV (-0.88 ± 0.24 nA, n = 12) compared to WT astrocytes (-0.37 ± 0.1 nA, n = 7; $p < 0.05$, two-sample t-test; Figure 6.4e).

6.3.3. Upregulation of Kir4.1 channel in astrocytes does not affect the baseline level of Ca^{2+}

Although upregulation of the Kir4.1 channel did not produce changes in the resting membrane potential, it might affect activation of voltage-dependent Na^+ or Ca^{2+} channels, causing a rise in [Ca^{2+}] (Duffy and MacVicar, 1994). Here, I tested whether the upregulation of Kir4.1 channel expression affects the baseline level of [Ca^{2+}] in astrocytes. To achieve this, Kir4.1 over-expressing astrocytes were loaded with Ca^{2+}-sensitive dye (OGB-1) (Figure 6.5a). Recording of the baseline [Ca^{2+}] was then performed from astrocytes GJ-connected to the patched cell, both with and without tdTomato fluorescence. In this configuration, dye diffusion to neighbouring astrocytes would demonstrate that Kir4.1 over-expressing astrocytes form functional gap-junction connections with neighbouring astrocytes. This might be critical for spatial K^+ buffering. The baseline [Ca^{2+}] recorded from gap-junction astrocytes (81.48 ± 3.56 nM, n = 13; Figure 6.5b) was significantly lower than that of patched astrocytes (128.49 ± 8.76 nM, n = 6; $p < 0.01$, two-sample t-test; Figure 6.5b). This effect might be caused by pipette dialysis, as previously reported in Zheng et al., 2015. Probably the most intriguing finding is that the baseline [Ca^{2+}] of Kir4.1 over-expressing astrocytes (79.63 ± 4.98 nM, n = 8) did not significantly differ from either WT astrocytes (81.48 ± 3.56 nM, n = 13; $p > 0.05$; two-sample t-test; Figure 6.5b) or tdTomato-negative astrocytes GJ-connected to Kir4.1 over-expressing cells (76.01 ± 4.55 nM, n = 21; > 0.05; two-sample t-test; Figure 6.5b). This suggests that genetic delivery of additional Kir4.1 channels to astrocytes does not cause changes in the baseline [Ca^{2+}].

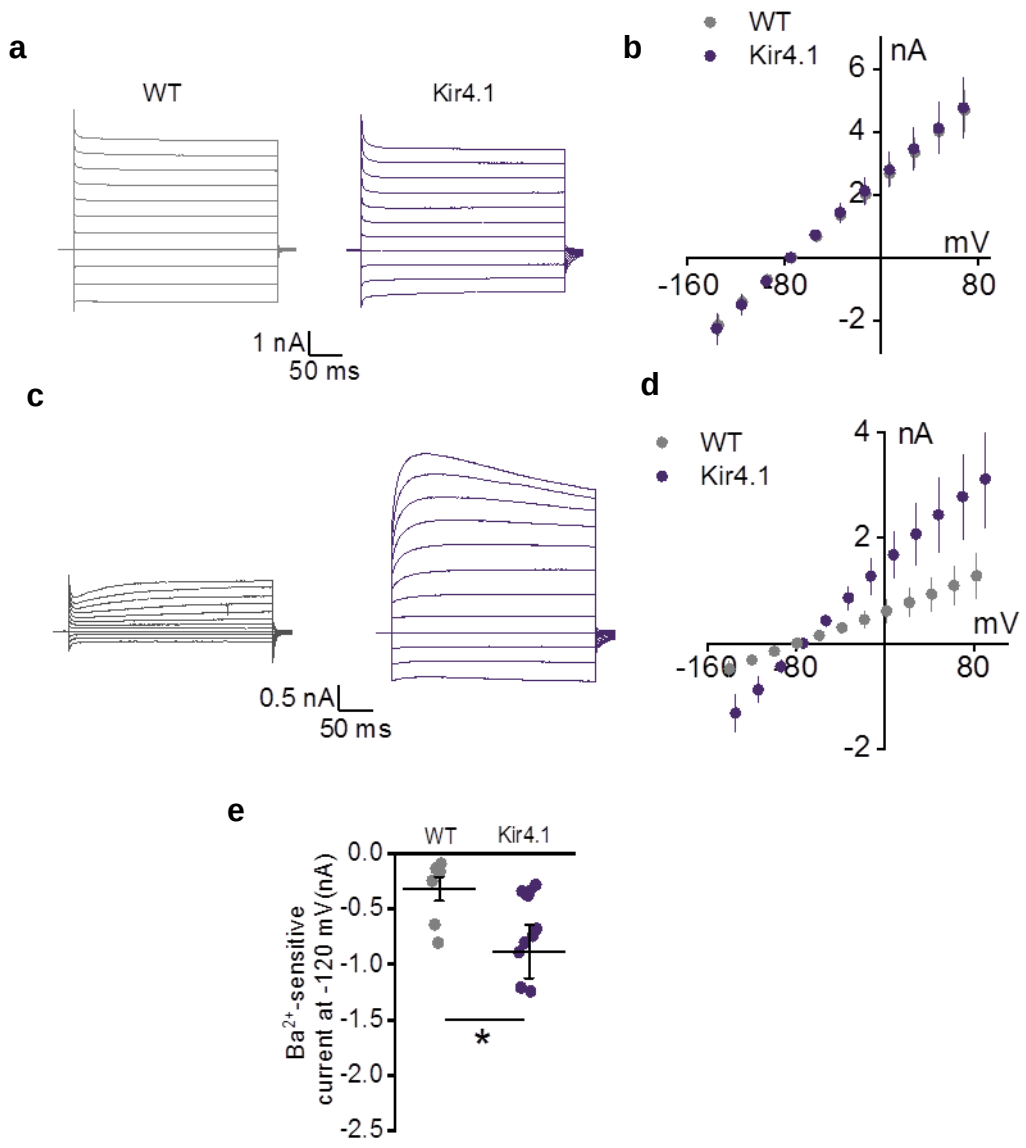

Figure 6.4 Upregulation of Kir4.1 channel expression in astrocytes enhances Ba^{2+}-sensitive currents

a- Sample traces representing current changes for step voltage injection in WT and Kir4 over-expressing astrocytes
b- Summary plot showing *I-V* plot for traces in (a)
c- Ba^{2+}-sensitive sample traces representing current changes for step voltage injection in WT and Kir4.1 over-expressing astrocytes
d- Ba^{2+}-sensitive *I-V* plot showing that upregulation of Kir4.1 channels increases the amplitude of K^+ currents
e- Ba^{2+}-sensitive current for WT and Kir4.1 over-expressing astrocytes at -120 mV.

Data are presented as mean ± SEM; *$p < 0.05$.

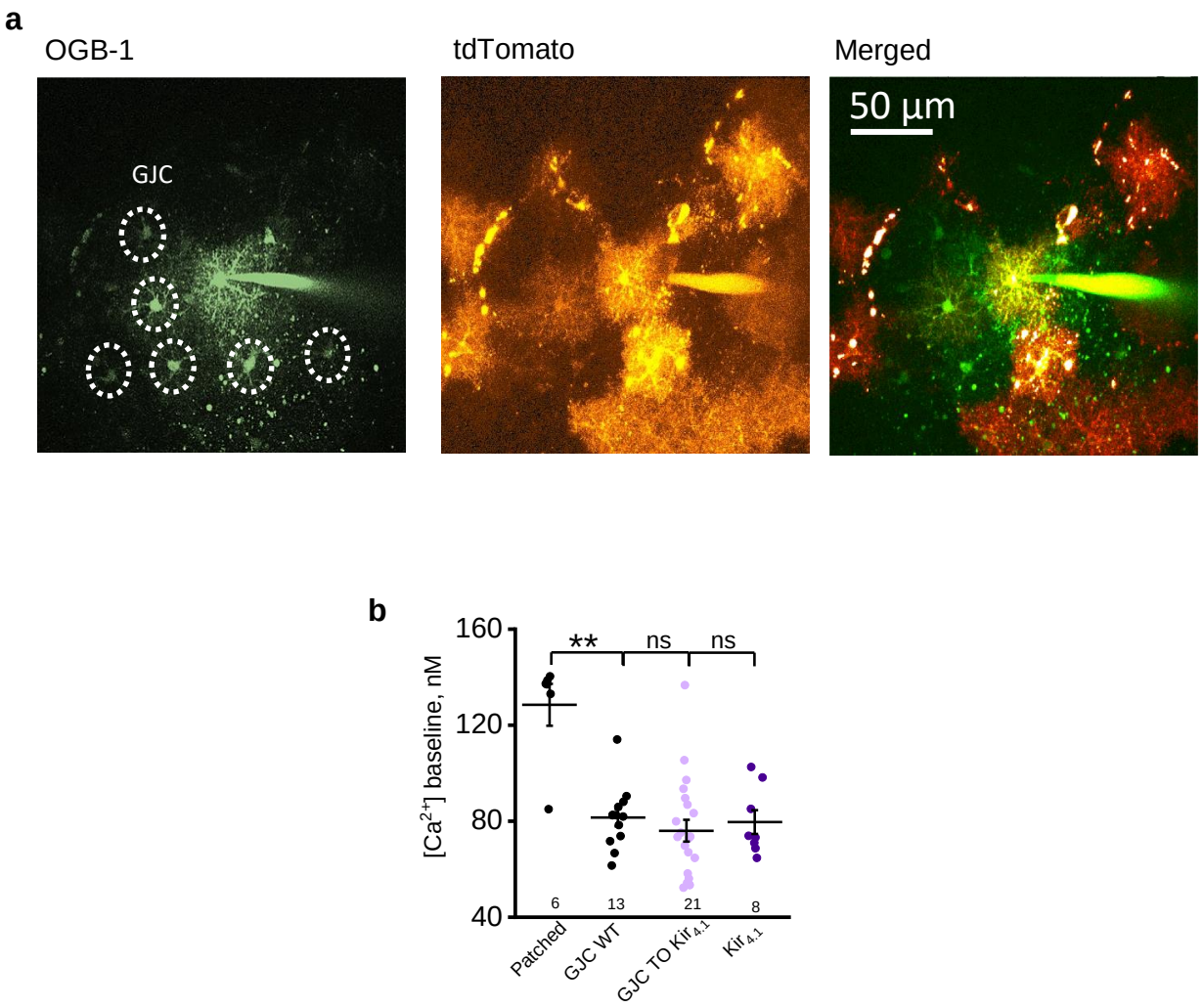

Figure 6.5 Upregulation of Kir4.1 channel expression in astrocytes does not affect the baseline [Ca^{2+}]

a- Examples of astrocytes (dotted circles) loaded with OGB-1 the pipette into Kir4.1 over-expressing astrocytes
b- Upregulation of Kir4.1 channel expression did not affect the astrocytic baseline [Ca^{2+}].

Data are presented as mean ± SEM; ns: $p > 0.05$, **$p < 0.01$

6.4. Discussion

6.4.1. Observations of Kir4.1 over-expressing astrocytes versus previously reported findings

The most noticeable result from this chapter is that upregulation of Kir4.1 channel expression in astrocytes did increase K^+ currents through the membrane, but left other electrophysiological properties of the cells, or the baseline [Ca^{2+}], unaffected. The notable widespread expression of Kir4.1 in glial cells, as confirmed by several groups, provides supportive evidence for a special role for this channel subtype in shaping the physiological characteristics of glial cells (Neusch et al., 2005). Studies performed on animals lacking functional Kir4.1 channels have established that Kir channels in astrocytes are essential for setting the resting membrane potential and are likely to be involved in extracellular K^+ clearing up with further release back to the extracellular space (Neusch et al., 2005; Casper et al., 2007; Harrison et al., 2007). It is not surprising that abnormal functioning of Kir4.1 channels is associated with a wide range of pathologies (Kivi et al., 2000; Steinhäuser et al., 2012; Dvorzhak et al., 2016). An excess of extracellular K^+ following brain injury has been attributed to a decrease in astrocytic Kir conductance (Bastide et al., 1999). Moreover, tissue obtained from epileptic patients shows a significant lack of inward-rectifying currents in astrocytes (Bordey and Sontheimer, 1998; Hinterkeuser et al., 2000) and disrupted K^+ buffering (Steinhäuser and Seifert, 2002). Additionally, astrocytes from several mouse models of a neurological disease show a dramatic reduction in both the expression level and functional profile of Kir4.1 channels. As reported earlier an HD-induced deficit in Q175 mice was associated with Kir4.1 functional loss and an elevated level of extracellular K^+; this could be rescued by viral delivery of this channel subtype to astrocytes. Restoring the Kir4.1 channel expression level also rescues the *I-V* relationship, the resting membrane potential, and K^+ currents (Tong et al., 2014). In glioma cell cultures, restoring Kir4.1 leads to membrane hyperpolarisation from -50 to -80 mV and prevents cell growth

(Olsen and Sontheimer, 2008). The broad diversity of studies investigating Kir4.1 in astrocytes allow me to compare the results obtained in this chapter with regard to Ba^{2+}-sensitive electrophysiological properties to those already obtained. In general, as recorded in this chapter, the resting membrane potential and input resistance from astrocytes lay within physiological range for hippocampal astrocytes and were in line with multiple studies using animals of the same age range. In particular, a recent study restoring Kir4.1 channel activity reported an astrocytic resting membrane potential of around -76 mV (Tong et al., 2012). A low concentration of $BaCl_2$ was shown to depolarise astrocytes in acute brain slices from -80 mV to -60 mV and to produce a two-fold increase in input resistance (Dvorzhak et al., 2016). Here, I obtained a similar membrane potential change for the WT group from -80 mV to -69 mV, which was associated with a 1.5-fold input resistance enhancement. Although I could identify Kir4.1 over-expressing astrocytes using the tdTomato fluorescence signal, I could not control the level of Kir4.1 channels expression. This potentially introduces variability into the recorded data. Surprisingly, the Kir4.1 over-expressing astrocytes recorded in this chapter showed no significant change in rest membrane potential or input resistance. These results suggest that the existing Kir4.1 expression level is sufficient to set the membrane potential close to EK and that delivery of additional Kir4.1 channels to astrocytes would not significantly alter it. However, the Ba^{2+}-induced membrane potential change and the increase of input resistance are larger in Kir4.1 over-expressing astrocytes. This finding implies that application of $BaCl_2$ to Kir4.1 over-expressing astrocytes blocks a larger proportion of channels and thus produces more profound changes.

6.4.2. Overexpression of Kir4.1 channels in astrocytes increase K^+ conductance

Recorded in this chapter, Ba^{2+}-sensitive currents from astrocytes with Kir4.1 channels over-expression demonstrated enhanced conductivity when

compared to astrocytes recorded from WT mice. The analysis of *I-V* relationships also revealed a weak inward-rectifying profile. Although Kir channels have inward-rectifying properties and conduct K^+ ions into the cell more easily than out of the cell, the rate of rectification was shown to vary between different channel subtypes (Hibino et al., 2004). Kir4.x along with Kir1.x and Kir5.x encode weak rectification channels and can conduct ions in the outward direction (D'Ambrosio et al., 2002).

A weak inward-rectifying profile for Kir4.1 might be explained due to a weak space-clamp over the astrocytic protrusions. However, when Meeks and Mennerich (2007) recorded K^+ currents from an isolated membrane patch they showed that *I-V* characteristics were also only weakly rectifying. These findings suggest that a poor space-clamp has a small impact on the rectification profile of K^+ currents. According to the established properties of Kir channels, the inward rectification profile occurs because the positively charged particle blocks the ion channel pore on the intracellular side (Oliver et al., 2000). Indeed, Mg^{2+} or intracellular polyamines were shown to cause inward rectification by blocking the pore in a voltage-dependent manner (Clarke *et al*., 2010). The endogenous intracellular polyamines spermine and spermidine can be depleted from the cell or from cell patches during whole-cell recording. However, rectification properties were not dramatically affected when astrocytes were recorded with internal supplementation of spermidine or Mg^{2+} in the pipette (Meeks and Mennerick, 2007). Weak rectification profile of Kir4.1 channels allow them not only conduct K^+ into the cell but also shunt currents from site of K^+ accumulation to the extracellular space where K^+ is depleted (D'Ambrosio et al., 2018).

6.4.3. Genetic upregulation of Kir4.1 channels does not affect the baseline [Ca^{2+}]

It has been shown previously that the upregulation of Kir4.1 channel expression in astrocytes is correlated with enhanced K^+ conductance and

leads to a significant reduction in extracellular K^+ levels (Tong et al., 2014). As already known, the K^+ concentration affects the presynaptic terminal and can enhance glutamate release (Shih et al., 2013a). In turn, the enhanced release probability might increase glutamate-mediated Ca^{2+} activity in astrocytes. Several studies have investigated how up- or down-regulation of Kir4.1 channel expression in astrocytes affects K^+ buffering and glutamate uptake; however, little has been done to investigate the effect of Kir4.1 channels on Ca^{2+} signalling. In this chapter, I report that Kir4.1 channel over-expression in astrocytes does not affect the baseline [Ca^{2+}] in the over-expressing cell and neighbouring astrocytes. The objectives of this thesis are focused on changes in Ca^{2+} baseline level and not on evoked changes in Ca^{2+} dynamics. However, further evaluation of induced changes in Ca^{2+} in Kir4.1 over-expressing astrocytes might reveal important, albeit subtle, features.

6.5. Conclusion

In this chapter, I have asked how the genetic delivery of additional functional Kir4.1 channels to astrocytes affects their properties. Electrophysiological characterisation revealed that enhancing Kir4.1 channel expression does not affect the astrocytic resting membrane potential, input resistance, or basal [Ca^{2+}]. Such genetic alteration produced an over-expression of functional K^+ channels, which was confirmed by the enhanced astrocytic K^+ currents. To conclude, astrocytes with genetic Kir4.1 channel upregulation express functional Kir4.1 channels and possess typical astrocytic properties, including the capacity to form gap-junction connections with neighbouring astrocytes and to maintain their baseline [Ca^{2+}] at around 80 nM.

Chapter 7

Astrocytic Kir4.1 channels determine presynaptic glutamate release probability

7.1. Introduction

Perisynaptic astrocytic processes surround both pre- and postsynaptic terminals in the CA1 *stratum radiatum* region, providing effective clearing of accumulated extracellular K^+ during synaptic transmission (Kofuji and Newman, 2004). Indeed, by regulating K^+ homeostasis, astrocytes play a critical role in brain function in normal as well as in pathological conditions. Recent findings suggest that astrocytes shape presynaptic excitability by directly controlling the probability of synaptic transmitter release. Moreover, Sasaki et al. (2011) showed that astrocytes modulate the action potential waveform in CA3-CA1 synapses (by releasing glutamate acting on presynaptic axon AMPA/kainate receptors). They also demonstrated that local extracellular application of K^+ broadens the AP waveform (Sasaki et al., 2011). This phenomenon was further confirmed by studies showing that inhibition of K^+ channels leads to presynaptic depolarisation and distance-dependent broadening of the axonal AP (Kole et al., 2007; Shu et al., 2007). These studies highlight the importance of extracellular K^+ signalling on presynaptic glutamate release.

Here, I aim to investigate how astrocytes with the enhanced K^+ conductivity modulate presynaptic axonal functions, in particular, presynaptic glutamate release and glutamate uptake by astrocytic transporters.

7.2. Methods

To fulfil the objectives of this chapter, I used two AAV viruses: 1) a glutamate sensor expressed in neurons (AAV2/1h.Synap.SF-iGluSnFR-A184V, herein described as iGluSnFR), to monitor glutamate responses; and 2) a virus that upregulates the expression level of Kir4.1 channels in astrocytes (AAV9.pZac.2.1-gfaABC1D-tdTomato:rKcnj10). Both viruses were mixed with ACSF solution to obtain a total of 1×10^8 genomic copies in the injected volume which and then delivered to the right lateral ventricle of P0–3 neonatal pups. To assess glutamate release from presynaptic boutons in the immediate vicinity of astrocytic PAPs with upregulated expression of Kir4.1 channels, I co-injected both AAVs in a total volume not exceeding 2.5 µL per ventricle. Acute hippocampal slices were prepared 2–3 weeks after AAV injection. Glutamate transporter current recording was performed from CA1 *stratum radiatum* astrocytes using the technique described in chapter 2. In brief, stimulation of the SC was used to induce inward currents in astrocytes, and subsequent application of the glutamate transporter antagonist TBOA was used to block glutamate transporter currents. Post-hoc subtraction of K^+ currents from the mixed current yielded the glutamate transporter current.

Presynaptic glutamate release was recorded from individual boutons of CA3 pyramidal neurons. Only boutons located on the axonal branch were used for recording and further analysis. A spiral-scan line was placed over the bouton of interest, which was then scanned at a sampling frequency of ~500 Hz with two-photon excitation at 910 nm. Stimulation of the SC with a paired-pulse protocol (2 stimuli × 20 Hz) was used to trigger glutamate release. After at least 15 repetitions of the glutamate response, an extracellular solution containing 2.5 mM [K^+] was replaced with ASCF solution containing 5 mM [K^+]. Then glutamate release was acquired from the same bouton. The direct readout of the average release probability (Pr) was measured by the sum total of release successes over the total number of trials for each condition.

7.3. Results

7.3.1. Elevated extracellular [K^+] enhances presynaptic release probability

To directly measure the release probability from individual CA3 presynaptic boutons, I used acute slices transduced with a glutamate sensor (iGluSnFR*)* (Figure 7.1a). In our laboratory, we previously used this system to estimate glutamate release probability from individual presynaptic boutons. The release probability in response to a single stimulation of the SC was estimated around 0.40. Delivery of the next pulse was shown to evoke an increase of release probability in the majority of recordings, demonstrating paired-pulse facilitation (Jensen et al., 2019). Here, measured release probability was also increased from 0.37 ± 0.09 to 0.72 ± 0.08 for the second stimulus delivered to SC ($n = 8$; $p < 0.05$; two-sample t-test; Figure 7.1d, Figure 7.3a–b), also demonstrating the paired-pulse facilitation (PPF) of glutamate release from the presynaptic element. Similar PPF tendency was revealed during recording of fluorescence intensity, it increased from 29.95 ± 3.90% for the first pulse to 48.01 ± 6.52% ($n = 8$; $p < 0.05$, two-sample t-test; Figure 7.1c) for the second one.

Extracellular [K^+] accumulation during synaptic transmission was mimicked by increasing [K^+] in the ACSF solution from 2.5 mM to 5 mM. Exposure to 5 mM [K^+] extracellular solution demonstrated a significant increase in fluorescent intensity from 37.09 ± 4.18 % for first stimulus to 59.50 ± 7.86 % for the second stimulus ($n = 8$; $p < 0.05$, two-sample t-test; Figure 7.1c). Additionally, release probability showed a tendency to increase from 0.63 ± 0.09 to 0.85 ± 0.06 ($n = 8$; $p > 0.05$, two-sample t-test; Figure 7.1d). Both the increase in fluorescence intensity and release probability for the second stimulus demonstrate the facilitation of glutamate release from the presynaptic element.

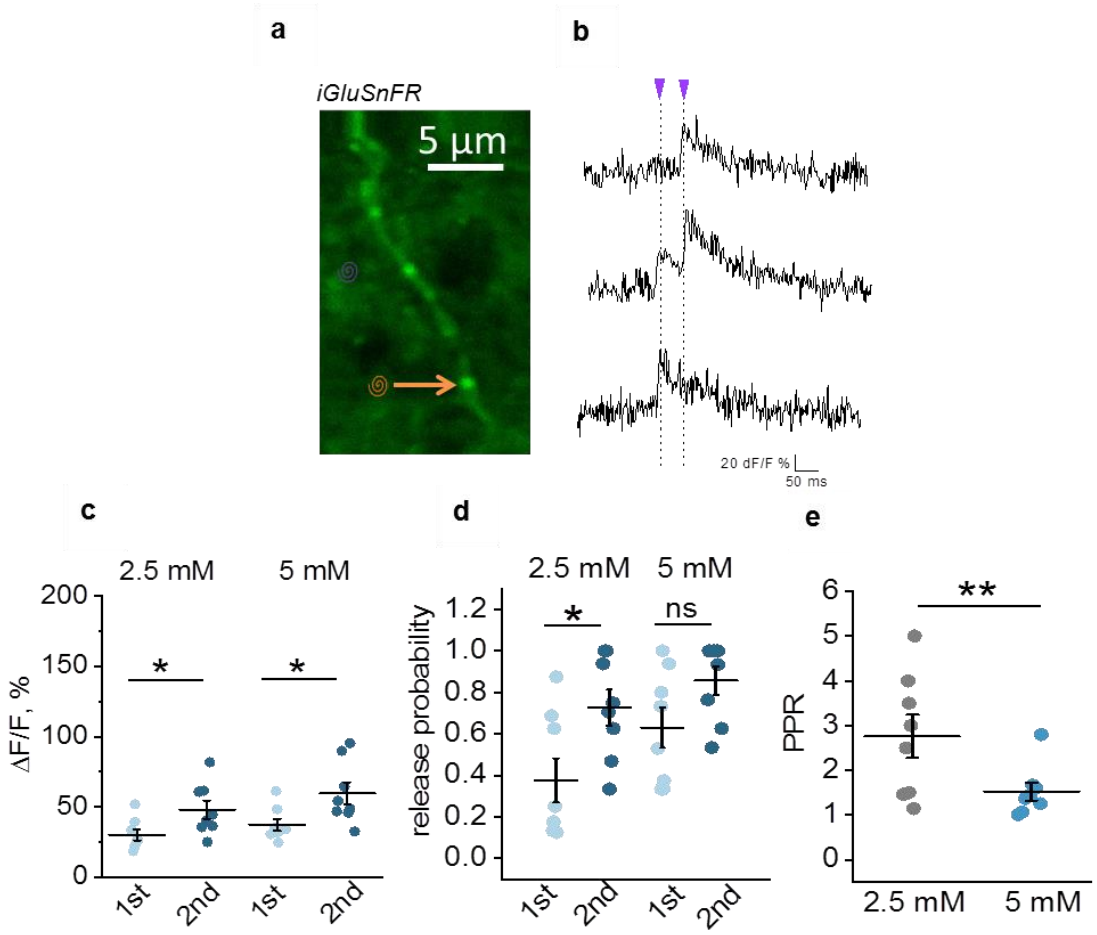

Figure 7.1 Elevation of extracellular [K^+] enhances glutamate release probability from presynaptic boutons

a- A segment of a CA3 pyramidal cell axon expressing iGluSnFR. Individual presynaptic boutons are clearly distinguishable. Spiral-scan shown in orange; dwell time, ~1.5 ms

b- Glutamate responses from an individual bouton (depicted in (a)). SC stimulation with the paired-pulse protocol (2 stimuli × 20 Hz) was used to induce glutamate release

c- $\Delta F/F$ fluorescent intensity signal, acquired from the same bouton during exposure of the slice to ACSF solution containing either 2.5 mM or 5 mM extracellular [K^+]

d- Glutamate release probability in response to the first and second stimulus for boutons in an ACSF solution containing either 2.5 mM or 5 mM extracellular [K^+]

e- An increase in extracellular [K^+] led to a significant reduction of the paired-pulse ratio.

Data are presented as mean ± SEM; ns: $p > 0.05$, *$p < 0.05$, and **$p < 0.01$.

Interestingly, the release probability in response to the first stimulus was already higher in the 5 mM [K^+] condition, implying that the increased extracellular [K^+] affects the presynaptic terminal and enhances glutamate release probability. To compare changes in the release probability of the second response to the release probability of the first one for 2.5 mM and 5 mM conditions I calculated the paired-pulse ratio (PPR). As shown in Figure 7.1e, PPR was significantly reduced from 2.76 ± 0.48 to 1.52 ± 0.20, when slice was exposed to 5 mM [K^+] ACSF solution ($n = 8$; $p < 0.01$; paired t-test). Therefore, the elevation of extracellular [K^+] underlies the increased release probability from presynaptic boutons.

7.3.2. Upregulation of Kir4.1 channel expression in astrocytes precludes K^+-mediated enhanced presynaptic glutamate release

To evaluate how the upregulation of K^+ channel expression in astrocytes affects presynaptic function, I measured glutamate release probability from boutons passing next to astrocytic PAPs over-expressing Kir4.1 channels (Figure 7.2a). When slice was exposed to 2.5 mM [K^+] ACSF solution the fluorescence intensity signal obtained from individual boutons was increased from 55.71 ± 6.07 % for the first stimulus to 90.95 ± 8.37 % for the second delivered stimulus ($n = 10$; $p < 0.001$, two-sample t-test; Figure 7.2b). In spite of the large variability of the responses, the release probability was also increased from 0.57 ± 0.09 to 0.72 ± 0.07 for the second stimulus ($n = 10$; $p > 0.05$; two-sample t-test; Figure 7.2c). Extracellular elevation of [K^+] also evoke significant increase of intensity fluorescent from 64.72 ± 9.66 % to 108.4 ± 17.20 % ($n = 10$; $p < 0.05$, two-sample t-test; Figure 7.2b).

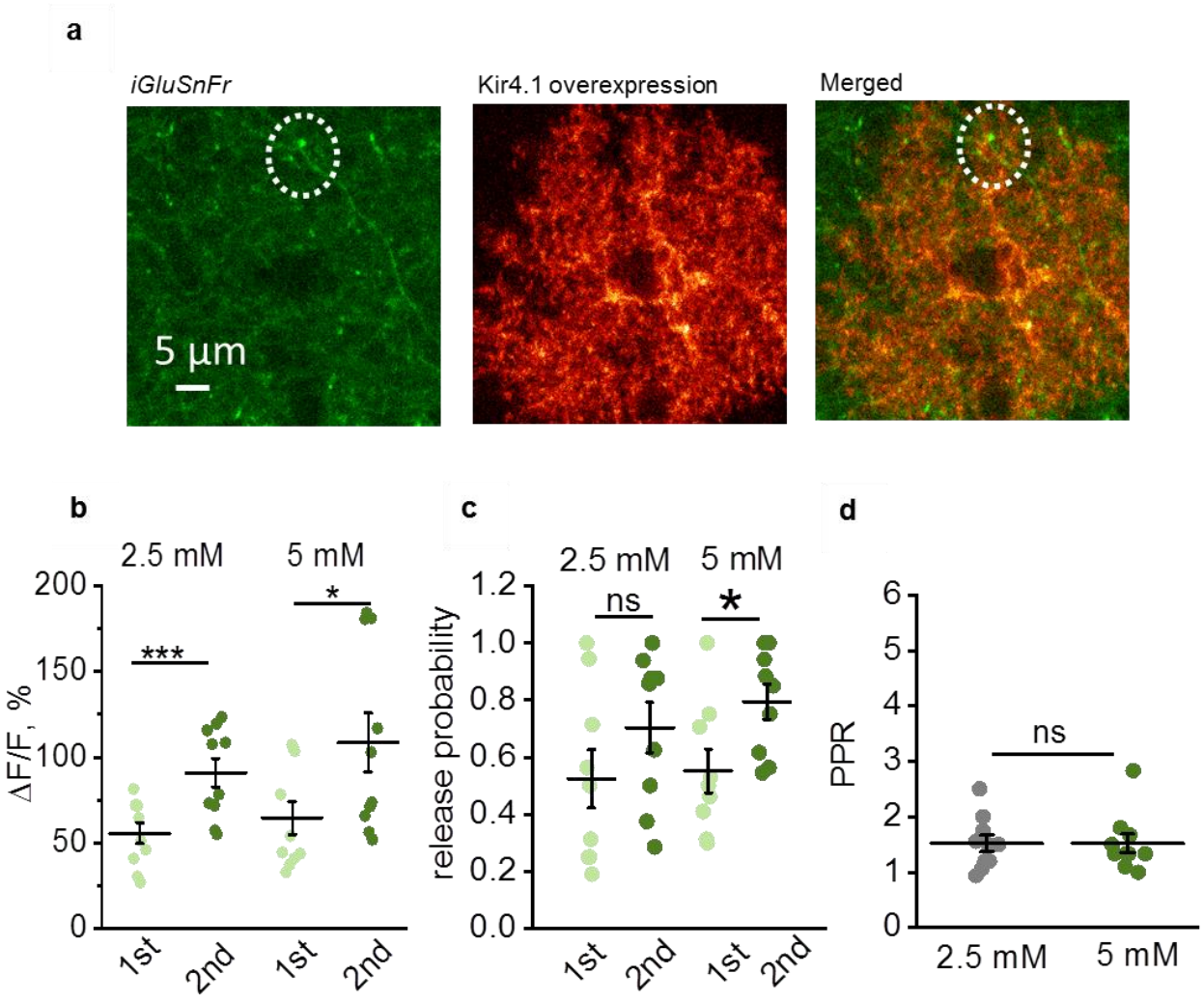

Figure 7.2 Upregulation of Kir4.1 channel expression in astrocytes precludes the K^+-mediated enhancement of release probability from presynaptic boutons

a- A segment of a CA3 pyramidal cell axon expressing iGluSnFR passing Kir4.1 over-expressing astrocytic processes. The bouton of interest is marked with a circle

b- The ΔF/F fluorescence intensity signal, acquired from the same bouton during exposure of the slice to an ACSF solution containing either 2.5 mM or 5mM extracellular [K^+]

c- Release probability in response to the first and second stimulus for boutons in ACSF solutions containing either 2.5 mM or 5 mM extracellular [K^+]

d- An increase in extracellular K^+ led to a reduction of the paired-pulse ratio.

Data are presented as mean ± SEM; ns: $p > 0.05$, *$p < 0.05$, ***$p < 0.001$.

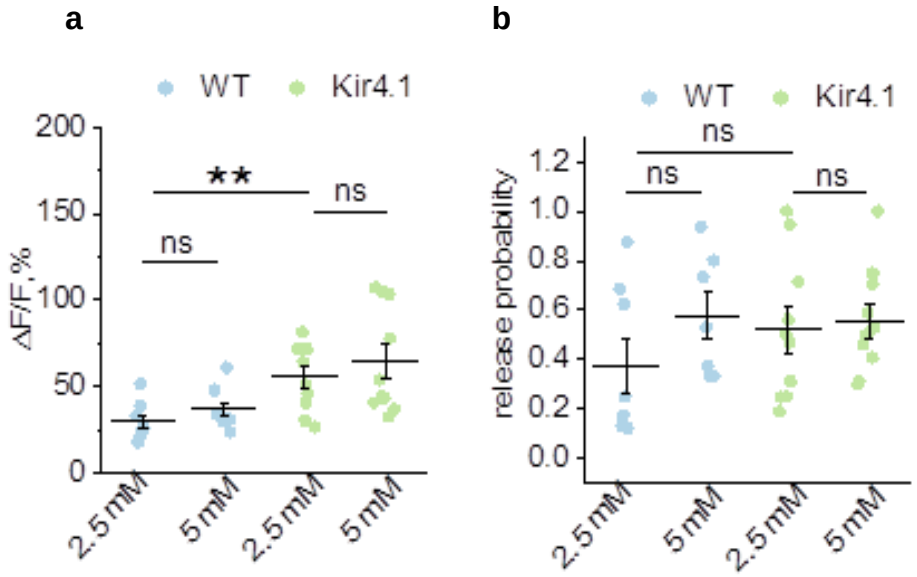

Figure 7.3 Upregulation of Kir4.1 channel expression in astrocytes increases the release probability in response to the first stimulus

a- The ΔF/F fluorescence intensity signal was higher for the first stimulus when the axon was in close vicinity to Kir4.1 over-expressing astrocytic protrusions (Kir4.1 condition)
b- Release probability for the first stimulus of the boutons passing close to the astrocyte with normal expression of Kir4.1 channels and Kir4.1 over-expression does not change, in both 2.5 mM and 5 mM conditions.

Data are presented as mean ± SEM; ns: $p > 0.05$, **$p < 0.01$

Moreover, it is led to increase of glutamate release probability from 0.55 ± 0.06 for the first stimulus to 0.77 ± 0.05 for the second one ($n = 10$; $p < 0.05$, two-sample t-test; Figure 7.2c), demonstrating changes in paired-pulse facilitation. Intriguingly, in contrast to the previous section, here exposure to 5 mM [K^+] did not affect release probability, which was confirmed with PPR ($p > 0.05$, paired t-test; Figure 7.2d). These findings suggest that the release probability from boutons passing Kir4.1 over-expressing astrocytes is insensitive to an elevation of extracellular [K^+].

7.3.3. Upregulation of Kir4.1 channel expression in astrocytes reduces activity-dependent facilitation of the glutamate transporter current

In chapter 6, I showed that upregulation of Kir4.1 channels in astrocytes enhanced K^+ currents. This finding suggests that accumulated extracellular [K^+] is rapidly removed through astrocytic K^+ channels. To evaluate how astrocytes with Kir4.1 channel over-expression take up released glutamate, I recorded glutamate transporter currents from Kir4.1 over-expressing astrocytes (Figure 7.4a). This approach allowed assessment of both glutamate release from the presynaptic terminal and the decay time. As shown in Figure 7.4a–b, Kir4.1 channel over-expression significantly reduced activity-dependent facilitation of the glutamate transporter current amplitude (n = 6; $p_{Kir4.1} < 0.0001$, $p_{stimulus} < 0.0001$, $p_{Kir4.1 \times stimulus} < 0.001$, two-way RM ANOVA). Kir over-expressing astrocytes were capable to translocated released glutamate within the same time for the both single (Ƭ decay = 7.64 ± 1.89 ms, n = 4; p > 0.05, two-sample t-test; for the difference with the WT group; Figure 7.4c) and repetitive stimulation (Ƭ decay = 18.10 ± 3.17 ms, n = 3; p > 0.05, two-sample t-test; for the difference with the WT group; Figure 7.4c). These findings suggest that the increased K^+ conductance in astrocytes decreases the amount of glutamate released during physiological synaptic transmission, but does not affect the glutamate transporter time course.

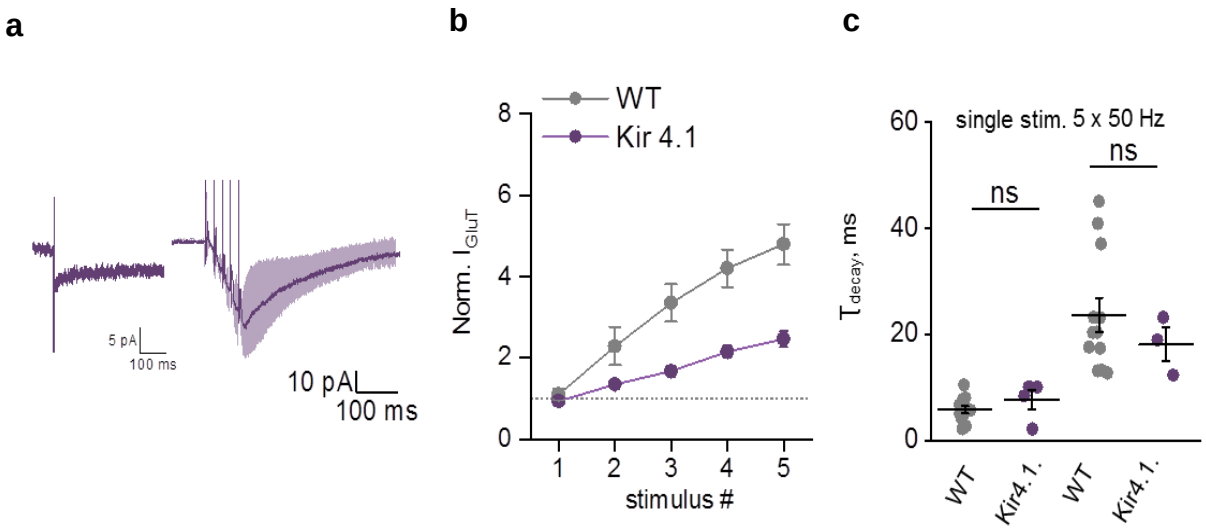

Figure 7.4 Upregulation of Kir4.1 channel expression in astrocytes reduces the amount of presynaptically released glutamate

a- Sample traces of the glutamate transporter current (I_{GluT}) recorded from Kir4.1 over-expressing astrocytes. Single or repetitive stimulation (5 × 50 Hz) was delivered to the SC to mimic synaptic transmission

b- Glutamate transporter current amplitudes during repetitive synaptic stimulation (5 × 50 Hz) normalised to the amplitude of glutamate current in response to a single stimulus. Kir4.1 over-expressing astrocytes (purple) show a significant reduction in activity-dependent facilitation compared to astrocytes in control condition (grey)

c- The decay time of I_{GluT} in response to single or repetitive stimulation. Genetic upregulation of Kir4.1 channel expression did not cause any change in the transporter current decay time.

Data are presented as mean ± SEM; ns: $p > 0.05$.

7.4. Discussion

7.4.1. Extracellular [K^+] regulates presynaptic glutamate release

A significant finding from this chapter is a direct observation that an elevation of extracellular [K^+] enhances glutamate release from an individual presynaptic terminal. It has been shown that K^+ ions play a crucial role in shaping synaptic transmission. Excessive extracellular K^+ is known to enhance presynaptic glutamate release (Shin et al., 2013), potentially through depolarisation of the presynaptic terminal, broadening of the AP, and enhanced Ca^{2+} entry (Chever et al., 2010; Sasaki et al., 2011; Sasaki, 2013; Shih et al., 2013a). Here, I showed that elevating the extracellular [K^+] from 2.5 mM to 5 mM increases release probability in individual presynaptic boutons. Despite a high degree of variability in the recorded signal, the majority of evoked responses were characterised as paired-pulse facilitation responses, with the amplitude of the second response higher than that of the first one in both 2.5 mM and 5 mM conditions. The mechanism underlying PPF is most often explained by the Ca^{2+} hypothesis. This argues that the first stimulation triggers small Ca^{2+} influx to the presynaptic terminal. This amount of Ca^{2+} is not sufficient to trigger much of a transmitter release, but contributes to further Ca^{2+} accumulation during the second stimulation. This mechanism leads to an increase of release probability by the time the second AP reaches the bouton. Additionally, the amount of facilitation has been shown to vary widely (Oertner et al., 2002; Allen and Stevens, 2006) and to be strongly dependent on the release probability of the first response (Debanne et al., 1996; Dobrunz and Stevens, 1997). Indeed, in my recordings, when presynaptic bouton was passing next to an astrocyte with normal Kir4.1 expression I showed that elevation of extracellular [K^+] increases the fluorescence intensity and the release probability of the first stimulus. Suggesting that [K^+] elevation mediated a greater portion of the Ca^{2+} influx into the presynaptic terminal. This leaves less of the Ca^{2+} available for the second stimulus and depletion of vesicles that

are ready for release. These considerations might explain why in the 5 mM condition the increase released probability for the second stimulus was lower than in the 2.5 mM condition.

7.4.2. Upregulation of Kir4.1 channel expression in astrocytes modulates presynaptic glutamate release

The most interesting finding from this chapter is that upregulation of Kir4.1 channel expression in astrocytes precludes the K^+-mediated enhancement of release probability from presynaptic boutons. Perisynaptic astroglial processes tightly associated with neuronal terminals were shown to locally modulate both pre- and post-synaptic processes. Here, when the axon passed through astrocytic PAPs with Kir4.1 channels over-expression, an elevation of extracellular [K^+] did not affect either the fluorescence intensity or the release probability of the recorded responses. The estimated paired-pulse ratio was also unchanged. These results suggest that the enhanced K^+ conductance produced by the additional insertion of functional Kir4.1 channels allows astrocytes to rapidly clear extracellular K^+ and thus eliminate its prolonged effect on presynaptic release probability.

Additionally, recordings of glutamate transporter current evoked with repetitive stimulation from Kir4.1 over-expressing astrocytes demonstrated significant reductions of its normalised amplitudes, suggesting that less glutamate is released from the presynaptic terminal and consequently sensed by astrocytic transporters. Enhanced expression of the Kir4.1 channel in astrocytes makes their glutamate transporter currents similar to those recorded when K^+ accumulation is restricted by NMDA receptor blockade (chapter 5, Figure 5.1c). This implies that enhanced K^+ conductance in astrocytes allows the rapid uptake of accumulated K^+, limiting retrograde K^+ signalling between post- and presynaptic terminals. Interestingly, as described in chapter 5, when I blocked AMPA and NMDA receptors, it led not only to a

reduction in activity-dependent transporter current potentiation, but also to a reduction in the decay time of glutamate transporters. This effect was due to K^+-induced membrane depolarisation. In this chapter I also demonstrated that the glutamate transporter decay time stays in the same range as control recordings from WT mice.

7.4.3. Variability of glutamate release probability

Several laboratories have employed optical quantum analysis to measure single synapse neurotransmitter release by comparing receptor-mediated Ca^{2+} increase in the postsynaptic terminal (Debanne et al., 1996; Oertner et al., 2002; Emptage et al., 2003). This method is limited by several factors solely associated with the properties of postsynaptic receptors. For instance, the majority of these studies were performed using NMDA receptor-mediated Ca^{2+} influx; since this receptor has relatively slow kinetics, it was not possible to measure repetitive quantal neurotransmitter release. The alternative approach used in this chapter provides direct access to the glutamate release from individual presynaptic boutons, not restricted to the kinetics of postsynaptic receptors. In addition, signal acquisition was performed with a spiral-scan, which provides a better temporal resolution and improved signal-to-noise ratio, and is also less traumatic to the cell. In line with earlier observations, these recordings also indicate that glutamate release probability varies across a wide range. It has previously been shown that quantal release from synapses is diverse and depends on presynaptic conditions that might change even between trials for the same synaptic terminal (Ermolyuk et al., 2013). This is not only due to the stochastic event of release probability, but also involves several factors, such as the properties of presynaptic receptors and channels (their activation, conductivity, and expression level), the presence of multiple release sites (Rama et al., 2019), and the size of the presynaptic terminal or vesicles themselves (Harris and Sultan, 1995). It was estimated that a two-fold increase in vesicular dimensions

could lead to an up to 8-fold variation in the amount of released neurotransmitter. Moreover, activity of the glutamate transporters responsible for loading vesicles with neurotransmitters and the degree of vesicular emptying may also vary, introducing other components of variability (Klingauf et al., 1998). Described variability might be overcome by increasing the sample number, as it was achieved by simultaneous imaging of multiple boutons in organotipic cultures (the sample size was more them 100 boutons; Jensen et al., 2019; Rama et al., 2019). The recordings presented in this chapter represent the first attempt to characterise glutamate release in organised brain tissue. It is a more challenging task due to lower chances of co-expression of both AAVs in the region of interest. Additionally, selected here strategy of paired recording from the same bouton, only allow to acquire one bouton per recording. Thus, acquisition of multiple boutons at the same time remains a challenging task.

7.4.4. Potential pathways underlying K^+-mediated enhancement in release probability from presynaptic boutons

The K^+-mediated increase of release probability reported here might occur through the broadening of the AP waveform and a consequent increase in Ca^{2+} influx in the presynaptic terminal. The exposure to elevated [K^+] levels can also activate voltage-gated Ca^{2+} channels by subthreshold presynaptic depolarisation, directly boosting Ca^{2+} transients (Bouhours et al., 2011), thus contributing to the overall Ca^{2+} rise. The observed shift of resting membrane potential could also activate presynaptic voltage-gated Kv1 channels, located in CA3 neurons (Kole et al., 2007; Shu et al., 2007; Boudkkazi et al., 2011; Foust et al., 2011; Kim, 2014). The slow kinetics of these channels (~5–10 s requires for full inactivation) underline a ~30% increase of neurotransmitter release during depolarisation-induced AP broadening (Kole

et al., 2007; Bialowas et al., 2015). This suggests that, indeed, an elevation of extracellular [K^+] could interact with presynaptic voltage-dependent channels leading to increased glutamate release probability.

7.5. Conclusion

In this chapter, I showed that over-expression of Kir4.1 channels in astrocytes curtails activity-dependent [K^+] accumulation in the synaptic cleft environment during physiological transmission. Over-expression of Kir4.1 channels in astrocytic protrusions thus regulates local glutamate release from individual Schaffer collateral boutons.

Chapter 8. General discussion

In this closing chapter, I will discuss findings from this thesis, and where they fit into the already established data. I will also consider physiological relevance of the described mechanisms, and future directions. Since the selection of a suitable methodological approach for studying glutamate transporter current parameters is crucial, I will also address some of the key technical aspects of astrocytic recordings.

8.1. Activity-dependent [K^+] accumulation facilitates the glutamate transporter current

The first and perhaps the most interesting finding is that the efficiency of the astrocytic glutamate transporter can change during physiologically compatible stimulation. Activity-dependent facilitation of the glutamate transporter current was enhanced when both NMDA and AMPA receptors were activated. Indeed, it has been shown that K^+ accumulation occurs through AMPA and NMDA receptors, with the bigger contribution coming from NMDA receptors (Bergles and Jahr, 1997; Ge and Duan, 2007). This result is in agreement with the finding that K^+ accumulation in the synaptic cleft contributes to a retrograde loop and enhances the release of neurotransmitters from the presynaptic terminal (Shih et al., 2013a). Taking advantage of glutamate transporter current recordings, I also estimated the average time required to remove an excess of glutamate from the extracellular space. Regardless of the activation of ionotropic receptors, the decay time of the recorded current evoked by a single stimulation was around 5 ms. This indicates that K^+ accumulation during single synaptic stimulation does not dramatically affect the ability of astrocytic transporters to efficiently translocate glutamate. Several groups estimate the glutamate transporter decay time

induced by a single stimulation to be between 5 and 10 ms (Grewer et al., 2000; Armbruster et al., 2016; Lebedeva et al., 2018). Thus, the transporter current decay time obtained in the current work (for a single synaptic discharge) fits in well with the accepted range in the literature.

The activity-dependent facilitation of the astrocytic transporter current presented in chapter 5 represents is a novel finding. Taking into account the important function of astrocytic transporters during synaptic transmission, several studies have attempted to evaluate the efficiency of glutamate transporters during repetitive stimulation. However, the majority of studies have used NMDA, AMPA, and $GABA_A$ receptor antagonists in the perfusion system to remove the contributions of these receptors to recorded currents (Diamond and Jahr, 2000; Meeks and Mennerick, 2007; Capuani et al., 2016). As shown in chapter 5, the predominant source of K^+ during synaptic transmission appears through the activated NMDA receptor: inhibiting this receptor should also limits K^+ build-up in the synaptic cleft. Such an experimental paradigm cannot, however, reveal the mechanism under investigation. Since the published recordings mentioned above were performed under the blockade of the ionotropic receptor, I can compare these results with those obtained in chapter 5, which were also recorded under the AMPA and NMDA receptor blockade. Among the previous studies, one appears close to the recording conditions in this thesis, in terms of stimulus frequency and numbers (Capuani et al., 2016). Indeed, in that study, the glutamate transporter decay time recorded with repetitive stimulation (10 pulses × 20 Hz; ionotropic receptors blocked) was ~8 ms; this is similar to the glutamate transporter current recorded with NMDA and AMPA receptor blockade in chapter 5 here. Therefore, the results presented in chapter 5 are in agreement with those in the literature. Importantly, they imply a mechanism regulating astrocytic glutamate transporter efficiency through an NMDA receptor-mediated accumulation of extracellular K^+.

8.2. Astrocytic glutamate transporters decay time does not depend on afferent recruitment

The second finding, which is rather unexpected, is that astrocytic glutamate transporters cannot be overwhelmed by increasing synaptic transmission. As they are essential for maintaining low extracellular levels of glutamate, the efficiency of astrocytic transporters under different levels of physiological stimulation was already investigated by Diamond and Jahr (2000). However, the authors of this study eliminated NMDA and AMPA receptors, restricting K^+ accumulation during synaptic transmission. Here, I established that glutamate transporters are capable of rapidly taking up glutamate with the same time constant, even under increased stimulation strength of SC. Nevertheless, enhanced stimulation strength of SC increase number of activated synapses in the tissue does not affect the efficiency of astrocytic glutamate uptake. I found only one recent study that investigated the efficiency of glutamate transporters under physiological stimulation (Armbruster et al., 2016). That study showed that astrocytic glutamate uptake slows down after a burst of neuronal activity. The authors used $BaCl_2$ and ionotropic glutamate receptor blockade and found that an increase in stimulation frequency suppressed glutamate uptake. This is logical because, unlike increased stimulus strength, high-frequency stimulation leads to progressive accumulation of extracellular K^+ near individual synapses (K^+ hotspots). Therefore, the efficiency of astrocytic glutamate transporters is likely to depend on cell firing frequency rather than synchronous activation of multiple synapses.

8.3. Methodological issues

Glutamate transporter current recordings from astrocytes

It is generally accepted that intense activity-driven synaptic transmission at CA3–CA1 synapses is associated with an elevation of extracellular K^+ (Kofuji and Newman, 2004). It has also been shown in multiple studies that either exogenous K^+ rises (Ransom and Goldring, 1973; Ge and Duan, 2007; Meeks and Mennerick, 2007; Rimmele et al., 2017) or physiological stimulation (Amzica et al., 2002; Ge and Duan, 2007; Chever et al., 2010) leads to astrocyte depolarisation. Although glutamate transporter operation has long been known to depend on membrane voltage (Wadiche et al., 1995; Grewer et al., 2000), the mechanism of glutamate clearance during synaptic transmission has remained poorly understood. Among the main factors limiting the study of astrocytic glutamate uptake, is the difficulty to obtain recording conditions that accurately reflect the voltage-dependent properties of astrocytic transporters. The stoichiometry of the transporter involves the translocation of one glutamate molecule, three Na^+ ions, and one H^+ ion inside, and the efflux of one K^+ ion. This stoichiometry does not allow for the glutamate transporter current, which is contaminated by inward K^+ currents, to be directly recorded. Different approaches have been explored to separate these two components of the current. Currents mediated by Kir channels are sensitive to Ba^{2+} in the low micromolar range. However, $BaCl_2$ application not only blocks Kir channels, but also increases the amplitude of the glutamate transporter current (Afzalov et al., 2013). Importantly, blocking Kir channels produces depolarisation and makes the astrocytic membrane insensitive to K^+ elevation during repetitive stimulation (Lebedeva et al., 2018). Thus, applying $BaCl_2$ to isolate the transporter current would mask the mechanism presented in this thesis. Several research groups have used an alternative approach and have blocked glutamate transporters with the non-transportable blocker TBOA (Shimamoto et al., 1998; Jabaudon et al., 1999; Shigeri et al., 2001). Further modification of TBOA allows the creation of the

TFB-TBOA form, which preferentially suppressing astrocytic glutamate transporters (Bozzo and Chatton, 2010). However, prolonged exposure to this compound induces spontaneous epileptiform discharges, restricting its usage (Tsukada et al., 2005). As mentioned in the previous section, blockade of ionotropic glutamate receptors routinely used in the early studies could have blocked an important mechanism of K^+ efflux revealed here. Several studies have used a combination of multiple antagonist in the perfusion system while recording glutamate transporter currents from astrocytes (Diamond and Jahr, 2000; Diamond, 2005; Meeks and Mennerick, 2007; Capuani et al., 2016). This methodological alteration allowed them to eliminate neuronal currents, and also to block the residual current in astrocytes. However, in these conditions the accumulation of K^+ in the synaptic cleft could have been curtailed, which would in turn prevent astrocytic depolarisation. That appears to be a plausible reason why the transporter current recordings from the earlier studies might not faithfully represent the glutamate transporter time course during synaptic stimulation.

Imaging [Ca^{2+}] and glutamate dynamics in brain tissue

Light absorption and scattering in the thick tissue of acute brain slices limit feasible imaging approaches to studying [Ca^{2+}] and glutamate dynamics (Murray, 2011). In the experiments in this thesis, I took advantage of both fluorescence intensity and lifetime imaging. Both these techniques have been applied in slices as well as *in vivo*. I will now discuss the benefits and the limitations of current approaches for signal acquisition in organised tissue specimens.

The acquisition of fluorescence signals from acute brain slices is restricted not only by the thickness of specimens, but also by other factors, including microscope settings and scanning parameters (i.e. the scanning pattern and frequency of scanning). Common approaches to improving the signal include the reduction of noise and the maximisation of the signal without extensive cell damage. Therefore, recording parameters should be carefully

selected for each particular experimental setting, taking into account the minimal requirements of particular methods. In this way, fluorescence intensity monitoring of Ca^{2+} sensitive indicators can provide information about relative changes in Ca^{2+} dynamics. Having the appropriate Ca^{2+}-sensitive dyes and an appropriate scanning frequency should allow individual Ca^{2+} transients to be resolved. Although the common Ca^{2+}-sensitive dye OGB-1 can be used to report Ca^{2+} concentration within the 10–500 nM range, accurate acquisition below 100 nM is limited. Among the limitations of this approach are the low signal-to-noise ratio, fluctuations in dye concentration, focal drift, and photobleaching. Signal quality could be improved by direct dye delivery to the cell of interest, but other limitations remain challenging to address. In contrast, the FLIM approach uses fluorescence decay rather than intensity measurements and is therefore insensitive to the indicator concentration, light scattering or absorption. This also makes FLIM insensitive to small Z-drifts of the focal plane occurring during scanning. Recent findings from our laboratory have demonstrated that changes in microenvironmental conditions in the physiological range also do not affect FLIM acquisitions (Zheng et al., 2015). Accurate FLIM acquisition requires counting and time-stamping large numbers of photons. This might be achieved by using hundreds of excitation cycles for every imaged pixel, with the number of acquired photons in repeated cycles following a Poisson distribution (Pawley, 2012). This recording cycle is counted as a single measurement and possesses an intrinsic statistical uncertainty, termed the photon noise. This sort of noise can be eliminated by increasing the number of photons measured. Most of the time, to enhance the precision of the quantities measured, experimenters increase either the recording endurance or the number of repeated cycles. Both approaches are associated with extensive exposures of the slice to the scanning laser beam and might traumatise cells, especially laser repeatedly scans small structures such as astrocytic somata or axonal boutons. Furthermore, small structures impose additional limitations upon FLIM signal acquisition. Due to their minuscule size, they have a limited number of available fluorophore molecules, resulting in a longer sampling window and consequently leading to a slower readout (Jensen

et al., 2017). In this thesis, to overcome these limitations I used a spiral-shaped line scan pattern for recording the signal from small structures in acute slices. The key advantage of the spiral scan is that it can cover a large region of interest (e.g. axonal bouton profile) at the maximum scanning frequency, for instance, over 1-2 ms only. The reduced time required for a single spiral scan is associated with a reduced laser exposure time. Correspondingly, the application of spiral-shaped line-scanning improves temporal resolution (it is possible to resolve single APs; Jensen et al., 2017) and also spatial resolution (allowing precise individual release sites to be reconstructed; (Jensen et al., 2019; Rama et al., 2019). Thus, this method represents a reliable tool for optimised fluorescence measurements from small structures.

8.4. Astrocytic depolarisation slows down glutamate uptake by transporters

An important result from this thesis is that small but significant depolarisation of astrocytic membrane slows down glutamate uptake by transporters. A computational study run by colleagues suggest that during synaptic transmission the concentration of extracellular K^+ might reach up to 5 mM (Shih et al., 2013b). So either depolarsation of perisynaptic astrocytic process or a decrease of the transmembrane K^+ gradient, or both, can potentially underpin reduced glutamate uptake (Grewer et al., 2008). In this thesis, it was established that K^+ elevation alone does not affect amplitude of glutamate transporter current, while astrocyte depolarisation increases its decay time.

Another important question to address is to what extend accumulated during synaptic transmission K^+ would depolarise PAPs? This is not a trivial task to evaluate due to several technical limitations. Fine astrocytic processes are beyond diffraction limit and does not allow resolving voltage-sensitive dyes to evaluate the range of depolarisation as well as use K^+ sensitive

microelectrode. During physiological synaptic transmission [K^+] can elevate up to 5 mM near postsynaptic receptors, but drops significantly outside of the synaptic cleft and, might strongly attenuated the effect on astrocyte membrane. Nevertheless, during HFS extracellular K^+ levels were shown to increase by several millimoles. Here, in chapter 5 we established that elevation of extracellular K^+ to 10 mM depolarise astrocytic membrane by 15 mV in average and prolonged the transporter current decay time.

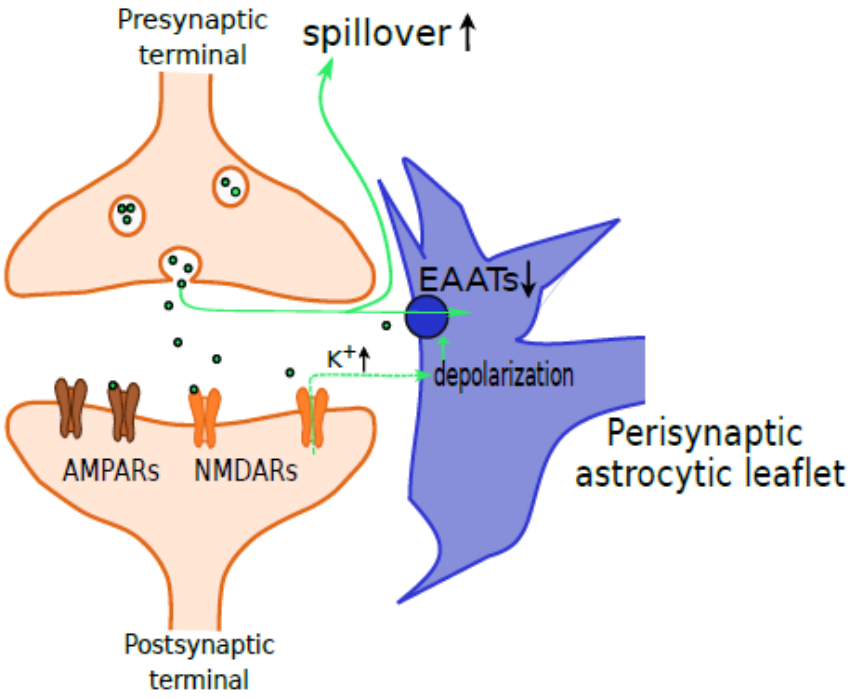

Figure 8.1 Proposed pathway for the slow-down of glutamate uptake and the consequent spillover

During physiological synaptic transmission, K^+ efflux from postsynaptic NMDA receptors rapidly depolarises astrocytes. This depolarisation induces a slow-down in the uptake of glutamate by astrocytic glutamate transporters. Excessive glutamate in the synaptic cleft promotes glutamate spillover and inter-synaptic crosstalk.

8.5. Physiological relevance

Astrocytic transporters appear to provide the fine tuning of spatiotemporal neuron–glia interactions. The contribution of astrocytic glutamate transporters to modulating physiological processes has previously been evaluated in several studies. These studies suggest that reduced expression of type-2 EAATs in various brain regions is associated with amyotrophic lateral sclerosis (Rostein et al., 1995), Alzheimer's disease (Jacob et al., 2007; Scott et al., 2011), schizophrenia (McCullumsmith et al., 2016), and drug addiction (Shen et al., 2014). In the hippocampus, blockade of astrocytic transporters enhances synaptic crosstalk (Scimemi et al., 2004) and promotes LTD (Wong et al., 2007). Astrocyte transporter-deficient mice have been shown to exhibit impaired LTP mediated via chronic NMDA receptor activation (Katagiri et al., 2001), confirming the importance of astrocytic glutamate transporters in LTP induction. In contrast, upregulation of astrocytic glutamate transporters following the intraperitoneal injection of the β-lactam antibiotic ceftriaxone prevents the expression of LTD and decreases the magnitude of LTP at mossy fibre–CA3 but not SC–CA1 synapses (Omrani et al., 2009). All of these studies underline the importance of efficient glutamate uptake for the learning and recall of extinction memory.

Here, by using several methodological approaches, I found that indeed the effective glutamate dwell-time in the synaptic cleft is correlated with the presence of postsynaptic K^+ ions. Recordings from independent pathways revealed that accumulated K^+ in the synaptic cleft promotes extrasynaptic glutamate escape (spillover). This finding suggests that glutamate spillover might indeed rapidly occur during physiological neurotransmission.

8.6. Conclusion

In this thesis, I have explored and unveiled an activity-dependent mechanism contributing to the efficiency of astrocytic glutamate transporters during physiological activity. Novel insights into the role of astrocytic glutamate uptake underline the importance of postsynaptic NMDA receptor-mediated K^+ accumulation and the resulting astrocytic depolarisation. The slow-down of glutamate uptake by transporters and the substantial levels of glutamate that transiently build up in and near the synaptic cleft may enhance inter-synaptic crosstalk between neighbouring excitatory circuits. I showed that selective over-expression of Kir4.1 channels in hippocampal astrocytes can modulate glutamate release probability at local synapses, highlighting the importance of this channel subtype to excitatory neurotransmission.

References

Abdipranoto, A., Liu, G. J., Werry, E. L., and Bennett, M. R. (2003). Mechanisms of secretion of ATP from cortical astrocytes triggered by uridine triphosphate. *Neuroreport*. doi:10.1097/00001756-200312020-00009.

Abramov, A. Y., Canevari, L., and Duchen, M. R. (2003). Changes in intracellular calcium and glutathione in astrocytes as the primary mechanism of amyloid neurotoxicity. *J. Neurosci.* 23, 5088–95. doi:10.1523/JNEUROSCI.4042-03.2004.

Abramov, A. Y., Canevari, L., and Duchen, M. R. (2004). Calcium signals induced by amyloid β peptide and their consequences in neurons and astrocytes in culture. in *Biochimica et Biophysica Acta - Molecular Cell Research* doi:10.1016/j.bbamcr.2004.09.006.

Adelman, W. J., and Fitzhugh, R. (1975). Solutions of the Hodgkin-Huxley equations modified for potassium accumulation in a periaxonal space. *Fed. Proc.*

Afzalov, R., Pryazhnikov, E., Shih, P.-Y., Kondratskaya, E., Zobova, S., Leino, S., et al. (2013). Low micromolar Ba2+ potentiates glutamate transporter current in hippocampal astrocytes. *Front. Cell. Neurosci.* doi:10.3389/fncel.2013.00135.

Akyuz, N., Altman, R. B., Blanchard, S. C., and Boudker, O. (2013). Transport dynamics in a glutamate transporter homologue. *Nature*. doi:10.1038/nature12265.

Alagem, N., Dvir, M., and Reuveny, E. (2001). Mechanism of Ba2+ block of a mouse inwardly rectifying K+ channel: Differential contribution by two discrete residues. *J. Physiol.* doi:10.1111/j.1469-7793.2001.00381.x.

Allen, C., and Stevens, C. F. (2006). An evaluation of causes for unreliability of synaptic transmission. *Proc. Natl. Acad. Sci.* doi:10.1073/pnas.91.22.10380.

Amédée, T., Robert, A., and Coles, J. A. (1997). Potassium homeostasis and glial energy metabolism. *Glia*. doi:10.1002/(SICI)1098-

1136(199709)21:1<46::AID-GLIA5>3.0.CO;2-#.

Amzica, F. (2002). In vivo electrophysiological evidences for cortical neuron-glia interactions during slow (< 1 Hz) and paroxysmal sleep oscillations. *J. Physiol. Paris*. doi:10.1016/S0928-4257(02)00008-6.

Amzica, F., Massimini, M., and Manfridi, A. (2002). Spatial buffering during slow and paroxysmal sleep oscillations in cortical networks of glial cells in vivo. *J. Neurosci.* doi:10.1523/JNEUROSCI.22-03-01042.2002.

Angulo, M. C., Kozlov, A. S., Charpak, S., and Audinat, E. (2004). Glutamate released from glial cells synchronizes neuronal activity in the hippocampus. *J. Neurosci.* 24, 6920–6927. doi:10.1523/JNEUROSCI.0473-04.2004.

Araque, a, Parpura, V., Sanzgiri, R. P., and Haydon, P. G. (1998). Glutamate-dependent astrocyte modulation of synaptic transmission between cultured hippocampal neurons. *Eur. J. Neurosci.* 10, 2129–2142. doi:10.1046/j.1460-9568.1998.00221.x.

Araque, A., Li, N., Doyle, R. T., and Haydon, P. G. (2000). SNARE protein-dependent glutamate release from astrocytes. *J. Neurosci.*

Araque, A., Parpura, V., Sanzgiri, R. P., and Haydon, P. G. (1999). Tripartite synapses: Glia, the unacknowledged partner. *Trends Neurosci.* doi:10.1016/S0166-2236(98)01349-6.

Armbruster, M., Hanson, E., and Dulla, C. G. (2016). Glutamate Clearance Is Locally Modulated by Presynaptic Neuronal Activity in the Cerebral Cortex. *J. Neurosci.* doi:10.1523/jneurosci.2066-16.2016.

Armstrong, C. M., and Hille, B. (1998). Voltage-gated ion channels and electrical excitability. *Neuron*. doi:10.1016/S0896-6273(00)80981-2.

Asztely, F., Erdemli, G., and Kullmann, D. M. (1997). Extrasynaptic glutamate spillover in the hippocampus: Dependence on temperature and the role of active glutamate uptake. *Neuron*. doi:10.1016/S0896-6273(00)80268-8.

Attwell, D., and Laughlin, S. B. (2001). An energy budget for signaling in the grey matter of the brain. *J. Cereb. Blood Flow Metab.* doi:10.1097/00004647-200110000-00001.

B. Malarkey, and Parpura, V. (2009). Mechanisms of glutamate release from astrocytes. 52, 142–154.

Bak, L. K., Schousboe, A., and Waagepetersen, H. S. (2006). The glutamate/GABA-glutamine cycle: aspects of transport, neurotransmitter homeostasis and ammonia transfer. *J. Neurochem.* 98, 641–53. doi:10.1111/j.1471-4159.2006.03913.x.

Balu, D. T., Basu, A. C., Corradi, J. P., Cacace, A. M., and Coyle, J. T. (2012). The NMDA receptor co-agonists, d-serine and glycine, regulate neuronal dendritic architecture in the somatosensory cortex. *Neurobiol. Dis.* doi:10.1016/j.nbd.2011.10.006.

Bastide, M., Bordet, R., Pu, Q., Robin, E., Puisieux, F., and Dupuis, B. (1999). Relationship between inward rectifier potassium current impairment and brain injury after cerebral ischemia/reperfusion. *J. Cereb. Blood Flow Metab.* doi:10.1097/00004647-199912000-00003.

Baylor, S. M., and Hollingworth, S. (1988). Fura- 2 calcium transients in frog skeletal muscle fibres. *J. Physiol.* doi:10.1113/jphysiol.1988.sp017244.

Bellot-Saez, A., Kékesi, O., Morley, J. W., and Buskila, Y. (2017). Astrocytic modulation of neuronal excitability through K + spatial buffering. *Neurosci. Biobehav. Rev.* 77, 87–97. doi:10.1016/j.neubiorev.2017.03.002.

Benarroch, E. E. (2016). Astrocyte signaling and synaptic homeostasis. *Neurology*. doi:10.1212/WNL.0000000000003019.

Bendahan, A., Armon, A., Madani, N., Kavanaugh, M. P., and Kanner, B. I. (2000). Arginine 447 plays a pivotal role in substrate interactions in a neuronal glutamate transporter. *J. Biol. Chem.* doi:10.1074/jbc.M006536200.

Bergles, D. E., Diamond, J. S., and Jahr, C. E. (1999). Clearance of glutamate inside the synapse and beyond. *Curr. Opin. Neurobiol.* doi:10.1016/S0959-4388(99)80043-9.

Bergles, D. E., and Jahr, C. E. (1997). Synaptic activation of glutamate transporters in hippocampal astrocytes. *Neuron*. doi:10.1016/S0896-6273(00)80420-1.

Bergles, D. E., and Jahr, C. E. (1998). Glial Contribution to Glutamate Uptake at Schaffer Collateral–Commissural Synapses in the Hippocampus. *J. Neurosci.* doi:10.1523/JNEUROSCI.18-19-07709.1998.

Bergles, D. E., Tzingounis, A. V., and Jahr, C. E. (2002). Comparison of coupled and uncoupled currents during glutamate uptake by GLT-1 transporters. *J. Neurosci.*

Bernardinelli, Y., Muller, D., and Nikonenko, I. (2014a). Astrocyte-synapse structural plasticity. *Neural Plast.* doi:10.1155/2014/232105.

Bernardinelli, Y., Randall, J., Janett, E., Nikonenko, I., König, S., Jones, E. V., et al. (2014b). Activity-dependent structural plasticity of perisynaptic astrocytic domains promotes excitatory synapse stability. *Curr. Biol.* doi:10.1016/j.cub.2014.06.025.

Berridge, M. J. (2009). Inositol trisphosphate and calcium signalling mechanisms. *Biochim. Biophys. Acta* 1793, 933–40. doi:10.1016/j.bbamcr.2008.10.005.

Bezzi, P., Carmignoto, G., Pasti, L., Vesce, S., Rossi, D., Rizzini, B. L., et al. (1998). Prostaglandins stimulate calcium-dependent glutamate release in astrocytes. *Nature* 391, 281–285. doi:10.1038/34651.

Bezzi, P., Gundersen, V., Galbete, J. L., Seifert, G., Steinhäuser, C., Pilati, E., et al. (2004). Astrocytes contain a vesicular compartment that is competent for regulated exocytosis of glutamate. *Nat. Neurosci.* doi:10.1038/nn1246.

Bezzi, P., and Volterra, A. (2001). A neuron-glia signalling network in the active brain. *Curr. Opin. Neurobiol.* doi:10.1016/S0959-4388(00)00223-3.

Biesecker, K. R., and Srienc, A. I. (2015). The Functional Role of Astrocyte Calcium Signaling in Cortical Blood Flow Regulation. *J. Neurosci.* doi:10.1523/jneurosci.4422-14.2015.

Björklund, A., and Dunnett, S. B. (2007). Dopamine neuron systems in the brain: an update. *Trends Neurosci.* 30, 194–202. doi:10.1016/j.tins.2007.03.006.

Boddum, K., Jensen, T. P., Magloire, V., Kristiansen, U., Rusakov, D. A.,

Pavlov, I., et al. (2016). Astrocytic GABA transporter activity modulates excitatory neurotransmission. *Nat. Commun.* doi:10.1038/ncomms13572.

Bohmbach, K., Schwarz, M. K., Schoch, S., and Henneberger, C. (2018). The structural and functional evidence for vesicular release from astrocytes in situ. *Brain Res. Bull.* doi:10.1016/j.brainresbull.2017.01.015.

Bordey, A., and Sontheimer, H. (1998). Properties of human glial cells associated with epileptic seizure foci. in *Epilepsy Research* doi:10.1016/S0920-1211(98)00059-X.

Bordey, A., and Sontheimer, H. (2000). Ion channel expression by astrocytes in situ: Comparison of different CNS regions. *Glia*. doi:10.1002/(sici)1098-1136(200003)30:1<27::aid-glia4>3.0.co;2-%23.

Boudker, O., Ryan, R. M., Yernool, D., Shimamoto, K., and Gouaux, E. (2007). Coupling substrate and ion binding to extracellular gate of a sodium-dependent aspartate transporter. *Nature*. doi:10.1038/nature05455.

Bozzo, L., and Chatton, J. Y. (2010). Inhibitory effects of (2S, 3S)-3-[3-[4-(trifluoromethyl)benzoylamino]benzyloxy]aspartate (TFB-TBOA) on the astrocytic sodium responses to glutamate. *Brain Res.* doi:10.1016/j.brainres.2009.12.028.

Brasnjo, G., and Otis, T. S. (2001). Neuronal glutamate transporters control activation of postsynaptic metabotropic glutamate receptors and influence cerebellar long-term depression. *Neuron*. doi:10.1016/S0896-6273(01)00377-4.

Bushong, E. a, Martone, M. E., Jones, Y. Z., and Ellisman, M. H. (2002). Protoplasmic astrocytes in CA1 stratum radiatum occupy separate anatomical domains. *J. Neurosci.* 22, 183–192. doi:22/1/183 [pii].

Cai, Z., Schools, G. P., and Kimelberg, H. K. (2000). Metabotropic glutamate receptors in acutely isolated hippocampal astrocytes: Developmental changes of mGluR5 mRNA and functional expression. *Glia*. doi:10.1002/(SICI)1098-1136(20000101)29:1<70::AID-GLIA7>3.0.CO;2-

V.

Camacho, A., and Massieu, L. (2006). Role of glutamate transporters in the clearance and release of glutamate during ischemia and its relation to neuronal death. *Arch. Med. Res.* doi:10.1016/j.arcmed.2005.05.014.

Cantrell, A. R., Smith, R. D., Goldin, A. L., Scheuer, T., and Catterall, W. A. (1997). Dopaminergic Modulation of Sodium Current in Hippocampal Neurons via cAMP-Dependent Phosphorylation of Specific Sites in the Sodium Channel α Subunit. *J. Neurosci.* 17, 7330–7338. doi:10.1523/jneurosci.17-19-07330.1997.

Capuani, C., Melone, M., Tottene, A., Bragina, L., Crivellaro, G., Santello, M., et al. (2016). Defective glutamate and K + clearance by cortical astrocytes in familial hemiplegic migraine type 2 . *EMBO Mol. Med.* doi:10.15252/emmm.201505944.

Casley, C. S., Lakics, V., Lee, H. gon, Broad, L. M., Day, T. A., Cluett, T., et al. (2009). Up-regulation of astrocyte metabotropic glutamate receptor 5 by amyloid-β peptide. *Brain Res.* doi:10.1016/j.brainres.2008.12.082.

Casper, K. B., Djukic, B., Philpot, B. D., Chin, L.-S., and McCarthy, K. D. (2007). Conditional Knock-Out of Kir4.1 Leads to Glial Membrane Depolarization, Inhibition of Potassium and Glutamate Uptake, and Enhanced Short-Term Synaptic Potentiation. *J. Neurosci.* doi:10.1523/jneurosci.0723-07.2007.

Charles, A. (1998). Intercellular calcium waves in glia. *Glia*. doi:10.1002/(SICI)1098-1136(199809)24:1<39::AID-GLIA5>3.0.CO;2-W.

Charles, A. C., Merrill, J. E., Dirksen, E. R., and Sandersont, M. J. (1991). Intercellular signaling in glial cells: Calcium waves and oscillations in response to mechanical stimulation and glutamate. *Neuron*. doi:10.1016/0896-6273(91)90238-U.

Chaudhry, F. A., Lehre, K. P., Lookeren Campagne, M. van, Ottersen, O. P., Danbolt, N. C., and Storm-Mathisen, J. (1995). Glutamate transporters in glial plasma membranes: Highly differentiated localizations revealed by quantitative ultrastructural immunocytochemistry. *Neuron*. doi:10.1016/0896-6273(95)90158-2.

Chen, T.-W., Wardill, T. J., Sun, Y., Pulver, S. R., Renninger, S. L., Baohan, A., et al. (2013). Ultrasensitive fluorescent proteins for imaging neuronal activity. *Nature* 499, 295–300. doi:10.1038/nature12354.

Chever, O., Djukic, B., McCarthy, K. D., and Amzica, F. (2010). Implication of Kir4.1 Channel in Excess Potassium Clearance: An In Vivo Study on Anesthetized Glial-Conditional Kir4.1 Knock-Out Mice. *J. Neurosci.* doi:10.1523/jneurosci.2078-10.2010.

Clarke, O. B., Caputo, A. T., Hill, A. P., Vandenberg, J. I., Smith, B. J., and Gulbis, J. M. (2010). Domain reorientation and rotation of an intracellular assembly regulate conduction in kir potassium channels. *Cell*. doi:10.1016/j.cell.2010.05.003.

Clements, J. D., Lester, R. A. J., Tong, G., Jahr, C. E., and Westbrook, G. L. (1992). The time course of glutamate in the synaptic cleft. *Science (80-.).* doi:10.1126/science.1359647.

Coco, S., Calegari, F., Pravettoni, E., Pozzi, D., Taverna, E., Rosa, P., et al. (2003). Storage and release of ATP from astrocytes in culture. *J. Biol. Chem.* doi:10.1074/jbc.M209454200.

Coetzee, W. A., Amarillo, Y., Chiu, J., Chow, A., Lau, D., McCormack, T., et al. (1999). Molecular diversity of K+ channels. in *Annals of the New York Academy of Sciences* doi:10.1111/j.1749-6632.1999.tb11293.x.

Colombo, J. A., and Reisin, H. D. (2004). Interlaminar astroglia of the cerebral cortex: A marker of the primate brain. *Brain Res.* doi:10.1016/j.brainres.2004.02.003.

Cornell-Bell, A. H., and Finkbeiner, S. M. (1991). Ca2+ waves in astrocytes. *Cell Calcium*. doi:10.1016/0143-4160(91)90020-F.

Cornell-Bell, A. H., Finkbeiner, S. M., Cooper, M. S., and Smith, S. J. (1990). Glutamate induces calcium waves in cultured astrocytes: Long-range glial signaling. *Science (80-.).* doi:10.1126/science.1967852.

Costa, R. O., Lacor, P. N., Ferreira, I. L., Resende, R., Auberson, Y. P., Klein, W. L., et al. (2012). Endoplasmic reticulum stress occurs downstream of GluN2B subunit of N-methyl-d-aspartate receptor in mature hippocampal cultures treated with amyloid-β oligomers. *Aging*

Cell. doi:10.1111/j.1474-9726.2012.00848.x.

D'Ambrosio, R., Gordon, D. S., and Winn, H. R. (2002). Differential role of KIR channel and Na(+)/K(+)-pump in the regulation of extracellular K(+) in rat hippocampus. *J. Neurophysiol.* 87, 87–102. doi:10.1152/jn.00240.2001.

D'Ambrosio, R., Maris, D. O., Grady, M. S., Winn, H. R., and Janigro, D. (2018). Impaired K + Homeostasis and Altered Electrophysiological Properties of Post-Traumatic Hippocampal Glia . *J. Neurosci.* doi:10.1523/jneurosci.19-18-08152.1999.

da Silva, W. C. N., Köhler, C. C., Radiske, A., and Cammarota, M. (2012). D1/D5 dopamine receptors modulate spatial memory formation. *Neurobiol. Learn. Mem.* 97, 271–5. doi:10.1016/j.nlm.2012.01.005.

Danbolt, N. C. (2001). Glutamate uptake. *Prog. Neurobiol.* doi:10.1016/S0301-0082(00)00067-8.

Dani, J. W., Chernjavsky, A., and Smith, S. J. (1992). Neuronal activity triggers calcium waves in hippocampal astrocyte networks. *Neuron*. doi:10.1016/0896-6273(92)90271-E.

De Felice, F. G., Velasco, P. T., Lambert, M. P., Viola, K., Fernandez, S. J., Ferreira, S. T., et al. (2007). Aβ oligomers induce neuronal oxidative stress through an N-methyl-D-aspartate receptor-dependent mechanism that is blocked by the Alzheimer drug memantine. *J. Biol. Chem.* doi:10.1074/jbc.M607483200.

De Pina-Benabou, M. H., Srinivas, M., Spray, D. C., and Scemes, E. (2018). Calmodulin Kinase Pathway Mediates the K + -Induced Increase in Gap Junctional Communication between Mouse Spinal Cord Astrocytes . *J. Neurosci.* doi:10.1523/jneurosci.21-17-06635.2001.

Debanne, D., Guérineau, N. C., Gähwiler, B. H., and Thompson, S. M. (1996). Paired-pulse facilitation and depression at unitary synapses in rat hippocampus: Quantal fluctuation affects subsequent release. *J. Physiol.* doi:10.1113/jphysiol.1996.sp021204.

Demuro, A., Mina, E., Kayed, R., Milton, S. C., Parker, I., and Glabe, C. G. (2005). Calcium dysregulation and membrane disruption as a ubiquitous

neurotoxic mechanism of soluble amyloid oligomers. *J. Biol. Chem.* 280, 17294–17300. doi:10.1074/jbc.M500997200.

Devaraju, P., Sun, M.-Y., Myers, T. L., Lauderdale, K., and Fiacco, T. A. (2013). Astrocytic group I mGluR-dependent potentiation of astrocytic glutamate and potassium uptake. *J. Neurophysiol.* doi:10.1152/jn.00517.2012.

Di Castro, M. A., Chuquet, J., Liaudet, N., Bhaukaurally, K., Santello, M., Bouvier, D., et al. (2011). Local Ca2+detection and modulation of synaptic release by astrocytes. *Nat. Neurosci.* doi:10.1038/nn.2929.

Diamond, J. S. (2001). Neuronal Glutamate Transporters Limit Activation of NMDA Receptors by Neurotransmitter Spillover on CA1 Pyramidal Cells. *J. Neurosci.* 21, 8328–8338. doi:10.1523/jneurosci.21-21-08328.2001.

Diamond, J. S. (2005). Deriving the Glutamate Clearance Time Course from Transporter Currents in CA1 Hippocampal Astrocytes: Transmitter Uptake Gets Faster during Development. *J. Neurosci.* doi:10.1523/jneurosci.5125-04.2005.

Diamond, J. S., Bergles, D. E., and Jahr, C. E. (1998). Glutamate release monitored with astrocyte transporter currents during LTP. *Neuron* 21, 425–33. doi:10.1016/S0896-6273(00)80551-6.

Diamond, J. S., and Jahr, C. E. (1997). Transporters buffer synaptically released glutamate on a submillisecond time scale. *J. Neurosci.* 17, 4672–4687.

Diamond, J. S., and Jahr, C. E. (2000). Synaptically released glutamate does not overwhelm transporters on hippocampal astrocytes during high-frequency stimulation. *J. Neurophysiol.* doi:10.1101/cshperspect.a006262.

Dobrunz, L. E., and Stevens, C. F. (1997). Heterogeneity of release probability, facilitation, and depletion at central synapses. *Neuron*. doi:10.1016/S0896-6273(00)80338-4.

Drews, A., Flint, J., Shivji, N., Jönsson, P., Wirthensohn, D., De Genst, E., et al. (2016). Individual aggregates of amyloid beta induce temporary calcium influx through the cell membrane of neuronal cells. *Sci. Rep.* 6,

31910. doi:10.1038/srep31910.

Duan, S., Anderson, C. M., Keung, E. C., Chen, Y., Chen, Y., and Swanson, R. A. (2003). P2X7 receptor-mediated release of excitatory amino acids from astrocytes. *J. Neurosci.*

Duan, S., Anderson, C. M., Stein, B. A., and Swanson, R. A. (1999). Glutamate induces rapid upregulation of astrocyte glutamate transport and cell-surface expression of GLAST. *J. Neurosci.*

Duffy, S., and MacVicar, B. A. (1994). Potassium-dependent calcium influx in acutely isolated hippocampal astrocytes. *Neuroscience*. doi:10.1016/0306-4522(94)90059-0.

Dustin, L. B. (2001). Ratiometric analysis of calcium mobilization. *Clin. Appl. Immunol. Rev.* doi:10.1016/S1529-1049(00)00002-7.

Dvorzhak, A., Vagner, T., Kirmse, K., and Grantyn, R. (2016). Functional Indicators of Glutamate Transport in Single Striatal Astrocytes and the Influence of Kir4.1 in Normal and Huntington Mice. *J. Neurosci.* doi:10.1523/jneurosci.0316-16.2016.

Emptage, N. J., Reid, C. A., Fine, A., and Bliss, T. V. P. (2003). Optical quantal analysis reveals a presynaptic component of LTP at hippocampal Schaffer-associational synapses. *Neuron*. doi:10.1016/S0896-6273(03)00325-8.

Ermolyuk, Y. S., Alder, F. G., Surges, R., Pavlov, I. Y., Timofeeva, Y., Kullmann, D. M., et al. (2013). Differential triggering of spontaneous glutamate release by P/Q-, N- and R-type Ca2+ channels. *Nat. Neurosci.* doi:10.1038/nn.3563.

Fairman, W. A., Sonders, M. S., Murdoch, G. H., and Amara, S. G. (1998). Arachidonic acid elicits a substrategated proton current associated with the glutamate transporter EAAT4. *Nat. Neurosci.* doi:10.1038/355.

Fairman, W. A., Vandenberg, R. J., Arriza, J. L., Kavanaught, M. P., and Amara, S. G. (1995). An excitatory amino-acid transporter with properties of a ligand-gated chloride channel. *Nature*. doi:10.1038/375599a0.

Fakler, B., Brändle, U., Glowatzki, E., Weidemann, S., Zenner, H. P., and

Ruppersberg, J. P. (1995). Strong voltage-dependent inward rectification of inward rectifier K+ channels is caused by intracellular spermine. *Cell*. doi:10.1016/0092-8674(95)90459-X.

Fellin, T., Pascual, O., Gobbo, S., Pozzan, T., Haydon, P. G., and Carmignoto, G. (2004). Neuronal synchrony mediated by astrocytic glutamate through activation of extrasynaptic NMDA receptors. *Neuron* 43, 729–43. doi:10.1016/j.neuron.2004.08.011.

Finch, E. A., Turner, T. J., and Goldin, S. M. (1991). Calcium as a coagonist of inositol 1,4,5-trisphosphate-induced calcium release. *Science* 252, 443–446. doi:10.1126/science.2017683.

Fischer, G., and Kettenmann, H. (1985). Cultured astrocytes from a syncytium after maturation. *Exp. Cell Res.* doi:10.1016/S0014-4827(85)80001-X.

Fischer, R., Schliess, F., and Häussinger, D. (1997). Characterization of the hypo-osmolarity-induced Ca2+ response in cultured rat astrocytes. *Glia*. doi:10.1002/(SICI)1098-1136(199705)20:1<51::AID-GLIA5>3.0.CO;2-8.

Flores-Hernandez, J., Hernandez, S., Snyder, G. L., Yan, Z., Fienberg, A. A., Moss, S. J., et al. (2000). D 1 Dopamine Receptor Activation Reduces GABA A Receptor Currents in Neostriatal Neurons Through a PKA/DARPP-32/PP1 Signaling Cascade. *J. Neurophysiol.* 83, 2996–3004. doi:10.1152/jn.2000.83.5.2996.

Furness, D. N., Dehnes, Y., Akhtar, A. Q., Rossi, D. J., Hamann, M., Grutle, N. J., et al. (2008). A quantitative assessment of glutamate uptake into hippocampal synaptic terminals and astrocytes: New insights into a neuronal role for excitatory amino acid transporter 2 (EAAT2). *Neuroscience*. doi:10.1016/j.neuroscience.2008.08.043.

Gadea, A., and López-Colomé, A. M. (2001). Glial transporters for glutamate, glycine, and GABA: II. GABA transporters. *J. Neurosci. Res.* doi:10.1002/jnr.1040.

Ge, W.-P., and Duan, S. (2007). Persistent enhancement of neuron-glia signaling mediated by increased extracellular K+ accompanying long-term synaptic potentiation. *J. Neurophysiol.* 97, 2564–2569.

doi:10.1152/jn.00146.2006.

Genoud, C., Quairiaux, C., Steiner, P., Hirling, H., Welker, E., and Knott, G. W. (2006). Plasticity of astrocytic coverage and glutamate transporter expression in adult mouse cortex. *PLoS Biol.* doi:10.1371/journal.pbio.0040343.

Giaume, C., Fromaget, C., El Aoumari, A., Cordier, J., Glowinski, J., and Grost, D. (1991). Gap junctions in cultured astrocytes: Single-channel currents and characterization of channel-forming protein. *Neuron*. doi:10.1016/0896-6273(91)90128-M.

Golovina, V. A. (2005). Visualization of localized store-operated calcium entry in mouse astrocytes. Close proximity to the endoplasmic reticulum. *J. Physiol.* doi:10.1113/jphysiol.2005.085035.

González, M. I., and Ortega, A. (1997). Regulation of the Na+-dependent high affinity glutamate/aspartate transporter in cultured Bergmann gila by phorbol esters. *J. Neurosci. Res.* doi:10.1002/(SICI)1097-4547(19971115)50:4<585::AID-JNR9>3.0.CO;2-A.

Gordon, G. R. J., Baimoukhametova, D. V., Hewitt, S. A., Rajapaksha, W. R. A. K. J. S., Fisher, T. E., and Bains, J. S. (2005). Norepinephrine triggers release of glial ATP to increase postsynaptic efficacy. *Nat. Neurosci.* doi:10.1038/nn1498.

Grewer, C., Gameiro, A., Zhang, Z., Tao, Z., Braams, S., and Rauen, T. (2008). Glutamate forward and reverse transport: From molecular mechanism to transporter-mediated release after ischemia. *IUBMB Life*. doi:10.1002/iub.98.

Grewer, C., Watzke, N., Wiessner, M., and Rauen, T. (2000). Glutamate translocation of the neuronal glutamate transporter EAAC1 occurs within milliseconds. *Proc. Natl. Acad. Sci.* doi:10.1073/pnas.160170397.

Grienberger, C., and Konnerth, A. (2012). Imaging Calcium in Neurons. *Neuron* 73, 862–885. doi:10.1016/j.neuron.2012.02.011.

Grynkiewicz, G., Poenie, M., and Tsien, R. Y. (1985). A new generation of Ca2+indicators with greatly improved fluorescence properties. *J. Biol. Chem.* doi:3838314.

Hagiwara, S., and Takahashi, K. (1974). The anomalous rectification and cation selectivity of the membrane of a starfish egg cell. *J. Membr. Biol.* doi:10.1007/BF01870103.

Haj-Yasein, N. N., Jensen, V., Vindedal, G. F., Gundersen, G. A., Klungland, A., Ottersen, O. P., et al. (2011). Evidence that compromised K + spatial buffering contributes to the epileptogenic effect of mutations in the human kir4.1 gene (KCNJ10). *Glia*. doi:10.1002/glia.21205.

Halassa, M. M., Fellin, T., Takano, H., Dong, J.-H., and Haydon, P. G. (2007). Synaptic Islands Defined by the Territory of a Single Astrocyte. *J. Neurosci.* doi:10.1523/JNEUROSCI.1419-07.2007.

Halassa, M. M., and Haydon, P. G. (2010). Integrated Brain Circuits: Astrocytic Networks Modulate Neuronal Activity and Behavior. *Annu. Rev. Physiol.* doi:10.1146/annurev-physiol-021909-135843.

Harris, K. m., and Sultan, P. (1995). Variation in the number, location and size of synaptic vesicles provides an anatomical basis for the nonuniform probability of release at hippocampal CA1 synapses. *Neuropharmacology*. doi:10.1016/0028-3908(95)00142-S.

Harrison, J. F., Rinne, M. L., Kelley, M. R., Druzhyna, N. M., Wilson, G. L., and Ledoux, S. P. (2007). Downregulation of Kir4.1 inward rectifzing potassium channel subunits bz RNAi impairs potassium transfer and glutamate uptake bz cultured cortical astrocytes. *Glia*. doi:10.1002/glia.

Haugeto, Ø., Ullensvang, K., Levy, L. M., Chaudhry, F. A., Honoré, T., Nielsen, M., et al. (1996). Brain glutamate transporter proteins form homomultimers. *J. Biol. Chem.* doi:10.1074/jbc.271.44.27715.

Haugland, R. P. (2002). *Handbook of fluorescent probes and research products*. doi:10.1007/978-1-61779-968-6.

Henneberger, C., Bard, L., Panatier, A., Reynolds, J., Medvidov, N. I., Minge, D., et al. (2018). Astroglia withdraw from potentiated synapses boosting inter-synaptic cross-talk. *bioRxiv*. doi:10.1101/349233.

Henneberger, C., Papouin, T., Oliet, S. H. R., and Rusakov, D. A. (2010a). Long-term potentiation depends on release of d-serine from astrocytes. *Nature* 463, 232–236. doi:10.1038/nature08673.

Henneberger, C., Papouin, T., Oliet, S. H. R., and Rusakov, D. a (2010b). Long-term potentiation depends on release of D-serine from astrocytes. *Nature* 463, 232–6. doi:10.1038/nature08673.

Henneberger, C., and Rusakov, D. A. (2012). Synaptic plasticity and Ca2+ signalling in astrocytes. 6, 141–146. doi:10.1017/S1740925X10000153.Synaptic.

Hertz, L. (2013). The glutamate-glutamine (GABA) cycle: Importance of late postnatal development and potential reciprocal interactions between biosynthesis and degradation. *Front. Endocrinol. (Lausanne).* doi:10.3389/fendo.2013.00059.

Hibino, H., Fujita, A., Iwai, K., Yamada, M., and Kurachi, Y. (2004). Differential assembly of inwardly rectifying K+ channel subunits, Kir4.1 and Kir5.1, in brain astrocytes. *J. Biol. Chem.* doi:10.1074/jbc.M405985200.

Higashi, K., Fujita, A., Inanobe, A., Tanemoto, M., Doi, K., Kubo, T., et al. (2001). An inwardly rectifying K(+) channel, Kir4.1, expressed in astrocytes surrounds synapses and blood vessels in brain. *Am. J. Physiol. Cell Physiol.* doi:10.1152/ajpcell.2001.281.3.C922.

Hinterkeuser, S., Schröder, W., Hager, G., Seifert, G., Blümcke, I., Elger, C. E., et al. (2000). Astrocytes in the hippocampus of patients with temporal lobe epilepsy display changes in potassium conductances. *Eur. J. Neurosci.* doi:10.1046/j.1460-9568.2000.00104.x.

Hirase, H., Qian, L., Barthó, P., and Buzsáki, G. (2004). Calcium dynamics of cortical astrocytic networks in vivo. *PLoS Biol.* doi:10.1371/journal.pbio.0020096.

Hof, P. R., Grossman, L. I., Bonar, C. J., Uddin, M., Wildman, D. E., Redmond, J. C., et al. (2006). Evolution of increased glia-neuron ratios in the human frontal cortex. *Proc. Natl. Acad. Sci.* doi:10.1073/pnas.0605843103.

Holtzclaw, L. A., Pandhit, S., Bare, D. J., Mignery, G. A., and Russell, J. T. (2002). Astrocytes in adult rat brain express type 2 inositol 1,4,5-trisphosphate receptors. *Glia*. doi:10.1002/glia.10085.

Huang, Y. H. (2004). Astrocyte Glutamate Transporters Regulate Metabotropic Glutamate Receptor-Mediated Excitation of Hippocampal Interneurons. *J. Neurosci.* doi:10.1523/JNEUROSCI.5217-03.2004.

Jabaudon, D., Shimamoto, K., Yasuda-Kamatani, Y., Scanziani, M., Gähwiler, B. H., and Gerber, U. (1999). Inhibition of uptake unmasks rapid extracellular turnover of glutamate of nonvesicular origin. *Proc. Natl. Acad. Sci. U. S. A.* 96, 8733–8738. doi:10.1073/pnas.96.15.8733.

Jacob, C. P., Koutsilieri, E., Bartl, J., Neuen-Jacob, E., Arzberger, T., Zander, N., et al. (2007). Alterations in expression of glutamatergic transporters and receptors in sporadic Alzheimer's disease. *J. Alzheimer's Dis.* doi:10.3233/JAD-2007-11113.

Jankowsky, J. L., Grunke, S. D., Kim, J.-Y., Golde, T. E., and Levites, Y. (2014). Intracerebroventricular Viral Injection of the Neonatal Mouse Brain for Persistent and Widespread Neuronal Transduction. *J. Vis. Exp.* doi:10.3791/51863.

Jensen, T. P., Zheng, K., Cole, N., Marvin, J. S., Looger, L. L., and Rusakov, D. A. (2019). Multiplex imaging relates quantal glutamate release to presynaptic Ca 2+ homeostasis at multiple synapses in situ. *Nat. Commun.* doi:10.1038/s41467-019-09216-8.

Jensen, T. P., Zheng, K., Tyurikova, O., Reynolds, J. P., and Rusakov, D. A. (2017a). Monitoring single-synapse glutamate release and presynaptic calcium concentration in organised brain tissue. *Cell Calcium* 64. doi:10.1016/j.ceca.2017.03.007.

Jensen, T. P., Zheng, K., Tyurikova, O., Reynolds, J. P., and Rusakov, D. A. (2017b). Monitoring single-synapse glutamate release and presynaptic calcium concentration in organised brain tissue. *Cell Calcium*. doi:10.1016/j.ceca.2017.03.007.

Jiang, R., Haustein, M. D., Sofroniew, M. V., and Khakh, B. S. (2014). Imaging Intracellular Ca^{2+} Signals in Striatal Astrocytes from Adult Mice Using Genetically-encoded Calcium Indicators. *J. Vis. Exp.* doi:10.3791/51972.

Kanemaru, K., Sekiya, H., Xu, M., Satoh, K., Kitajima, N., Yoshida, K., et al.

(2014). In Vivo visualization of subtle, transient, and local activity of astrocytes using an ultrasensitive Ca 2+ indicator. *Cell Rep.* doi:10.1016/j.celrep.2014.05.056.

Kao, J. P. Y., Li, G., and Auston, D. A. (2010). *Practical aspects of measuring intracellular calcium signals with fluorescent indicators*. doi:10.1016/B978-0-12-374841-6.00005-0.

Karwoski, C. J., Lu, H. K., and Newman, E. A. (1989). Spatial buffering of light-evoked potassium increases by retinal Müller (glial) cells. *Science (80-.).* doi:10.1126/science.2785716.

Katagiri, H., Tanaka, K., and Manabe, T. (2001). Requirement of appropriate glutamate concentrations in the synaptic cleft for hippocampal LTP induction. *Eur. J. Neurosci.* doi:10.1046/j.0953-816X.2001.01664.x.

Kato, K., Clifford, D. B., and Zorumski, C. F. (1993). Long-term potentiation during whole-cell recording in rat hippocampal slices. *Neuroscience*. doi:10.1016/0306-4522(93)90282-K.

Katz, B., and Miledi, R. (1968). The role of calcium in neuromuscular facilitation. *J. Physiol.* doi:10.1113/jphysiol.1968.sp008469.

Khan, Z. U., Koulen, P., Rubinstein, M., Grandy, D. K., and Goldman-Rakic, P. S. (2001). An astroglia-linked dopamine D2-receptor action in prefrontal cortex. *Proc. Natl. Acad. Sci. U. S. A.* 98, 1964–9. doi:10.1073/pnas.98.4.1964.

Kim, K., Lee, S. G., Kegelman, T. P., Su, Z. Z., Das, S. K., Dash, R., et al. (2011). Role of Excitatory Amino Acid Transporter-2 (EAAT2) and glutamate in neurodegeneration: Opportunities for developing novel therapeutics. *J. Cell. Physiol.* 226, 2484–2493. doi:10.1002/jcp.22609.

Kimelberg, H. K., Goderie, S. K., Higman, S., Pang, S., and Waniewski, R. A. (1990). Swelling-induced release of glutamate, aspartate, and taurine form astrocyte cultures. *J. Neurosci.* 10, 1583–1591.

Kirischuk, S., Kirchhoff, F., Matyash, V., Kettenmann, H., and Verkhratsky, A. (1999). Glutamate-triggered calcium signalling in mouse Bergmann glial cells in situ: Role of inositol-1,4,5-trisphosphate-mediated intracellular calcium release. *Neuroscience*. doi:10.1016/S0306-4522(99)00067-6.

Kivi, A., Lehmann, T. N., Kovács, R., Eilers, A., Jauch, R., Meencke, H. J., et al. (2000). Effects of barium on stimulus-induced rises of [K+](o) in human epileptic non-sclerotic and sclerotic hippocampal area CA1. *Eur. J. Neurosci.* doi:10.1046/j.1460-9568.2000.00103.x.

Klingauf, J., Kavalali, E. T., and Tsien, R. W. (1998). Kinetics and regulation of fast endocytosis at hippocampal synapses. *Nature*. doi:10.1038/29079.

Kofuji, P., Ceelen, P., Zahs, K. R., Surbeck, L. W., Lester, H. A., and Newman, E. A. (2000). Genetic inactivation of an inwardly rectifying potassium channel (Kir4.1 subunit) in mice: phenotypic impact in retina. *J. Neurosci.*

Kofuji, P., and Newman, E. A. (2004). Potassium buffering in the central nervous system. *Neuroscience* 129, 1045–1056. doi:10.1016/j.neuroscience.2004.06.008.

Koizumi, S. (2010). Synchronization of Ca2+ oscillations: involvement of ATP release in astrocytes. *FEBS J.* 277, 286–292. Available at: http://www.ncbi.nlm.nih.gov/pubmed/19895581.

Kole, M. H. P., Letzkus, J. J., and Stuart, G. J. (2007). Axon Initial Segment Kv1 Channels Control Axonal Action Potential Waveform and Synaptic Efficacy. *Neuron*. doi:10.1016/j.neuron.2007.07.031.

Konietzko, U., and Müller, C. M. (1994). Astrocytic dye coupling in rat hippocampus: Topography, developmental onset, and modulation by protein kinase C. *Hippocampus*. doi:10.1002/hipo.450040313.

Kreft, M., Stenovec, M., Rupnik, M., Grilc, S., Kržan, M., Potokar, M., et al. (2004). Properties of Ca2+-dependent exocytosis in cultured astrocytes. *Glia*. doi:10.1002/glia.20018.

Kristian Enkvist, M. O., and McCarthy, K. D. (1994). Astroglial Gap Junction Communication Is Increased by Treatment with Either Glutamate or High K+ Concentration. *J. Neurochem.* doi:10.1046/j.1471-4159.1994.62020489.x.

Krzan, M., Stenovec, M., Kreft, M., Pangršič, T., Grilc, S., Haydon, P. G., et al. (2003). Calcium-dependent exocytosis of atrial natriuretic peptide

from astrocytes. *J. Neurosci.* doi:10.1523/jneurosci.23-05-01580.2003.

Kuchibhotla, K. V., Lattarulo, C. R., Hyman, B. T., and Bacskai, B. J. (2009). Synchronous hyperactivity and intercellular calcium waves in astrocytes in Alzheimer mice. *Science (80-.).* doi:10.1126/science.1169096.

Kuffler SW, Nicholls JG, O. R. (1966). PHYSIOLOGICAL PROPERTIES OF GLIAL CELLS IN THE CENTRAL NERVOUS SYSTEM OF AMPHIBIAl. *Methods* J Neurophy, 768–787.

Kuga, N., Sasaki, T., Takahara, Y., Matsuki, N., and Ikegaya, Y. (2011). Large-scale calcium waves traveling through astrocytic networks in vivo. *J. Neurosci.* 31, 2607–14. doi:10.1523/JNEUROSCI.5319-10.2011.

Kugler, P., and Schleyer, V. (2004). Developmental expression of glutamate transporters and glutamate dehydrogenase in astrocytes of the postnatal rat hippocampus. *Hippocampus*. doi:10.1002/hipo.20015.

Lalo, U., Pankratov, Y., Kirchhoff, F., North, R. A., and Verkhratsky, A. (2006). NMDA receptors mediate neuron-to-glia signaling in mouse cortical astrocytes. *J. Neurosci.* 26, 2673–83. doi:10.1523/JNEUROSCI.4689-05.2006.

Lalo, U., Pankratov, Y., Parpura, V., and Verkhratsky, A. (2011). Ionotropic receptors in neuronal-astroglial signalling: What is the role of “excitable” molecules in non-excitable cells. *Biochim. Biophys. Acta - Mol. Cell Res.* doi:10.1016/j.bbamcr.2010.09.007.

Larsen, B. R., Assentoft, M., Cotrina, M. L., Hua, S. Z., Nedergaard, M., Kaila, K., et al. (2014). Contributions of the Na+/K+-ATPase, NKCC1, and Kir4.1 to hippocampal K+ clearance and volume responses. *Glia*. doi:10.1002/glia.22629.

Lau, L. T., and Yu, A. C. H. (2001). Astrocytes produce and release interleukin-1, interleukin-6, tumor necrosis factor alpha and interferon-gamma following traumatic and metabolic injury. *J. Neurotrauma*. doi:10.1089/08977150151071035.

Laurén, J., Gimbel, D. A., Nygaard, H. B., Gilbert, J. W., and Strittmatter, S. M. (2009). Cellular prion protein mediates impairment of synaptic plasticity by amyloid-B oligomers. *Nature*. doi:10.1038/nature07761.

Lebedeva, A., Plata, A., Nosova, O., Tyurikova, O., and Semyanov, A. (2018). Activity-dependent changes in transporter and potassium currents in hippocampal astrocytes. *Brain Res. Bull.* 136. doi:10.1016/j.brainresbull.2017.08.015.

Lehre, K. P., and Danbolt, N. C. (1998). The Number of Glutamate Transporter Subtype Molecules at Glutamatergic Synapses : Chemical and Stereological Quantification in Young Adult Rat Brain. 18, 8751–8757.

Lehre, K. P., Levy, L. M., Storm-mathisen, J., Ottersen, O. P., and Danbolt, N. C. (1995). Differential expression of two glial glutamate transporters in the rat brain: quantitative and immunocytochemical observations.

Lester, R. A. J., Clements, J. D., Westbrook, G. L., and Jahr, C. E. (1990). Channel kinetics determine the time course of NMDA receptor-mediated synaptic currents. *Nature*. doi:10.1038/346565a0.

Leyton, M., and Vezina, P. (2014). Dopamine ups and downs in vulnerability to addictions: A neurodevelopmental model. *Trends Pharmacol. Sci.* 35, 268–276. doi:10.1016/j.tips.2014.04.002.

Li, S., Mealing, G. A. R., Morley, P., and Stys, P. K. (2018). Novel Injury Mechanism in Anoxia and Trauma of Spinal Cord White Matter: Glutamate Release via Reverse Na + -dependent Glutamate Transport . *J. Neurosci.* doi:10.1523/jneurosci.19-14-j0002.1999.

Lim, D., Iyer, A., Ronco, V., Grolla, A. A., Canonico, P. L., Aronica, E., et al. (2013). Amyloid beta deregulates astroglial mGluR5-mediated calcium signaling via calcineurin and Nf-kB. *Glia*. doi:10.1002/glia.22502.

Liu, H. T., Tashmukhamedov, B. A., Inoue, H., Okada, Y., and Sabirov, R. Z. (2006). Roles of two types of anion channels in glutamate release from mouse astrocytes under ischemic or osmotic stress. *Glia*. doi:10.1002/glia.20400.

Liu, Q. S., Xu, Q., Arcuino, G., Kang, J., and Nedergaard, M. (2004). Astrocyte-mediated activation of neuronal kainate receptors. *Proc.Natl.Acad.Sci.U.S.A*. doi:10.1073/pnas.0306731101.

Longuemare, M. C., and Swanson, R. A. (1995). Excitatory amino acid

release from astrocytes during energy failure by reversal of sodium-dependent uptake. *J. Neurosci. Res.* doi:10.1002/jnr.490400312.

Lückhoff, A. (1986). Measuring cytosolic free calcium concentration in endothelial cells with indo-1: The pitfall of using the ratio of two fluorescence intensities recorded at different wavelengths. *Cell Calcium*. doi:10.1016/0143-4160(86)90003-5.

MacVicar, B. A., and Choi, H. B. (2017). Astrocytes Provide Metabolic Support for Neuronal Synaptic Function in Response to Extracellular K+. *Neurochem. Res.* 42, 2588–2594. doi:10.1007/s11064-017-2315-8.

Macvicar, B. A., Feighan, D., Brown, A., and Ransom, B. (2002). Intrinsic optical signals in the rat optic nerve: Role for K + uptake via NKCC1 and swelling of astrocytes. *Glia*. doi:10.1002/glia.10023.

Malgaroli, A., Milani, D., Meldolesi, J., and Pozzan, T. (1987). Fura-2 measurements of cytosolic free Ca2+in monolayers and suspensions of various types of animal cells. *J. Cell Biol.* doi:10.1083/jcb.105.5.2145.

Maravall, M., Mainen, Z. F., Sabatini, B. L., and Svoboda, K. (2000). Estimating intracellular calcium concentrations and buffering without wavelength ratioing. *Biophys. J.* 78, 2655–2667. doi:10.1016/S0006-3495(00)76809-3.

Marcaggi, P., Hirji, N., and Attwell, D. (2005). Release of L-aspartate by reversal of glutamate transporters. *Neuropharmacology*. doi:10.1016/j.neuropharm.2005.07.011.

Martineau, M., Parpura, V., and Mothet, J. P. (2014). Cell-type specific mechanisms of D-serine uptake and release in the brain. *Front. Synaptic Neurosci.* doi:10.3389/fnsyn.2014.00012.

Massa, P. T., and Mugnaini, E. (1985). Cell-cell junctional interactions and characteristic plasma membrane features of cultured rat glial cells. *Neuroscience*. doi:10.1016/0306-4522(85)90320-3.

McBain, C. J. (1994). Hippocampal inhibitory neuron activity in the elevated potassium model of epilepsy. *J. Neurophysiol.* 73, 2853–2863. doi:10.1152/jn.1995.73.2.2853.

McCullumsmith, R. E., O'Donovan, S. M., Drummond, J. B., Benesh, F. S.,

Simmons, M., Roberts, R., et al. (2016). Cell-specific abnormalities of glutamate transporters in schizophrenia: Sick astrocytes and compensating relay neurons? *Mol. Psychiatry*. doi:10.1038/mp.2015.148.

Meeks, J. P., and Mennerick, S. (2004). Selective Effects of Potassium Elevations on Glutamate Signaling and Action Potential Conduction in Hippocampus. *J. Neurosci.* doi:10.1523/JNEUROSCI.4845-03.2004.

Meeks, J. P., and Mennerick, S. (2007). Astrocyte membrane responses and potassium accumulation during neuronal activity. *Hippocampus*. doi:10.1002/hipo.20344.

Meldrum, B. S. (2018). Glutamate as a Neurotransmitter in the Brain: Review of Physiology and Pathology. *J. Nutr.* doi:10.1093/jn/130.4.1007s.

Mennerick, S., and Zorumski, C. F. (1994). Glial contributions to excitatory neurotransmission in cultured hippocampal cells. *Nature*. doi:10.1038/368059a0.

Minelli, A., Barbaresi, P., Reimer, R. J., Edwards, R. H., and Conti, F. (2001). The glial glutamate transporter GLT-1 is localized both in the vicinity of and at distance from axon terminals in the rat cerebral cortex. *Neuroscience*. doi:10.1016/S0306-4522(01)00375-X.

Minich, T., Riemer, J., Schulz, J. B., Wielinga, P., Wijnholds, J., and Dringen, R. (2006). The multidrug resistance protein 1 (Mrp1), but not Mrp5, mediates export of glutathione and glutathione disulfide from brain astrocytes. *J. Neurochem.* doi:10.1111/j.1471-4159.2006.03737.x.

Missale, C., Nash, S. R., Robinson, S. W., Jaber, M., and Caron, M. G. (1998). Dopamine receptors: from structure to function. *Physiol. Rev.* 78, 189–225. doi:10.1186/1471-2296-12-32.

Montana, V., Malarkey, E. B., Verderio, C., Matteoli, M., and Parpura, V. (2006). Vesicular transmitter release from astrocytes. *Glia* 54, 700–715. doi:10.1002/glia.20367.

Morales-Mulia, S., Vaca, L., Hernandez-Cruz, A., and Pasantes-Morales, H. (1998). Osmotic swelling-induced changes in cytosolic calcium do not affect regulatory volume decrease in rat cultured suspended cerebellar

astrocytes. *J. Neurochem.*

Morte, B., and Bernal, J. (2014). Thyroid hormone action: Astrocyte-neuron communication. *Front. Endocrinol. (Lausanne).* doi:10.3389/fendo.2014.00082.

Murphy-Royal, C., Dupuis, J. P., Varela, J. A., Panatier, A., Pinson, B., Baufreton, J., et al. (2015). Surface diffusion of astrocytic glutamate transporters shapes synaptic transmission. *Nat. Neurosci.* doi:10.1038/nn.3901.

Murray, J. M. (2011). Methods for imaging thick specimens: Confocal microscopy, deconvolution, and structured illumination. *Cold Spring Harb. Protoc.* doi:10.1101/pdb.top066936.

Nagaoka, T., Masuda, A., and Takamatsu, T. (2011). Lowering Extracellular pH Raises Intracellular Calcium in Cultured Rat Astrocytes. *Acta Histochem. Cytochem.* doi:10.1267/ahc.30.221.

Nagy, J. I., Patel, D., Ochalski, P. A. Y., and Stelmack, G. L. (1999). Connexin30 in rodent, cat and human brain: Selective expression in gray matter astrocytes, co-localization with connexin43 at gap junction and late developmental appearance. *Neuroscience*. doi:10.1016/S0306-4522(98)00191-2.

Nagy, J. I., and Rash, J. E. (2000). Connexins and gap junctions of astrocytes and oligodendrocytes in the CNS. *Brain Res. Rev.* doi:10.1016/S0165-0173(99)00066-1.

Nett, W. J., Oloff, S. H., and McCarthy, K. D. (2002). Hippocampal astrocytes in situ exhibit calcium oscillations that occur independent of neuronal activity. *J. Neurophysiol.* 87, 528–537. Available at: http://www.ncbi.nlm.nih.gov/pubmed/11784768.

Neusch, C., Papadopoulos, N., Müller, M., Maletzki, I., Winter, S. M., Hirrlinger, J., et al. (2005). Lack of the Kir4.1 Channel Subunit Abolishes K + Buffering Properties of Astrocytes in the Ventral Respiratory Group: Impact on Extracellular K + Regulation . *J. Neurophysiol.* doi:10.1152/jn.00996.2005.

Neusch, C., Rozengurt, N., Jacobs, R. E., Lester, H. A., and Kofuji, P. (2001).

Kir4.1 potassium channel subunit is crucial for oligodendrocyte development and in vivo myelination. *J. Neurosci.*

Newman, E. A. (1987). Regulation of potassium levels by Muller cells in the vertebrate retina. *Can. J. Physiol. Pharmacol.* doi:10.1139/y87-162.

Newman, E. A. (1993). Inward-rectifying potassium channels in retinal glial (m??ller) cells. *J. Neurosci.*

Newman, E. A. (2001). Propagation of Intercellular Calcium Waves in Retinal Astrocytes and Müller Cells. *J. Neurosci.* doi:21/7/2215 [pii].

Nicholls, D., and Attwell, D. (1990). The release and uptake of excitatory amino acids. *Trends Pharmacol. Sci.* doi:10.1016/0165-6147(90)90129-V.

Nowak, L., Bregestovski, P., Ascher, P., Herbet, A., and Prochiantz, A. (1984). Magnesium gates glutamate-activated channels in mouse central neurones. *Nature*. doi:10.1038/307462a0.

Nutt, D. J., Lingford-Hughes, A., Erritzoe, D., and Stokes, P. R. a (2015). The dopamine theory of addiction: 40 years of highs and lows. *Nat. Rev. Neurosci.* 16, 305–312. doi:10.1038/nrn3939.

Oberheim, N. A., Takano, T., Han, X., He, W., Lin, J. H. C., Wang, F., et al. (2009). Uniquely Hominid Features of Adult Human Astrocytes. *J. Neurosci.* doi:10.1523/JNEUROSCI.4707-08.2009.

Oertner, T. G., Sabatini, B. L., Nimchinsky, E. A., and Svoboda, K. (2002). Facilitation at single synapses probed with optical quantal analysis. *Nat. Neurosci.* doi:10.1038/nn867.

Ogata, K., and Kosaka, T. (2002). Structural and quantitative analysis of astrocytes in the mouse hippocampus. *Neuroscience*. doi:10.1016/S0306-4522(02)00041-6.

Oliet, S. H. R., Piet, R., and Poulain, D. A. (2001). Control of glutamate clearance and synaptic efficacy by glial coverage of neurons. *Science (80-.).* doi:10.1126/science.1059162.

Oliet, S. H. R., Syková, E., Poulain, D. A., Vargová, L., and Piet, R. (2004). Physiological contribution of the astrocytic environment of neurons to intersynaptic crosstalk. *Proc. Natl. Acad. Sci.*

doi:10.1073/pnas.0308408100.

Oliver, D., Baukrowitz, T., and Fakler, B. (2000). Polyamines as gating molecules of inward-rectifier K+ channels. *Eur. J. Biochem.* doi:10.1046/j.1432-1327.2000.01669.x.

Olsen, M. L., Higashimori, H., Campbell, S. L., Hablitz, J. J., and Sontheimer, H. (2006). Functional expression of Kir4.1 channels in spinal cord astrocytes. *Glia*. doi:10.1002/glia.20312.

Olsen, M. L., and Sontheimer, H. (2004). Mislocalization of Kir Channels in Malignant Glia. *Glia*. doi:10.1002/glia.10346.

Olsen, M. L., and Sontheimer, H. (2008). Functional implications for Kir4.1 channels in glial biology: From K + buffering to cell differentiation. *J. Neurochem.* doi:10.1111/j.1471-4159.2008.05615.x.

Omrani, A., Melone, M., Bellesi, M., Safiulina, V., Aida, T., Tanaka, K., et al. (2009). Up-regulation of GLT-1 severely impairs LTD at mossy fibre-CA3 synapses. *J. Physiol.* doi:10.1113/jphysiol.2009.177881.

Orkand, R. K., Nicholls, J. G., and Kuffler, S. W. (1966). Effect of nerve impulses on the membrane potential of glial cells in the central nervous system of amphibia. *J. Neurophysiol.* 29, 788–806. doi:10.1152/jn.1966.29.4.788.

Otis, T. S., and Jahr, C. E. (1998). Anion currents and predicted glutamate flux through a neuronal glutamate transporter. *J. Neurosci.*

Otsu, Y., Couchman, K., Lyons, D. G., Collot, M., Agarwal, A., Mallet, J. M., et al. (2015). Calcium dynamics in astrocyte processes during neurovascular coupling. *Nat. Neurosci.* doi:10.1038/nn.3906.

Owe, S. G., Marcaggi, P., and Attwell, D. (2006). The ionic stoichiometry of the GLAST glutamate transporter in salamander retinal glia. *J. Physiol.* doi:10.1113/jphysiol.2006.116830.

Padmashri, R., and Sikdar, S. K. (2007). Glutamate pretreatment affects Ca2+ signaling in processes of astrocyte pairs. *J. Neurochem.* doi:10.1111/j.1471-4159.2006.04166.x.

Palygin, O., Lalo, U., Verkhratsky, A., and Pankratov, Y. (2010). Ionotropic NMDA and P2X<inf>1/5</inf>receptors mediate synaptically induced

Ca^{2+}signalling in cortical astrocytes. *Cell Calcium*. doi:10.1016/j.ceca.2010.09.004.

Panatier, A., Vallée, J., Haber, M., Murai, K. K., Lacaille, J. C., and Robitaille, R. (2011). Astrocytes are endogenous regulators of basal transmission at central synapses. *Cell* 146, 785–798. doi:10.1016/j.cell.2011.07.022.

Parpura, V., Basarsky, T. a., Liu, F., Jeftinija, K., Jeftinija, S., and Haydon, P. G. (1994). Glutamate-mediated astrocyte-neuron signalling. *Nature* 369, 744–747. doi:10.1038/369744a0.

Parpura, V., and Haydon, P. G. (2000). Physiological astrocytic calcium levels stimulate glutamate release to modulate adjacent neurons. *Proc. Natl. Acad. Sci.* doi:10.1073/pnas.97.15.8629.

Pasti, L., Volterra, A., Pozzan, T., and Carmignoto, G. (1997). Intracellular calcium oscillations in astrocytes: a highly plastic, bidirectional form of communication between neurons and astrocytes in situ. *J. Neurosci.* 17, 7817–30. doi:10.1038/nrn1722.

Paulson, O. B., and Newman, E. A. (1987). Does the release of potassium from astrocyte endfeet regulate cerebral blood flow? *Science (80-.).* doi:10.1126/science.3616619.

Pawley, J. B. (2012). “Sources of Noise in Three-Dimensional Microscopical Data Sets,” in *Three-dimensional Confocal Microscopy* doi:10.1016/b978-0-12-668330-1.50007-7.

Pellerin, L., and Magistretti, P. J. (1994). Glutamate uptake into astrocytes stimulates aerobic glycolysis: A mechanism coupling neuronal activity to glucose utilization. *Proc. Natl. Acad. Sci. U. S. A.* doi:10.1073/pnas.91.22.10625.

Pellerin, L., and Magistretti, P. J. (2012). Sweet sixteen for ANLS. *J. Cereb. Blood Flow Metab.* doi:10.1038/jcbfm.2011.149.

Peracchia, C. (1978). Calcium effects on gap junction structure and cell coupling. *Nature*. doi:10.1038/271669a0.

Peracchia, C. (2004). Chemical gating of gap junction channels: Roles of calcium, pH and calmodulin. *Biochim. Biophys. Acta - Biomembr.* doi:10.1016/j.bbamem.2003.10.020.

Perea, G., Navarrete, M., and Araque, A. (2009). Tripartite synapses: astrocytes process and control synaptic information. *Trends Neurosci.* doi:10.1016/j.tins.2009.05.001.

Perez, M. F., Ford, K. A., Goussakov, I., Stutzmann, G. E., and Hu, X. T. (2011). Repeated cocaine exposure decreases dopamine D2-like receptor modulation of Ca2+ homeostasis in rat nucleus accumbens neurons. *Synapse*. doi:10.1002/syn.20831.

Pessia, M., Tucker, S. J., Lee, K., Bond, C. T., and Adelman, J. P. (1996). Subunit positional effects revealed by novel heteromeric inwardly rectifying K+ channels. *EMBO J.* doi:10.1002/j.1460-2075.1996.tb00661.x.

Pizzo, P., Burgo, A., Pozzan, T., and Fasolato, C. (2001). Role of capacitative calcium entry on glutamate-induced calcium influx in type-I rat cortical astrocytes. *J. Neurochem.* doi:10.1046/j.1471-4159.2001.00539.x.

Porter, J. T., and McCarthy, K. D. (1996). Hippocampal astrocytes in situ respond to glutamate released from synaptic terminals. *J. Neurosci.* 16, 5073–5081.

Pow, D. V., and Barnett, N. L. (2000). Developmental expression of excitatory amino acid transporter 5: A photoreceptor and bipolar cell glutamate transporter in rat retina. *Neurosci. Lett.* doi:10.1016/S0304-3940(99)00988-X.

Rama, S., Jensen, T. P., and Rusakov, D. A. (2019). Glutamate Imaging Reveals Multiple Sites of Stochastic Release in the CA3 Giant Mossy Fiber Boutons. *Front. Cell. Neurosci.* 13, 1–6. doi:10.3389/fncel.2019.00243.

Ransom, B. R., and Goldring, S. (1973). Slow hyperpolarization in cells presumed to be glia in cerebral cortex of cat. *J. Neurophysiol.* 36, 879–892. doi:10.1152/jn.1973.36.5.879.

Ransom, B. R., and Sontheimer, H. (1992). The neurophysiology of glial cells. *J. Clin. Neurophysiol.*

Ransom, C. B., Ransom, B. R., and Sontheimer, H. (2000). Activity-

dependent extracellular K+ accumulation in rat optic nerve: The role of glial and axonal Na+ pumps. *J. Physiol.* doi:10.1111/j.1469-7793.2000.00427.x.

Rauen, T., Tanui, R., and Grewer, C. (2014). Structural and functional dynamics of Excitatory Amino Acid Transporters (EAAT). *AIMS Mol. Sci.* doi:10.3934/molsci.2014.3.99.

Reichenbach, A., Derouiche, A., and Kirchhoff, F. (2010). Morphology and dynamics of perisynaptic glia. *Brain Res. Rev.* 63, 11–25. doi:10.1016/j.brainresrev.2010.02.003.

Requardt, R. P., Hirrlinger, P. G., Wilhelm, F., Winkler, U., Besser, S., and Hirrlinger, J. (2012). Ca2+signals of astrocytes are modulated by the NAD+/NADH redox state. *J. Neurochem.* doi:10.1111/j.1471-4159.2012.07645.x.

Reuss, B., and Unsicker, K. (2001). Atypical neuroleptic drugs downregulate dopamine sensitivity in rat cortical and striatal astrocytes. *Mol. Cell. Neurosci.* doi:10.1006/mcne.2001.1017.

Rimmele, T. S., Rocher, A. B., Wellbourne-Wood, J., and Chatton, J. Y. (2017). Control of Glutamate Transport by Extracellular Potassium: Basis for a Negative Feedback on Synaptic Transmission. *Cereb. Cortex*. doi:10.1093/cercor/bhx078.

Roche, K. W., O'Brien, R. J., Mammen, A. L., Bernhardt, J., and Huganir, R. L. (1996). Characterization of multiple phosphorylation sites on the AMPA receptor GluR1 subunit. *Neuron*. doi:10.1016/S0896-6273(00)80144-0.

Rollenhagen, A., Satzler, K., Rodriguez, E. P., Jonas, P., Frotscher, M., and Lubke, J. H. R. (2007). Structural Determinants of Transmission at Large Hippocampal Mossy Fiber Synapses. *J. Neurosci.* doi:10.1523/jneurosci.1946-07.2007.

Rosenegger, D. G., Tran, C. H. T., Wamsteeker Cusulin, J. I., and Gordon, G. R. (2015). Tonic Local Brain Blood Flow Control by Astrocytes Independent of Phasic Neurovascular Coupling. *J. Neurosci.* doi:10.1523/jneurosci.1780-15.2015.

Rothstein, J. D., Van Kammen, M., Levey, A. I., Martin, L. J., and Kuncl, R. W. (1995). Selective loss of glial glutamate transporter GLT-1 in amyotrophic lateral sclerosis. *Ann. Neurol.* doi:10.1002/ana.410380114.

Rusakov, D. A., and Kullmann, D. M. (1998). Extrasynaptic glutamate diffusion in the hippocampus: ultrastructural constraints, uptake, and receptor activation. *J. Neurosci.* doi:10.1523/JNEUROSCI.18-09-03158.1998.

Santello, M., Calì, C., and Bezzi, P. (2012). Gliotransmission and the tripartite synapse. *Adv. Exp. Med. Biol.* doi:10.1007/978-3-7091-0932-8_14.

Sasaki, T. (2013). The axon as a unique computational unit in neurons. *Neurosci. Res.* 75, 83–88. doi:10.1016/j.neures.2012.12.004.

Sasaki, T., Matsuki, N., and Ikegaya, Y. (2011). Action-potential modulation during axonal conduction. *Science (80-.).* 331, 599–601. doi:10.1126/science.1197598.

Savtchenko, L. P., Bard, L., Jensen, T. P., Reynolds, J. P., Kraev, I., Medvedev, N., et al. (2018). Disentangling astroglial physiology with a realistic cell model in silico. *Nat. Commun.* doi:10.1038/s41467-018-05896-w.

Schröder, W., Seifert, G., Hüttmann, K., Hinterkeuser, S., and Steinhäuser, C. (2002). AMPA receptor-mediated modulation of inward rectifier K+ channels in astrocytes of mouse hippocampus. *Mol. Cell. Neurosci.* doi:10.1006/mcne.2001.1080.

Scimemi A, Fine A, Kullmann D, R. D. (2004). NR2B-Containing Receptors Mediate Cross Talk among Hippocampal Synapses. *J. Neurosci.* doi:10.1523/JNEUROSCI.0364-04.2004.

Scimemi, A., Tian, H., and Diamond, J. S. (2009). Neuronal Transporters Regulate Glutamate Clearance, NMDA Receptor Activation, and Synaptic Plasticity in the Hippocampus. *J. Neurosci.* doi:10.1523/jneurosci.4845-09.2009.

Scott, H. A., Gebhardt, F. M., Mitrovic, A. D., Vandenberg, R. J., and Dodd, P. R. (2011). Glutamate transporter variants reduce glutamate uptake in Alzheimer's disease. *Neurobiol. Aging*.

doi:10.1016/j.neurobiolaging.2010.03.008.

Shen, H. -w., Scofield, M. D., Boger, H., Hensley, M., and Kalivas, P. W. (2014). Synaptic Glutamate Spillover Due to Impaired Glutamate Uptake Mediates Heroin Relapse. *J. Neurosci.* doi:10.1523/jneurosci.4564-13.2014.

Shigeri, Y., Shimamoto, K., Yasuda-Kamatani, Y., Seal, R. P., Yumoto, N., Nakajima, T., et al. (2001). Effects of threo-β-hydroxyaspartate derivatives on excitatory amino acid transporters (EAAT4 and EAAT5). *J. Neurochem.* doi:10.1046/j.1471-4159.2001.00588.x.

Shigetomi, E., Bushong, E. a, Haustein, M. D., Tong, X., Jackson-Weaver, O., Kracun, S., et al. (2013a). Imaging calcium microdomains within entire astrocyte territories and endfeet with GCaMPs expressed using adeno-associated viruses. *J. Gen. Physiol.* 141, 633–47. doi:10.1085/jgp.201210949.

Shigetomi, E., Jackson-Weaver, O., Huckstepp, R. T., O'Dell, T. J., and Khakh, B. S. (2013b). TRPA1 channels are regulators of astrocyte basal calcium levels and long-term potentiation via constitutive D-serine release. *J. Neurosci.* 33, 10143–53. doi:10.1523/JNEUROSCI.5779-12.2013.

Shigetomi, E., Patel, S., and Khakh, B. S. (2016). Probing the Complexities of Astrocyte Calcium Signaling. *Trends Cell Biol.* doi:10.1016/j.tcb.2016.01.003.

Shigetomi, E., Tong, X., Kwan, K. Y., Corey, D. P., and Khakh, B. S. (2012). TRPA1 channels regulate astrocyte resting calcium and inhibitory synapse efficacy through GAT-3. *Nat. Neurosci.* 15, 70–80. doi:10.1038/nn.3000.

Shih, P. Y., Savtchenko, L. P., Kamasawa, N., Dembitskaya, Y., McHugh, T. J., Rusakov, D. A., et al. (2013a). Retrograde Synaptic Signaling Mediated by K+ Efflux through Postsynaptic NMDA Receptors. *Cell Rep.* 5, 941–951. doi:10.1016/j.celrep.2013.10.026.

Shih, P. Y., Savtchenko, L. P., Kamasawa, N., Dembitskaya, Y., McHugh, T. J., Rusakov, D. A., et al. (2013b). Retrograde Synaptic Signaling

Mediated by K+ Efflux through Postsynaptic NMDA Receptors. *Cell Rep.* doi:10.1016/j.celrep.2013.10.026.

Shimamoto, K., Lebrun, B., Yasuda-Kamatani, Y., Sakaitani, M., Shigeri, Y., Yumoto, N., et al. (1998). dl- threo -β-Benzyloxyaspartate, A Potent Blocker of Excitatory Amino Acid Transporters. *Mol. Pharmacol.* doi:10.1124/mol.53.2.195.

Shu, Y., Yu, Y., Yang, J., and McCormick, D. A. (2007). Selective control of cortical axonal spikes by a slowly inactivating K+ current. *Proc. Natl. Acad. Sci.* doi:10.1073/pnas.0702041104.

Song, X., Zhao, Y., Narcisse, L., Duffy, H., Kress, Y., Lee, S., et al. (2005). Canonical transient receptor potential channel 4 (TRPC4) co-localizes with the scaffolding protein ZO-1 in human fetal astrocytes in culture. *Glia*. doi:10.1002/glia.20128.

Steinhäuser, C., and Seifert, G. (2002). Glial membrane channels and receptors in epilepsy: Impact for generation and spread of seizure activity. *Eur. J. Pharmacol.* doi:10.1016/S0014-2999(02)01846-0.

Steinhäuser, C., Seifert, G., and Bedner, P. (2012). Astrocyte dysfunction in temporal lobe epilepsy: K + channels and gap junction coupling. *Glia*. doi:10.1002/glia.22313.

Surmeier, D. J., Bargas, J., Hemmings, H. C., Nairn, A. C., and Greengard, P. (1995). Modulation of calcium currents by a D1 dopaminergic protein kinase/phosphatase cascade in rat neostriatal neurons. *Neuron*. doi:10.1016/0896-6273(95)90294-5.

Tabata, H. (2015). Diverse subtypes of astrocytes and their development during corticogenesis. *Front. Neurosci.* doi:10.3389/fnins.2015.00114.

Takano, T., Tian, G. F., Peng, W., Lou, N., Libionka, W., Han, X., et al. (2006). Astrocyte-mediated control of cerebral blood flow. *Nat. Neurosci.* doi:10.1038/nn1623.

Takumi, T., Ishii, T., Horio, Y., Morishige, K. I., Takahashi, N., Yamada, M., et al. (1995). A novel ATP-dependent inward rectifier potassium channel expressed predominantly in glial cells. *J. Biol. Chem.* doi:10.1074/jbc.270.27.16339.

Tanaka, K., Watase, K., Manabe, T., Yamada, K., Watanabe, M., Takahashi, K., et al. (1997). Epilepsy and exacerbation of brain injury in mice lacking the glutamate transporter GLT-1. *Science* 276, 1699–1702. doi:10.1126/science.276.5319.1699.

Timmerman, M. P., and Ashley, C. C. (1986). Fura-2 diffusion and its use as an indicator of transient free calcium changes in single striated muscle cells. *FEBS Lett.* doi:10.1016/0014-5793(86)81073-0.

Tolner, B., Poolman, B., Wallace, B., and Konings, W. N. (1992). Revised nucleotide sequence of the gltP gene, which encodes the proton-glutamate-aspartate transport protein of Escherichia coli K-12. *J. Bacteriol.* doi:10.1128/jb.174.7.2391-2393.1992.

Tong, X., Ao, Y., Faas, G. C., Nwaobi, S. E., Xu, J., Haustein, M. D., et al. (2014). Astrocyte Kir4.1 ion channel deficits contribute to neuronal dysfunction in Huntington's disease model mice. *Nat. Neurosci.* doi:10.1038/nn.3691.

Tong, X., Shigetomi, E., Looger, L. L., and Khakh, B. S. (2012). Genetically Encoded Calcium Indicators and Astrocyte Calcium Microdomains. *Neurosci.* 19, 274–291. doi:10.1177/1073858412468794.

Toyomoto, M., Ohta, M., Okumura, K., Yano, H., Matsumoto, K., Inoue, S., et al. (2004). Prostaglandins are powerful inducers of NGF and BDNF production in mouse astrocyte cultures. *FEBS Lett.* doi:10.1016/S0014-5793(04)00246-7.

Tsien, J. Z., Huerta, P. T., and Tonegawa, S. (1996). The essential role of hippocampal CA1 NMDA receptor-dependent synaptic plasticity in spatial memory. *Cell* 87, 1327–1338. doi:10.1016/S0092-8674(00)81827-9.

Tsien, R. (1989). Fluorescent Probes Of Cell Signaling. *Annu. Rev. Neurosci.* doi:10.1146/annurev.neuro.12.1.227.

Tsukada, S., Iino, M., Takayasu, Y., Shimamoto, K., and Ozawa, S. (2005). Effects of a novel glutamate transporter blocker, TFB-TBOA, on activities of hippocampal neurons. *Neuropharmacology* 48, 479–491. doi:10.1016/j.neuropharm.2004.11.006.

Ulbricht, E., Pannicke, T., Hollborn, M., Raap, M., Goczalik, I., Iandiev, I., et al. (2008). Proliferative gliosis causes mislocation and inactivation of inwardly rectifying K+ (Kir) channels in rabbit retinal glial cells. *Exp. Eye Res.* doi:10.1016/j.exer.2007.11.002.

Unichenko, P., Myakhar, O., and Kirischuk, S. (2012). Intracellular Na + concentration influences short-term plasticity of glutamate transporter-mediated currents in neocortical astrocytes. *Glia*. doi:10.1002/glia.22294.

Vaarmann, A., Gandhi, S., and Abramov, A. Y. (2010). Dopamine induces Ca2+ signaling in astrocytes through reactive oxygen species generated by monoamine oxidase. *J. Biol. Chem.* doi:10.1074/jbc.M110.111450.

Vandenberg, R. J., Mitrovic, A. D., and Johnston, G. A. (1998). Molecular basis for differential inhibition of glutamate transporter subtypes by zinc ions. *Mol. Pharmacol.*

Vargas-Caballero, M., and Robinson, H. P. C. (2003). A slow fraction of Mg2+ unblock of NMDA receptors limits their contribution to spike generation in cortical pyramidal neurons. *J. Neurophysiol.* 89, 2778–2783. doi:10.1152/jn.01038.2002.

Vaughan, R. A., and Foster, J. D. (2013). Mechanisms of dopamine transporter regulation in normal and disease states. *Trends Pharmacol. Sci.* 34, 489–496. doi:10.1016/j.tips.2013.07.005.

Venance, L., Stella, N., Glowinski, J., and Giaume, C. (1997). Mechanism involved in initiation and propagation of receptor-induced intercellular calcium signaling in cultured rat astrocytes. *J. Neurosci.* 17, 1981–1992.

Ventura, R., and Harris, K. M. (1999). Three-dimensional relationships between hippocampal synapses and astrocytes. *J. Neurosci.* 19, 6897–906.

Verkhratsky, A., and Burnstock, G. (2014). Biology of purinergic signalling: Its ancient evolutionary roots, its omnipresence and its multiple functional significance. *BioEssays* 36, 697–705. doi:10.1002/bies.201400024.

Verkhratsky, A., Reyes, R. C., and Parpura, V. (2014). TRP channels coordinate ion signalling in astroglia. *Rev. Physiol. Biochem. Pharmacol.*

doi:10.1007/112_2013_15.

Verkhratsky, A., and Steinhäuser, C. (2000). Ion channels in glial cells. *Brain Res. Rev.* doi:10.1016/S0165-0173(99)00093-4.

Verkhratsky, A., Untiet, V., and Rose, C. R. (2019). Ionic signalling in astroglia beyond calcium. *J. Physiol.* doi:10.1113/JP277478.

Wadiche, J. I., Arriza, J. L., Amara, S. G., and Kavanaugh, M. P. (1995). Kinetics of a human glutamate transporter. *Neuron*. doi:10.1016/0896-6273(95)90340-2.

Wadiche, J. I., and Kavanaugh, M. P. (2018). Macroscopic and Microscopic Properties of a Cloned Glutamate Transporter/Chloride Channel. *J. Neurosci.* doi:10.1523/jneurosci.18-19-07650.1998.

Walsh, D. M., Klyubin, I., Fadeeva, J. V., Cullen, W. K., Anwyl, R., Wolfe, M. S., et al. (2002a). Naturally secreted oligomers of amyloid β protein potently inhibit hippocampal long-term potentiation in vivo. *Nature*. doi:10.1038/416535a.

Walsh, D. M., Klyubin, I., Fadeeva, J. V, Cullen, W. K., Anwyl, R., Wolfe, M. S., et al. (2002b). Naturally secreted oligomers of amyloid beta protein potently inhibit hippocampal long-term potentiation in vivo. *Nature* 416, 535–539. doi:10.1038/416535a.

Walz, W., Wuttke, W., and Hertz, L. (1984). Astrocytes in primary cultures: Membrane potential characteristics reveal exclusive potassium conductance and potassium accumulator properties. *Brain Res.* doi:10.1016/0006-8993(84)90772-8.

Wang, D., Govindaiah, G., Liu, R., De Arcangelis, V., Cox, C. L., and Xiang, Y. K. (2010). Binding of amyloid β peptide to β 2 adrenergic receptor induces PKA-dependent AMPA receptor hyperactivity . *FASEB J.* doi:10.1096/fj.10-156661.

Wang, X., Lou, N., Xu, Q., Tian, G. F., Peng, W. G., Han, X., et al. (2006). Astrocytic Ca2+signaling evoked by sensory stimulation in vivo. *Nat. Neurosci.* doi:10.1038/nn1703.

Warr, O., Takahashi, M., and Attwell, D. (1999). Modulation of extracellular glutamate concentration in rat brain slices by cystine-glutamate

exchange. *J. Physiol.* doi:10.1111/j.1469-7793.1999.783ad.x.

Wise, R. A. (2004). Dopamine, learning and motivation. *Nat. Rev. Neurosci.* doi:10.1038/nrn1406.

Witcher, M. R., Kirov, S. A., and Harris, K. M. (2007). Plasticity of perisynaptic astroglia during synaptogenesis in the mature rat hippocampus. *Glia*. doi:10.1002/glia.20415.

Wong, T. P., Howland, J. G., Robillard, J. M., Ge, Y., Yu, W., Titterness, A. K., et al. (2007). Hippocampal long-term depression mediates acute stress-induced spatial memory retrieval impairment. *Proc. Natl. Acad. Sci.* doi:10.1073/pnas.0702308104.

Woo, D. H., Han, K.-S., Shim, J. W., Yoon, B.-E., Kim, E., Bae, J. Y., et al. (2012). TREK-1 and Best1 Channels Mediate Fast and Slow Glutamate Release in Astrocytes upon GPCR Activation. *Cell*. doi:10.1016/j.cell.2012.09.005.

Yaar, M., Zhai, S., Pilch, P. F., Doyle, S. M., Eisenhauer, P. B., Fine, R. E., et al. (1997). Binding of β-amyloid to the p75 neurotrophin receptor induces apoptosis: A possible mechanism for Alzheimer's disease. *J. Clin. Invest.* doi:10.1172/JCI119772.

Yang, J., Yu, H., Zhou, D., Zhu, K., Lou, H., Duan, S., et al. (2015). Na+-Ca2+ exchanger mediates ChR2-induced [Ca2+]i elevation in astrocytes. *Cell Calcium*. doi:10.1016/j.ceca.2015.06.008.

Ye, L., Haroon, M. A., Salinas, A., and Paukert, M. (2017). Comparison of GCaMP3 and GCaMP6f for studying astrocyte Ca2+ dynamics in the awake mouse brain. *PLoS One*. doi:10.1371/journal.pone.0181113.

Yernool, D., Boudker, O., Jin, Y., and Gouaux, E. (2004). Structure of a glutamate transporter homologue from Pyrococcus horikoshii. *Nature*. doi:10.1038/nature03018.

Zanassi, P., Paolillo, M., Montecucco, A., Avvedimento, E. V., and Schinelli, S. (1999). Pharmacological and molecular evidence for dopamine D1 receptor expression by striatal astrocytes in culture. *J. Neurosci. Res.* 58, 544–552. doi:10.1002/(SICI)1097-4547(19991115)58:4<544::AID-JNR7>3.0.CO;2-9.

Zerangue, N., and Kavanaugh, M. P. (1996). Flux coupling in a neuronal glutamate transporter. *Nature*. doi:10.1038/383634a0.

Zhang, Z., Tao, Z., Gameiro, A., Barcelona, S., Braams, S., Rauen, T., et al. (2007). Transport direction determines the kinetics of substrate transport by the glutamate transporter EAAC1. *Proc. Natl. Acad. Sci.* doi:10.1073/pnas.0704570104.

Zheng, K., Bard, L., Reynolds, J. P., King, C., Jensen, T. P., Gourine, A. V., et al. (2015). Time-Resolved Imaging Reveals Heterogeneous Landscapes of Nanomolar Ca2+ in Neurons and Astroglia. *Neuron* 88, 277–288. doi:10.1016/j.neuron.2015.09.043.

Zheng, K., Jensen, T. P., and Rusakov, D. A. (2018). Monitoring intracellular nanomolar calcium using fluorescence lifetime imaging. *Nat. Protoc.* 13, 581–597. doi:10.1038/nprot.2017.154.

Zheng, K., Scimemi, A., and Rusakov, D. A. (2008). Receptor actions of synaptically released glutamate: The role of transporters on the scale from nanometers to microns. *Biophys. J.* doi:10.1529/biophysj.108.129874.

Zlokovic, B. V., Deane, R., Sagare, A. P., Bell, R. D., and Winkler, E. A. (2010). Low-density lipoprotein receptor-related protein-1: A serial clearance homeostatic mechanism controlling Alzheimer's amyloid β-peptide elimination from the brain. *J. Neurochem.* doi:10.1111/j.1471-4159.2010.07002.x.